Design, Analysis and On-sun Testing of Efficient Nanofluid Based Volumetric Absorption Solar Thermal Systems

Thesis

Submitted for the partial fulfillment of the Degree

of

Doctor of Philosophy

By

Nirmal Singh
(Registration No.: 901708003)

THAPAR INSTITUTE
OF ENGINEERING & TECHNOLOGY
(Deemed to be University)

Department of Mechanical Engineering,
Thapar Institute of Engineering & Technology (Deemed to be University),
Patiala

August 2022

Dedicated

to

my

family

Certificate

This is to certify that the thesis titled **"Design, Analysis and On-sun Testing of Efficient Nanofluid Based Volumetric Absorption Solar Thermal Systems"** being submitted by Mr. Nirmal Singh to Department of Mechanical Engineering, Thapar Institute of Engineering & Technology (Deemed to be University), Patiala for the award of degree of Doctor of Philosophy, is a record of bonafide research work carried out by him under my guidance and supervision and has fulfilled the requirements for the submission of this thesis, which to my knowledge has reached the requisite standard.

The results embodied in the thesis have not been submitted in part or full to any other University or Institute for the award of any degree or diploma.

Nirmal Singh
(Nirmal Singh)

16/08/2022

Dr. Vikrant Khullar
Associate Professor
Department of Mechanical Engineering,
Thapar Institute of Engineering &
Technology (Deemed to be University),
Patiala, India

i

Acknowledgments

I would like to thank most sincerely my supervisor, Dr. Vikrant Khullar, Associate Professor, Department of Mechanical Engineering, Thapar Institute of Engineering & Technology (Deemed to be University), for providing me such a valuable research opportunity and for countless guidance, knowledge and motivation during the course of my research. I learned a lot from him over the course of this Ph.D. work. His goal-oriented style of work, passion towards research, work ethics, has been very inspiring for me. His daily practice of following up on recent scientific literature is something that I also tried to adopt and greatly benefitted. I really appreciate his unconditional support and encouragement towards doing high-caliber research. It has been a great honor to work under his guidance.

I am extremely thankful to Prof. Prakash Gopalan, Director, Thapar Institute of Engineering & Technology (Deemed to be University), Prof. R. Siddique, Dean of Research & Sponsored Projects, Thapar Institute of Engineering & Technology (Deemed to be University) and Dr. T. K. Bera, Head, Department of Mechanical Engineering, Thapar Institute of Engineering & Technology (Deemed to be University) for extending the opportunity to undertake this doctoral research.

I would like to profoundly thank my doctoral committee members, Dr. Madhup Mittal and Dr. Rohit Singla, Department of Mechanical Engineering and Dr. Bhupendra Kumar Chudasama, School of Physics and Material Science, Thapar Institute of Engineering & Technology (Deemed to be University) for their immense help and guiding me towards the right direction. My heart-full thanks to the staff members of the Department of Mechanical Engineering, School of Physics and Material Science, Department of Chemistry and Biochemistry, and Department of Biotechnology at Thapar Institute of Engineering & Technology (Deemed to be University) for their valuable time and help in conducting samples measurement in labs.

My special thanks to, ITMMEC (IIT-Delhi), Mechanical Engineering Department (IIT-Ropar), Panjab University, Chandigarh and Surface Engineering Division, CSIR-National Aerospace Laboratories. for their support for samples measurement.

My endless thanks go to my research colleagues, and friends for their valuable contribution, spiritual and moral support at various stages of my work.

My deepest gratitude goes to my beloved parents, my brother and his wife, who have always supported me through highs and lows of life. They have touched my life in many ways.

I gratefully acknowledge the financial support given by Department of Science and Technology – Science and Engineering Research Board (Sanction order nos. CRG/2021/003272 and ECR/2016/000462).

Finally, I wish to thank the ‘ALMIGHTY’ God for his sufficiency.

Nirmal Singh

Abstract

Majority of the installed solar energy conversion platforms either convert the incident solar radiant energy into electricity (solar-photovoltaic) or into thermal energy (solar-thermal). At present, owing to steep decline in the cost of photovoltaic cells; photovoltaic technology has more presence opposed to solar thermal technologies. In relation to meeting heating and cooling energy demand (which accounts for nearly 50% of the total energy demand), solar thermal technologies potentially promise much greater dividends. Paradoxically, the current worldwide deployment of solar-thermal platforms is meager; this may be ascribed to their relatively low thermal efficiencies and high capital investments. Therefore, there is an urgent need to significantly improve the existing solar thermal systems. To this end, nanofluid based volumetrically absorbing systems have emerged as one of the potent candidates that promise high energy conversion efficiencies and lower material requirements. However, these promising novel systems have not been able to outperform the incumbent solar thermal platforms under the sun owing to instability of nanofluids in real-world service conditions - nanoparticles tend to agglomerate and hence settle down. In order to subjugate the stability barrier, and to operate the volumetric receiver in real world applications; we report a low cost and scalable method to synthesize solar selective nanofluids from 'used engine oil'. The as-prepared nanofluids exhibit excellent long-term stability and photo-thermal conversion efficiency. Moreover, these were found to retain their stability and functional characteristics even after extended periods of high temperature (300°C) heating, ultra violet light exposure and thermal cyclic loading. Building upon it, a nanofluid based volumetrically absorbing solar receiver having reflecting inner surfaces has been tested under outdoor conditions. Results show that steady-state thermal efficiency peaks at an optimum nanoparticles volume fraction ($\eta_{th} = 59 \pm 5.5\%$ at $f_v = 1\%$). Furthermore, the as-prepared nanofluid shows excellent stability i.e. it retains its optical characteristics and particle size distribution even after undergoing pumping and thermal cycles and moving in flow loops (circulation through pipes/valves) during on-sun testing. Moreover, the as-prepared nanofluid has negligible impact on the surface and optical properties of solar receiver constituent materials.

Furthermore, the present work investigates efficacy of ZnO based transparent heat mirrors as thermal loss mitigators in 'direct volumetrically absorbing' solar thermal platforms. Comprehensive experimental and theoretical modeling frameworks have been developed to understand and quantify the heat loss mechanisms. Detailed analysis reveals that

performance characteristics are strong functions of the 'side' of the glass that has been coated (i.e. whether 'receiver facing' (RF) or 'sky facing' (SF) sides of the cover has been coated). Results show that the employing ZnO based heat mirror as a cover significantly reduces the thermal losses relative to uncoated glass cover (25.12% and 21.43% reduction for RF and SF side coated heat mirrors respectively). Moreover, fundamental performance limits of ideal heat mirrors have also been determined for both RF and SF side coated cover configurations. Relative to the uncoated glass covers, ideal heat mirror covers (viz., RF and SF side coated) promise 50.03% and 38.23% thermal loss reduction respectively (@ 400˚C receiver surface temperature and 1.5μm cut-off wavelength).

Overall, the present work represents a significant step in improving the existing volumetric absorpion based solar thermal systems; particularly aiming at intermediate temperature applications (viz. industrial and domestical heating/cooling).

Table of Contents

List of Figures

List of Tables

Nomenclature

English symbols

A	area (m^2)
C	concentration ratio
C_p	specific heat ($JKg^{-1}K^{-1}$)
$e_{b,t,\lambda}$	blackbody emissive power
E	photon energy (eV)
E_p	plasmon energy (eV)
E_c	relaxation energy (eV)
f_v	volume fraction (%)
F_{ij}	view factor
G	direct solar irradiation (Wm^{-2})
h_{gc}	convective heat transfer coefficient from glass to cover inner surface ($Wm^{-2}K^{-1}$)
h_{ga}	convective heat transfer coefficient from cover surface to the outside envelope ($Wm^{-2}K^{-1}$)
J	Radiosity (Wm^{-2})
k	thermal conductivity of air ($Wm^{-2}K^{-1}$)
$K_{a\lambda}$	spectral absorption coefficient
K_{bf}	thermal conductivity of basefluid ($Wm^{-2}K^{-1}$)
k_g	thermal conductivity of glass (= 0.8 $Wm^{-2}K^{-1}$)
K_i	incident angle modifier
$K_{h,\lambda}$	absorption index of refraction
K_{nf}	thermal conductivity of nanofluid ($Wm^{-2}K^{-1}$)
$\dot{m}$	mass flow rate (Kgs^{-1})
n_a	index of refraction of air (= 1)
$n_{h,\lambda}$	spectral index of refraction
Nu	Nusselt number

Pr	Prandtl Number
Q_{loss}	thermal loss (W)
Ra	Rayleigh Number
S_{λ}	spectral solar irradiance (Wm^{-2})
T	temperature (°C)
T_{atm}	atmospheric temperature (K)
T_{avg}	average temperature (K)
T_{sky}	sky temperature (K)
T	time (s)
t_g	thickness of glass (2 mm)
T_g	temperature of receiver surface (K)
$T_{cgi/HMi}$	cover glass inner surface temperature (K)
$T_{cgo/HMo}$	cover glass outer surface temperature (K)

Greek Symbols

β	inclination angle (= 16°)
ε_{eff}	effective emittance
ε_g	emittance of glass (=0.88)
$\varepsilon_{cgi/HMi}$	emittance of cover inner surface
$\varepsilon_{cgo/HMo}$	emittance of cover outer surface
ε_{∞}	adjustment parameter of ZnO (= 3.7)
Λ	wavelength (nm)
η	efficiency (%)
σ	stephen-Boltzmann constant (W/m^2K^4)
τ	transmittance
Θ	Incident angle

Ψ	angle of incidence (= 0°)

Subscripts and superscripts

amb.	ambient
avg.	average
Ct	constant
eff.	effective
In	inlet
Out	outlet
Sw	solar weighted

List of abbreviations

AC	analytical centrifugation
AM	air mass
ATR	attenuated total reflection
CNT	carbon nanotubes
DAQ	data acquisition system
DLS	dynamic light scattering
DNI	direct normal incidence
EDS	energy-dispersive X-ray spectroscopy
EM	electron microscopy
FESEM	field emission scanning electron microscopy
FLVASCs	Fresnel lens based volumetric absorption solar collector
FTIR	Fourier transform infrared spectroscopy
GCR	geometric concentration ratio
HM	heat mirror
IR	infrared
IEP	isoelectric point
MWCNT	multi-walled carbon nanotubes
NIR	near infrared

NS	natural sedimentation
PTVASCs	parabolic trough volumetric absorption solar collectors
SA	spectral analysis
SAS	surface absorption based systems
SEM	scanning electron microscopy
SSS	solar selective surfaces
STS	solar thermal systems
TEM	transmission electron microscope
VAS	volumetric absorption based systems
VASC	volumetric absorption solar collectors
XRD	x-ray Diffraction
UV	ultra-violet
VAR	volumetrically absorbing receiver
VIS	visible
ZP	zeta potential

Chapter 1

Introduction

1.1 Motivation

World-wide energy crisis is a reality now, caused by the fast growth in world population and industrial development as well as the rapid expansion of the society. Fossil fuel reserves being limited; renewable energy resources such as solar, wind, and geothermal could prove to be good alternatives to the conventional fossil fuels.

Although intermittent, but amongst all the renewable energy resources, solar energy is one of the most lucrative options (being huge and freely available resource). Either solar energy could be directly converted to electricity (solar photovoltaic) or it could be converted to thermal energy which could then be employed in a host of applications ranging from cooking, water heating, air conditioning and electricity generation (common Solar thermal systems (STSs) are shown in Fig. 1.1). Currently, STSs are used for numerous domestic as well as industrial purposes (electrical energy generation, water heating system, space heating and cooling systems and desalination). Moreover, solar thermal energy harvesting technique is a more sensible and effective way of harnessing solar energy, when our objective is to heat or to cool something. Solar thermal systems being scalable and being amenable for a variety of applications are expected to provide a solution to the energy demand with minimal damage to the environment. Present solar thermal technology is relatively inefficient compared to its fossil fuel based counterparts, thus making it imperative to improve the existing STSs.

1.2 Background

At the heart of most of STSs (which are used for heating/cooling applications or electricity generation purposes) there is a surface absorption based receiver which converts incident solar energy into thermal energy. In case of parabolic trough collectors (which is presently the most matured CSP technology), the receiver consists of a coated metal tube enveloped in a concentric glass tube. These are generally metal tubes made of materials such as aluminium/carbon/cooper/stainless steel and having a matte black layer or solar selective layer deposited on the surface. This allows sufficient photo-thermal energy conversion of the

incident solar radiant energy into the thermal energy gain of the absorbing surface (walls of the metal tube).

Linear parabolic trough

Linear Fresnel reflector

Parabolic dish

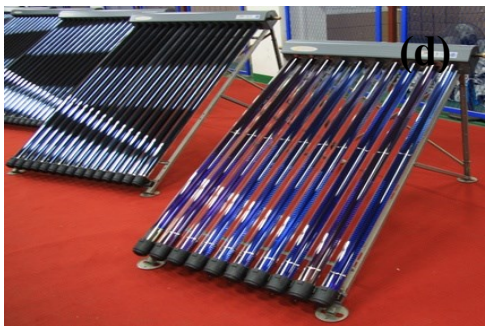

Evacuated tube collector

Solar pond

Solar power tower

Fig. 1.1: Existing solar thermal systems (STS) based on surface-absorption based receivers: (a) Linear parabolic trough[1] (b) linear Fresnel reflector[2], (c) parabolic dish[3], (d) evacuated tube collector[4], (e) solar pond[5], and (f) solar power tower[6].

---

[1]http://www.energynext.in/indias-first-csp-plant-commissioned-under-jnnsm/
[2]https://csp-world.com/news/20131015/001222/first-year-operation-puerto-errado-2-fresnel-csp-plant
[3]https://www.pinterest.com/pin/490399846906567265/
[4]http://www.garagejournal.com/forum/showthread.php?t=78588
[5]https://solarthermalmagazine.com/learn-more/the-solar-pond/70-kwatts-in-elpaso-texas/
[6]https://www.pinterest.com/pin/372884044132238968/

Subsequently, the circulating fluid being in direct contact with the walls of the tubes, the transfer of energy from the tube walls to the fluid happens predominantly firstly by conduction and then by convection. The aforementioned conduction-convection mechanism being relatively less efficient, results in significant temperature gradients across the metal tube wall-fluid interface - termed as "temperature overheat". This inherent "temperature overheat" results in considerable performance reduction in surface absorption based STSs. To circumvent this issue, one of the alternate approaches which has seen recent upsurge is volumetrically thermal energy conversion of the solar radiation within the working fluid instead of at the absorbing surface. The thermal resistance (conductive and convective) is significantly cut down in a volumetric absorption solar thermal system. The graphics of both solar thermal systems, and the corresponding schemes and thermal resistance analogies are compared in Fig. 1.2. The idea of volumetric absorption was presented in the 1970's as a substitute to conventional solar collector with the objective to enhance the photo-thermal conversion efficiency. First of all Minardi et al. [1] developed a volumetric absorption receiver using heterogeneous mixture of micro-sized (μm) carbon particles in shellac (Indian Ink). Although, this work contributed towards the development of new solar thermal systems, but, owing to stability issues of the micro-particle dispersions, could not be a success.

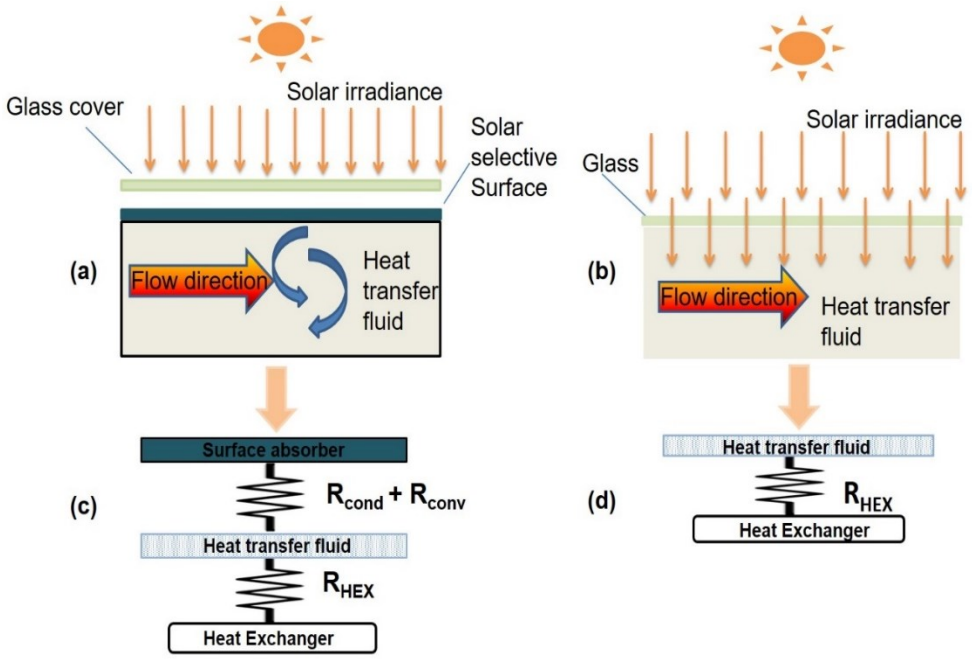

Fig. 1.2: Graphics of the (a) surface based and (b) volumetric absorption solar thermal systems, and their (c-d) Thermal resistance analogy.

Stable colloidal dispersion of nanoparticles (particles with dimension < 100 nm); termed as "nanofluids", have shown to improve optical and thermal properties in relation to the conventional flowing mediums. Nanoparticles when suspended in the basefluid gives variation in properties like density (ρ), specific heat (c_p), thermal conductivity (k), viscosity (μ), and absorption coefficient; which could ultimately enhance heat transfer characteristics of basefluid as shown in Fig. 1.3.

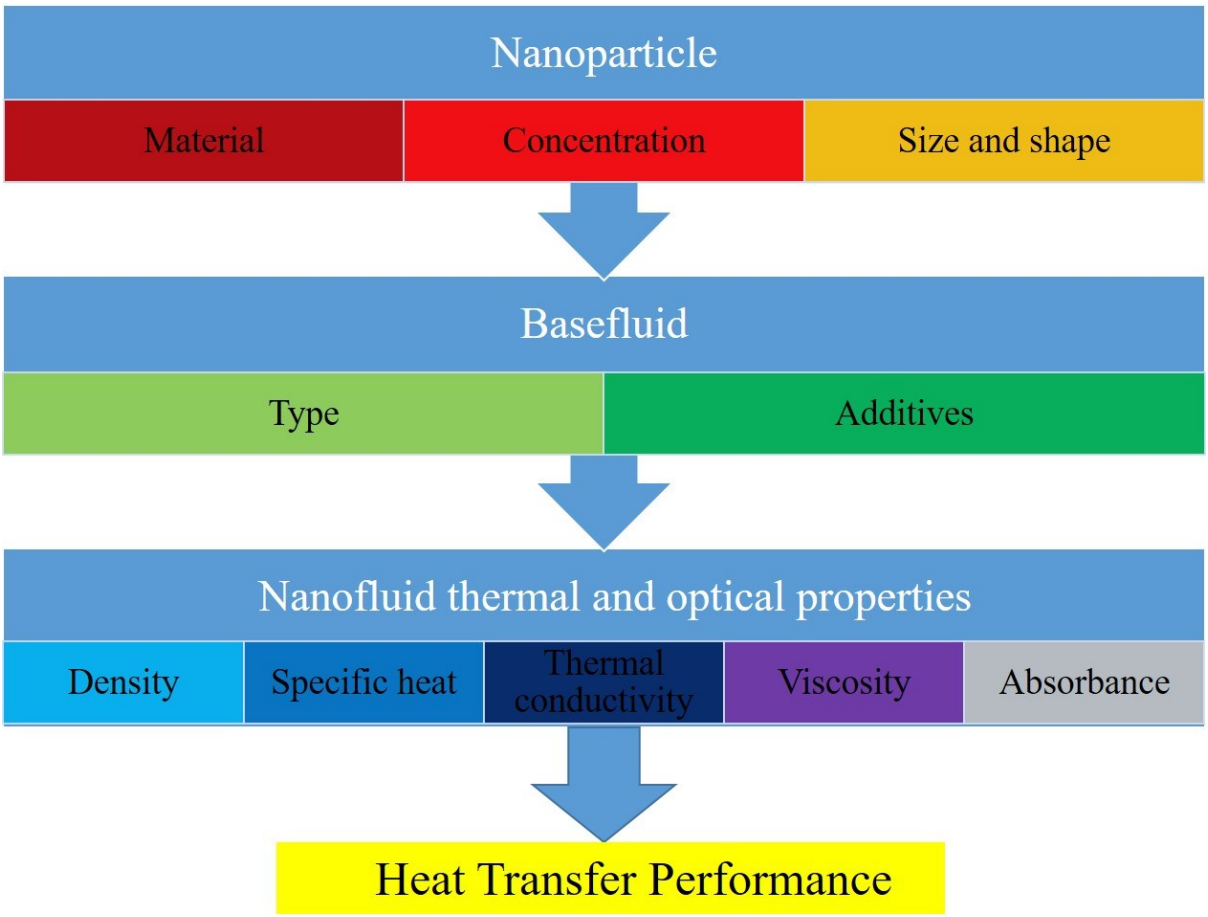

Fig. 1.3: Tailoring nanofluid properties through variation in properties of the basefluid and the nanoparticles.

The advantages of employing nanofluid as the working fluid in solar thermal systems are as follows:

- As the nanoparticles have a particle size in the nano-range (10^{-9}), they could be considered to be as lumped systems and (Biot number < 0.1). A simple calculation suggests that heat transfer coefficient (h) between the nanoparticles and the surrounding media could be as high as 10^8 $Wm^{-2}K^{-1}$.

- The optical properties (such as absorption and extinction coefficients) of nanofluids could be engineered to be considerably higher than the corresponding basefluids.
- The nanofluid thermal conductivity (k_{nf}) has been shown to be high (3% - 5%) in comparison to the corresponding basefluid. [2]
- As nanoparticle dispersion could be engineered for broad temperature range, hence making them suitable for use in a host of variants of volumetric absorption solar collectors. [3]
- Problems such as agglomeration, scaling and clogging of pumps and pipes faced in using micron particles suspension in collector could be eliminated by use of nano sized particles in volumetric absorption based solar thermal system. [4]

In the past decade, extensive work has been carried out in relation to nanofluid based volumetrically absorbing solar thermal systems. However, stability of nanoparticles dispersions under practical operating conditions (nanoparticles agglomerate and stick to the piping/plumbing components [3, 4]) and optimum volumetric receiver design (that achieves high thermal efficiency) are the two fundamental standing issues in the development of these volumetrically absorbing systems.

Present work is essentially a significant step in addressing the aforementioned concerns. An efficient volumetric absorption based solar thermal system employing thermally stable - solar selective nanofluids engineered from 'used engine oil' has been designed and fabricated. Herein, the objective is two-folds: assessing the performance of the designed receiver and testing the as-prepared nanofluid under laboratory as well as real world conditions under the sun.

1.3 Thesis outline

Chapter 1 (Introduction) starts with the motivation behind research in the area of solar thermal technologies. Subsequently, the constructional and working principle differences between conventional and volumetric solar thermal systems have been briefly discussed. At the end, the fundamental challenges in the development of volumetric absorption based solar thermal systems have been listed. In **Chapter 2 (Literature review),** the nanofluid preparation methods and their stability quantification techniques are discussed; also literature relevant to the stability of nanofluids has been discussed. Subsequently, the literature relevant to the experimental studies in the realm of volumetric absorption solar thermal systems has been

critically reviewed. Finally, these have been sub-classified based on the type of concentrating optics employed (parabolic and Fresnel reflectors/refractors) and the typical temperatures involved. **Chapter 3 (Nanofluid synthesis and stability quantification)** details the low-cost and scalable method to synthesize solar selective nanofluid from 'used engine oil'. The as-prepared nanofluids exhibit excellent long-term stability and photo-thermal conversion efficiency. Moreover, these were found to retain their stability and functional characteristics even after extended periods of high temperature (300°C) heating, ultraviolet light exposure, and cyclic thermal loading. Furthermore, the as-prepared nanofluid shows excellent stability, i.e., it retains its optical characteristics and particle size distribution even after undergoing pumping and thermal cycles and moving in flow loops (circulation through pipes/valves) during on-sun testing. In **Chapter 4 (Experimental investigation of volumetric absorption solar collector)** on-sun experimental investigations into nanofluid-based volumetrically absorbing solar receiver (having reflecting inner surfaces) have been carried out. Carbon soot nanoparticles from used engine oil dispersed in paraffin oil forms the working fluid. Results show that steady-state thermal efficiency peaks at an optimum nanoparticles volume fraction (η_{th} = 59 ± 5.5% at f_v = 1%). Moreover, the as-prepared nanofluid has a negligible impact on solar receiver constituent materials' surface and optical properties. **Chapter 5 (Experimental and theoretical estimation of thermal loss from volumetric absorption solar collector)** focuses on experimental setup design and exploring the possibility of heat mirrors reducing the thermal losses in the volumetric receiver. Heat mirrors having infrared reflecting property reduce the radiative loss. Detailed analysis reveals that performance characteristics are strong functions of the 'side' of the glass that has been coated (i.e. whether 'receiver facing' (RF) or 'sky facing' (SF) sides of the cover has been coated). Due to the experimental setup's working temperature limit, the cover configurations have been investigated experimentally only up to 175˚C. However, theoretically, investigation has been done even for high inlet fluid temperatures (up to 400°C). Moreover, fundamental performance limits of ideal heat mirrors have also been determined for both RF and SF side coated cover configurations. **Chapter 6 (Conclusions and recommendations for future work)** summarises the main conclusions of the research work done and delineates the possible future directions which warrant attention.

Chapter 2

Literature Review

Today world is facing many challenges and out of those challenges; generation of clean energy without affecting environment is one of the key challenge. As per the prediction by energy development authorities, by the year 2050, the world population shall require 30 TW (terawatt) of energy in order to maintain economical growth. Sun daily irradiation is adequate enough to bear the energy demand for years [5]. Firstly, the literature relevant to the stability of nanofluids is dealt with. Subsequently, the literature relevant to the experimental studies in the realm of volumetric absorption solar thermal systems has been critically reviewed. Finally, these have been sub-classified on the basis of the type of concentrating optics employed (parabolic and Fresnel reflectors/refractors) and the typical temperatures involved.

2.1 Literature review on stability of nanofluid

2.1.1 Preparation Methods

The stability of nanofluids is one of the most critical issues in adapting a volumetric absorption solar system in industrial applications. The synthesis and operating condition are the factors which affect the nanoparticles stability in dispersion. First of all, nanofluid preparation method must be carefully selected, to ensure the nanofluid stability. The preparation methods are categorised as [6]:

- **One step process**: The nanofluid synthesis is done through in-situ preparation via chemical methods. By this method, agglomerations problem is minimized i.e. highly stable nanofluids could be synthesized, however, this method is difficult to scale up, i.e. nanofluids in bulk quantity with controlled volume fractions is still a challenge.
- **Two-step process**: This route of synthesis of nanofluid involves preparing the mixture of already prepared nanoparticles and the basefluid. Primarily, nanoparticles are synthesized to the favourable size (nm) and shape by processes (physical or chemical) and then, dispersed in the basefluids by mechanical methods (steering and ultra-sonication).

2.2.2 Stability enhancement methods for nanofluids

Nanofluids "very existence" rests on their stability characteristics; agglomeration of nanoparticles can result the nanofluids to lose their enhanced heat transfer properties. Therefore, investigation of stability problem in nanoparticle dispersions (nanofluids) is vital to examine as it could significantly impact the thermo-physical and well as the optical characteristics of nanofluids. Different chemical methods have been used by various researchers to increase the stability of the nanoparticles dispersion. These have been briefly described below:

- **Addition of surfactants:** In order to stabilize the nanofluids, surfactant molecules are also added; i.e. they surround the nanoparticles and form a shell around the nanoparticles. The surface tension of the host liquid is reduced by surfactants and as a result it enhances the dispersion of the nanoparticles. The electromagnetic repulsive forces amongst these enveloped nanoparticles inhibit the probable sedimentation of nanoparticles and hence improve the stability of nanofluid.
- **Chemical functionalization:** In this technique, functional groups (such as COOH, COH and OH) are bonded to nanoparticles' surfaces with the help strong oxidants like sulphuric acid (H_2SO_4) and nitric acid (HNO_3) or by mild oxidation via potassium persulphate ($K_2S_2O_8$) treatments. Recently researchers reported that nanoparticle dispersions employing functionalized nanoparticles are stable up to temperatures on the order of 200°C [7]
- **Plasma functionalization:** Herein, the nanoparticles are functionalized using plasma deposition process. More commonly, the surface modification of CNTs has been done through the aforementioned process. Surface treatment helps in controlling hydrophilicity of the CNTs and therefore, enhancing the CNTs stability in the basefluid. In recent times, researchers have reported stable nanoparticle dispersions (showing remarkable stability for sufficient period of time, nearby 8 months and at high temperatures, 170^{o}C) employing plasma treated multi-walled carbon nanotubes (MWCNTs) [8].
- **Engineering nanofluids pH:** Electro-kinetic properties directly influence the nanoparticle dispersion stability; therefore, a particular value of the pH can enhance the stability characteristics. The nanofluids pH should be controlled such that it should be away from the Isoelectric point (IEP). Next to IEP, fluid zeta potential is zero.

2.2.3 Stability analysis methods for nanofluids

Stability being one of the key attributes dictating the suitability of the nanofluid for a given application; various techniques (as shown in Fig 2.1) have been developed to assess the stability of nanofluids.

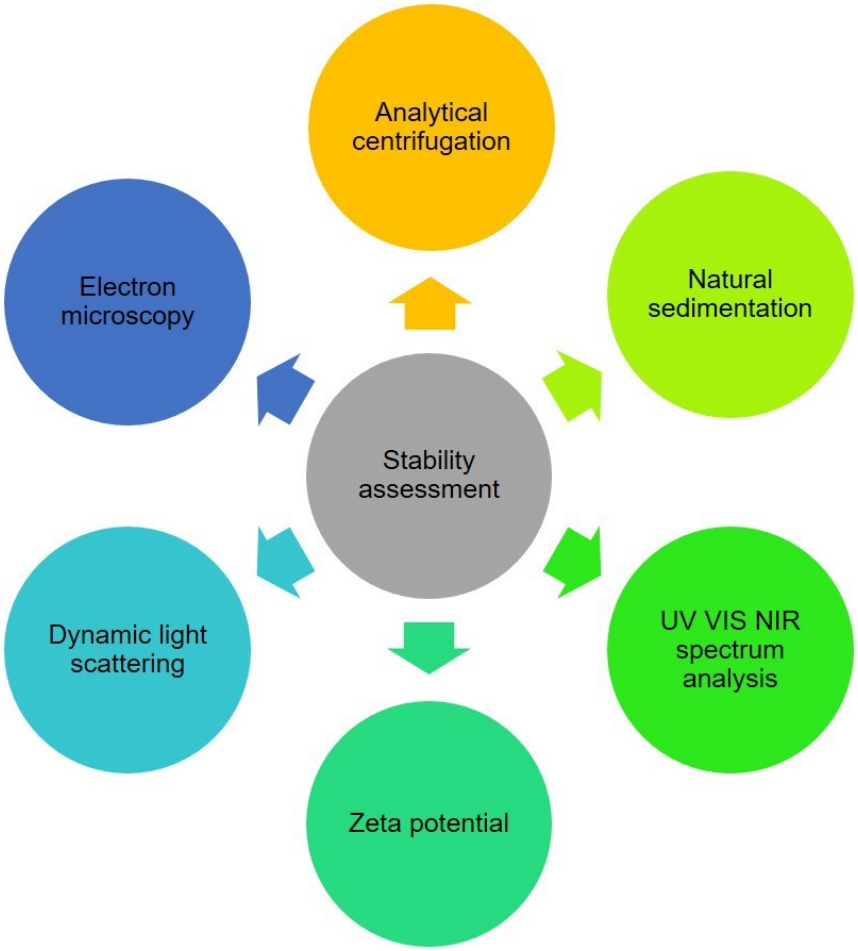

Fig. 2.1: Stability quantification methods

- **Sedimentation method**

  This is one of the most straightforward methods for evaluation of the stability of nanofluids. Sedimentation method can be performed essentially by the following two routes

  1. Natural sedimentation
  2. Analytical centrifugation

  Out of both the aforementioned techniques, natural sedimentation is the primary and the most cost-effective method. The dispersion is checked visually over the time as

nanoparticles tend to sediment out due to density difference. Natural sedimentation is more amenable for checking short term stagnation stability. However, to check the stability in accelerated mode, centrifugation technique is employed. In this method, an exterior field of force is applied so that the nanoparticles start to agglomerate if not stably dispersed in the base-fluids. The volume or weight of sedimentation indicates the stability of nanofluids. [9]. Even though both the methods are simple, but they provide only qualitative information about the dispersion stability.

- **Zeta potential analysis**

  Zeta potential is primarily used to assess the nanoparticles' stability in case of electrostatic and/or electrosteric stabilization. "Zeta potential" is essentially the potential difference between the dispersion medium and the static layer of fluid adhering to the particle. Fundamentally, it specifies the degree of repulsion between adjacent charged particles in dispersion. In general, nanofluids having zeta potential between 40mV - 60 mV exhibit excellent dispersion stability. [10]

- **Spectral analysis method**

  Spectral analysis is another useful way to estimate the stability of nanofluids. Through UV-Vis-NIR spectrophotometer, the change in optical signatures (spectral transmittance curve) could be used as an indicator of stability of the nanofluids [11]. Spectral methods can augment the preliminary revelations from sedimentation methods. In case of the nanofluid having high stability the optical characteristics (spectral transmittance) will nearly remain unchanged even after stagnation and centrifugation process.

- **Electron microscopy methods**

  To measure the typical nanoparticles size and analyse their morphology, microscopy techniques are the most common methods available. Very high resolution microscopes such as transmission electron microscope (TEM) and scanning electron microscope (SEM) are employed to take digital images of nanoparticles, known as electron micrographs. In electron microscopy the sample to be analysed is prepared by drying a small quantity of the prepared nanofluid. The sample preparation is much easy in case of water based nanofluid; for the oil based nanofluid, during the drying process oil gets adsorbed on the surface of nanoparticle - thus necessitating the use of other reagents/chemicals before the sample could be loaded in SEM and TEM instruments.

- **Dynamic Light scattering method**

  Dynamic light scattering (DLS) technique estimates the hydrodynamic diameter of the nanoparticles in the dispersion. This technique is based on the Rayleigh scattering of incident light. Light scattering intensity is disturbed by the Brownian motion of the nanoparticles. Therefore, change in intensity difference would yield particle size as Brownian motion is particle size dependent. Coupling of DLS with sedimentation technique will give more insights about the stability of nanofluid.

Stability being one of the key factors impacting the performance of volumetric absorption solar collectors (VASC); it is imperative that the prepared nanofluids exhibit stability under real life operating conditions. Researchers have employed various methods to anticipate the stability of nanofluids under various conditions that simulate the real life operational conditions. These include techniques such as natural sedimentation, cyclic heating, and constant temperature heating for long hours. Table 2.1 details the selected studies that have tried to address the stability issue. Most of the studies have assessed the nanofluid stability under stagnation conditions. Only a few of these explore the nanofluid stability conditions in cyclic/prolonged heating conditions.

Table 2.1: A brief summary of the studies done by several researchers on the stability of nanofluids. NS- natural sedimentation, AC- analytical centrifugation, ZP- zeta potential, EM- electron microscopy, DLS- dynamic light scattering, SA-spectral analysis

Author(s); Year	**Nanoparticle/ Size**	**Base-fluid**	**Surface modification**	**Temperature**	**Stability assessment method**	**Cyclic heating**	**Stagnation stability period**
Sani et al., 2011 [12]	SWCNHs, Amorphous	EG	----------	Up to 150^{o}C	NS, DLS	5 cycles	6 months
Otanicar et al., 2013 [13]	Silver (35nm), Gold (25nm), Silica	Water, EG	Tween, SDS, Triton X	Up to 80^{o}C	ZP, DLS	200 cycles	2 days
Quinbo et al., 2013 [14]	Cu (25nm,50nm)	Water	SDBS	----------	NS	----------	7 days
Colangelo et al. 2013 [15]	Al_2O_3(45nm), Fe_2O_3(30nm), ZnO(60nm)	Water	----------	----------	NS	----------	1 day
Karami et al., 2014 [16]	CNT	Water	Alkaline functionalization	----------	SA	----------	1 month
Hordy et al., 2014 [17]	MWCNT/30nm	Water, EG, Therminol VP-1, PG	Plasma functionalisation	80% of boiling point of basefluids	NS, SA	3 hours heat	8 months

Khullar et al., 2014 [18]	MWCNT (31.6nm), Amorphous carbon (<50nm)	Ethylene glycol, Water	Triton X-100	32-65°C	ZP, DLS	----------	1 day
Filho et al., 2014 [19]	Silver (10nm)	Water	----------	Up to 50°C	NS	----------	3 months
Zhang et al., 2014 [20]	Cu, Ni, and Ni/C	1-hexyl-3-methylimidazolium Tetra fluoroborate ([HMIM]BF4)	----------	----------	NS	----------	3 days
Sajid et al., 2014 [21]	Al_2O_3	Water	----------	----------	EM, DLS, SA	----------	6 hours
Mehrali et al., 2014 [22]	GNPs(Graphene Nano platelets)	Water	----------	----------	NS, ZP, SA	----------	600 hours
Chen et al., 2015 [23]	Ag, TiO_2, ZnO	Water	----------	Up to 65°C	NS	----------	20 days
Subramaniyam et al., 2015 [24]	TiO_2, C-TiO_2/ 42.77nm	Water, Ethylene glycol	----------	----------	NS	----------	10days
Hordy et al., 2015 [25]	MWCNT	Denatured alcohol	Plasma functionalisation	Up to 65°C	SA	5 cycles of evaporation	20 months
Mesgari et al. 2015 [7]	MWCNT	Therminol 55, EG	Plasma functionalisation	Up to 150°C	SA	1 hour heat	----------
Gorji et al., 2015 [26]	SWCNT/1.5nm	Water	-COOH functional group	25-90°C	DDLS, SA, ZP	50 cycles	3 Months
Jin et al., 2016 [27]	Au (20nm)	Water	----------	Up to 56°C	SA	----------	2 months
Mesgari et al., 2016 [28]	CNT, DWCNT, MWCNT	Therminol 55, EG, Water	Acid treated, KPS treated, Surfactant-SDBS	25-150°C	SA	Heated up to 250°C	
Li et al., 2016 [29]	SiC (30nm)	Diathermic oil	----------	----------	NS	----------	3 days
Menbari et al., 2016 [30]	Al_2O_3 (40nm) - CuO (100nm) binary	Water, EG	Sodium Hexameta Phosphate (SHMP)	----------	EM	----------	1 day
Zhang et al., 2016 [31]	GNPs (30nm), SWCNT (2nm), GE(Graphene)	1-hexyl-3-methylimidazolium Tetra fluoroborate ([HMIM]BF4)	----------	20-100°C	NS	----------	1 month
Shende et al., 2016 [32]	PUMWNT(partially unzipped multi wall carbon nanotube	Water-EG	----------	----------	SA	----------	2 months
Colangelo et al., 2016 [33]	Al_2O_3 (50nm)	Therminol-66	Oleic acid	----------	NS	----------	1 month

Sarsam et al., 2016 [34]	GNPs	Water	GA, CTAB, SDS, SDBS	----------	NS, ZP, SA	----------	2 months
Farzaneh et al., 2016 [35]	TiO_2	Water, EG	----------	----------	NS	----------	21 days
Chen et al., 2016 [36]	Fe_3O_4 (9nm)	Silicone Oil	PDMS (polydimethyl siloxane) ligands	25-150ºC	AC-DDLS, SA	10 cycles	----------
Vakili et al., 2016 [37]	Graphene Nano platelets	Water	----------	----------	NS, ZP	----------	45 days
Li et al., 2016 [38]	CNT	EG	Cyclodextrin modified	----------	NS, ZP	----------	2 months
Zeng et al., 2016 [39]	Sn/SiO_2/Ag (68-105nm)	Therminol Vp-1	----------	50-250ºC	EM	200 cycles	----------
Yan et al., 2017 [40]	SiO_2 (30nm)	Water	----------	41-53ºC	NS, DDLS	----------	20 days
Liu et al., 2017 [41]	Paraffin@MF/graphite	1-hexyl-3-methylimidazolium Tetra fluoroborate ([HMIM]BF4)	----------	30-80ºC	DDLS, SA	50 heating cycles of 30-80ºC/ 4 hours of heating at 70ºC	----------
Akilu et al., 2017 [42]	SiO_2-CuO/C (25nm)	Glycerol-EG mixture 60-40	----------	----------	NS	----------	1 month
Rosa et al., 2017 [43]	Gold (20nm)	Water	----------	1 hour heating at 100ºC	NS	6 cycles	----------
Chen et al.,2017[44]	Graphene oxide	Water	----------	30-80ºC	NS	----------	2 months
Leong et al., [45]	Aluminium oxide (13, <50nm) TiO_2 (21nm)	Water	Gum Arabic (GA), Poly vinyl pyrrolidone (PVP), SDBS	----------	SA	----------	4 weeks
Shende et al.2017 [46]	rGo (Reduced graphene oxide)	Water, EG	Chemical functionalisation	----------	SA	----------	2 months
Furio et al., 2017 [47]	CB (carbon black)	Therminol VP-1	SDS, SDBS, DS (diphenyl sulphone)	----------	SA	10 cycles of heating at 400ºC	5 days
Jian et al., 2017 [48]	MWCNT	Water	Surfactant TNWDIS	20º-80º	NS, DDLS, SA	15 cycles	
Rafael et al., 2017 [49]	Sn (80nm)	EG	----------	----------	SA, DDLS, ZP, EM	----------	10 days
Roberto et al., 2017 [50]	Au (15nm)	Eutectic mixture of biphenyl and diphenyl Oxide.	----------	300ºC	NS	5 hour heat/4 cycles	7 days
Khosrojerdi et al., 2017 [51]	Graphene oxide Nano platelets	Water	----------	----------	NS	----------	340 days

Liu et al., 2017 [52]	Modified graphene	1-hexyl-3-methylimidazolium Tetra fluoroborate ([HMIM]BF4)	----------	Up to 180°C for 1 month	NS, ZP	500 cycles	----------
Chen et al., 2017 [53]	SiC/30nm	1-hexyl-3-methylimidazolium Tetra fluoroborate ([HMIM]BF4)	----------	25-65°C	NS, SA	----------	20 days
Bhalla et al., 2017 [54]	Cobalt oxide	De-ionized water	Surfactant-Triton X-100	Up to 64°C	NS	----------	1day
Chen et al., 2017 [55]	Graphene oxide (GO)	Water		30-75°C	NS, ZP, EM	----------	2 months
Wang et al.,2017 [56]	Al_2O_3 (30nm)	Water	surfactant-Tween 80, Span 80	----------	NS, SA	----------	3 weeks
Wang et al., 2018 [57]	Cu (100nm), CuO (50nm), Chinese ink, C	Water	----------	Up to 80°C	NS, SA	4 hours of heat	1 day
Zeng et al., 2018 [58]	MWCNT (15nm), SiO_2/Ag	Water	Hexadecyl trimethylammonium bromide(CTAB)	30-68°C	NS, ZP	----------	7 days
Yasinskiy et al.,2018 [59]	TiO_2 (20nm)	Eutectic mixture of biphenyl and diphenyl oxide	1-octadecanethiol (ODT)	----------	DDLS, ZP, SA	----------	5 days
Gulzar et al., 2018 [60]	HybridAl_2O_3-TiO_2	Therminol-55	Oleic acid	25-158°C	NS	----------	7 days
Wang et al., 2018 [61]	ZnO-Au 13.3nm	Silicone oil		Up to 100°C	NS, SA	10 cycles	10 days
Khullar et al., 2018 [62]	Amorphous carbon	Water	Triton X-100	Up to 90°C	NS, DDLS	----------	1day
Zhang et al., 2018 [63]	CuO (10nm)	Water	ammonium citrate	Up to 60°C	NS	----------	1 month
Mehrali et al., 2018 [64]	Ag-rGo, rGO (25-45nm)	Water	----------	----------	NS, SA	----------	1000 hours
Coronilla et al., 2018 [65]	Nio (9nm)	Eutectic mixture of biphenyl and diphenyl oxide	Benzalkonium chloride (BAC) and 1-octadecanethiol (ODT)	----------	DDLS, ZP, SA	----------	1 week
Navas et al., 2018 [66]	MoS_2	Eutectic mixture of biphenyl and diphenyl oxide	----------	----------	DDLS, SA	----------	8 days
Wang et al., 2018 [67]	Au-ZNG(N-doped graphene)	Water	----------	Up to 40°C	SA	----------	2 months
Peng et al., 2018 [68]	Fe_3O_4@graphene (10nm)	Silicone Oil	PDMS (polydimethylsiloxane)	6 hour heating @150°C	AC, SA, EM	5 cycles	----------

Taylor et al., 2018 [69]	Ag+ Nasio$_2$ Ag+TEOS(tetraethyl-orthosilicate)	Water	----------	At 80^{o}C	DDLS, EM, ZP, SA,	10 cycles	----------
Aguilar et al., 2018 [70]	TiO_2	Eutectic mixture of biphenyl and diphenyl oxide	----------	----------	DLS, ZP, SA	----------	1 month
Huaxu et al., 2018 [71]	ZnO (231nm)	Water Glycol	----------	10 hours @80^{o}C	NS,AC	----------	4 hours
Qu et al., 2019 [72]	CuO-MWCNT(50nm)	Water	----------	Up to 75^{o}C	NS	----------	1 month
Xu et al., 2019 [73]	rGO	Water-EG mixture	PVP (polyvinylpyrrolidone)	----------	NS	----------	2 months
Sadegi et al., 2019 [74]	Cu_2O(58nm)	Water	PVP-K300 (polyvinylpyrrolidone)	----------	NS	----------	7 months
Shu et al., 2019 [75]	rGO	EG	----------	12 hours @ 120^{o}C	NS	8 cycles	2 weeks
Furio et al., 2019 [76]	CB (carbon black) 10nm	Therminol 66	DS(Diphenyl sulfone)	30 minutes @85^{o}C	DLS	----------	----------
Furio et al., 2019 [77]	SWCNH, Oxidised SWCNH	Water	SDS	30 minutes @75^{o}C	NS,DLS	----------	3 months
Sharaf et al., 2019 [78]	CIT-Au PEG-Au	Water	----------	12 hours @70^{o}C	NS	----------	16 months
Sreekumar et al., 2019 [79]	ATO/Ag (20-50nm)	Water	SDS	----------	NS	----------	30 days
Valizade et al., 2019 [80]	CuO(30nm) SiC(35nm)	Water	GA, CTAB	----------	NS,ZP	----------	1 week
Chen et al., 2019 [81]	MWCNT (20nm)	Water	----------	----------	ZP	50 cycles @60^{o}C	10 days
Li et al., 2019 [82]	SiC(40nm) MWCNT (20nm)	EG	PVP-K30	----------	ZP	30 cycles @60^{o}C	30 days
Alberghini et al., 2019 [83]	Coffee	Glycerol	----------	----------	NS	----------	6 months
Ismail et al., 2019 [84]	CNT(20nm)	Water	GA, PVP, SDS	----------	NS,ZP	----------	6 months
Okonkwo et al., 2019 [85]	Fe TiO_2(30-70nm)	Syltherm-800	----------	----------	ZP	----------	15 days
Hazra et al., 2019 [86]	CB(100nm)	EG	PVP-K30	----------	NS,DLS,ZP	----------	5 months
Lin et al., 2020 [87]	ITO(7.8nm)	Therminol 66	----------	5.5 hours @320^{o}C	NS	----------	72 hours
Qu et al., 2020 [88]	GO (0.2-5um)/ MWCNT (20-30nm)	Therminol 66	Oleic acid	----------	NS	4 cycles	2 weeks
Lee et al., 2020 [89]	Au@SiO_2 (88nm) Ag@SiO_2 (139nm)	Therminol VP-1	----------	1 hour @150^{o}C	NS	----------	6 months
Merino et al., 2020 [90]	WSe_2 (400-900nm)	Eutectic mixture of biphenyl and	Triton X-100	----------	NS, ZP	----------	30 days

		diphenyl oxide					
Li et al., 2020 [91]	CD-CNT	EG	PVP-K30	----------	NS,ZP	30 cycles @60°C	1 month
Sani et al., 2020 [92]	S-GNP(3-12nm) P-GNP(2-18nm)	Water	----------	----------	NS,DLS	----------	1 week
Torres et al. 2020 [93]	CuO (50nm)	PEG	----------	----------	NS,ZP	----------	2 months
Sharaf et al., 2021 [94]	CIT-Au BSA-Au PVA-Au PEG-Au	Water	----------	12 hour @85°C	NS	20 cycles	3 years
Seifiker et al., 2021 [95]	CQD(6.5nm)	PEG-200	----------	----------	NS	6 cycles @60°C	37 days
Zanetti et al., 2021 [96]	SWCNH (30-50nm)	Water	SDS PVP-10	----------	SA	----------	1 week

2.2 Literature review on nanofluid-based volumetric absorption solar collector

Theoretical (numerical and analytical) and experimental studies under no flow conditions clearly point out that it is indeed possible to enhance the overall thermal efficiency through direct volumetric absorption of solar irradiance. However, under flow conditions, it has been found that the nanofluid based solar receivers (whether mounted on a parabolic trough or Fresnel lens based solar collector system), have lower thermal efficiency as compared to its surface absorption counterparts. This may be attributed to stability issues of nanofluids and high radiative losses from VASCs. Therefore, in order to make these novel systems outperform their surface absorption counterparts (under real life flow conditions), more research (both theoretical and experimental) is required.

Table 2.2: A brief summary of low temperature nanofluid-based VASCs.

Authors (s); Year	**Basefluid**	**Nanoparticle**	**Research Findings**
Tyagi et al., 2009 [97]	Water	Aluminium	There is 10% efficiency enhancement with nanofluid as compared to conventional solar collector For low fraction efficiency increases remarkably and remain constant at higher volume fraction.
Mu et al., 2009 [98]	Water	Tio_2, SiO_2, ZrC (40nm)	Temperature enhancement in case of nanofluid dispersion of TiO_2 and ZrC nanoparticle are better than SiO_2 based nanoparticle.
Otanicar et al., 2010 [99]	Water	CNTs, graphite, Ag	An improvement of 6% in steady state efficiency when Silver nanoparticle size is reduced to half (40nm to 20nm)
Lee et al., 2012 [100]	Water	SiO_2/Au core nanoshell	Gold nanoshell based nanofluids at 0.05% volume fraction enhance efficiency up to 70%.
Parvin et al., 2014 [101]	Water	Ag, Cu, Al_2O_3	Cu volume fraction of 3% is most effective in heat transfer rate.

			Increasing the Reynolds number, enhances the collector efficiency 2 times.
Khullar et al., 2014 [18]	Water, EG	Amorphous carbon, MWCNTs	There is an optimum volume fraction of nanoparticle at which volumetric absorption will perform best. Higher stagnation temperature is the result of better optical and conversion efficiency.
Filho et al., 2014 [19]	Water	Ag	Stable suspension of silver nanoparticle is tested under direct sunlight. Stored energy increased to 144% for 6.5 ppm of silver particles.
Cregan et al., 2015 [102]	Water	Al	Nanoparticle concentration strongly influences collector performance. Nanoparticle size and collector angle has no influence on efficiency.
Gorji et al., 2015 [103]	Water	Graphite	Increase in collector length, height and entropy generation results in positive effect on thermal performance, whereas an increase in width decreases the thermal efficiency.
Lee et al., 2015 [104]	Water	MWCNTs	Results show that the efficiency is directly influence by concentration and Peclet number (Pe) and contrariwise influence by Nusselt number (Nu)
Gupta et al., 2015 [105]	Water	Al_2O_3	Enhancement in efficiency for all concentration as compare to the fluid without concentration. Volume fraction beyond 0.005% had a counter effect on efficiency.
Karami et al., 2015 [106]	Water-EG	CuO	Efficiency with nanoparticle concentration is 17% more as compare to the basefluid. Efficiency increases with increase of flow rate.
Delfani et al., 2016 [107]	Water-EG	MWCNTs	Volume fraction of 100ppm had an efficiency of 29% more than basefluid used as the working fluid System design only applicable for low temperature domestic application.
Vakili et al., 2016 [108]	Water	Graphene	A maximum efficiency of 93% is achieved with nanoparticle concentration, while only 69% of basefluid.
Jeon et al., 2016 [109]	Water	AuNRs	Gain in the temperature decreases to an optimum value of Absorption coefficient. Increasing the length of collector has adverse effect on the efficiency
Turkyilmazoglu, 2016 [110]	Water	Al	Efficiency of 100% is also possible with a heat transferring material for the bottom panel.
Gorji et al., 2016 [111]	Water	Graphite, Ag, Fe_3O_4	The thermal efficiency of 40ppm concentration is 57.4% higher than that of basefluid. Exergy analysis is directly related to the incident radiation and inversely with the flow rate.
Menbari et al., 2016 [112]	Water	CuO	Volume fraction and flow rate are effective in enhancing the thermal efficiency. Increase in volume fraction enhance thermal efficiency from 18% to 52%.
Chen et al., 2016[23,113,114]	Water	Ag, Au, TiO_2	Photo thermal conversion efficiency of Silver nanoparticle is better than Gold and TiO_2. Maximum collector efficiency of 90% is attained for a volume fraction of 0.03%
Chen et al., 2017 [115]	Water	Graphene oxide (GO)	Photo-thermal conversion performance of dispersion was more as compare to basefluid and the highest efficiency was 97.45% (@30^o C) and 48.92% (@ 80^o C).

Dugaria et al., 2017 [116]	Water	SWCNH	An optical efficiency is estimated 90.6% for volumetric concentrating collectors. Receiver behaves more like a surface type absorber receiver as the nanoparticle concentration is increased.
Khullar et al., 2018 [117]	Water	Amorphous carbon	Amorphous carbon being well suited for solar thermal applications as compare to others nanoparticles. Due to carbon having highest solar weighted absorptivity at low volume fraction.
Zhang et al., 2018 [63]	Water	CuO	Optimal depth of 1cm for the present nanofluid concentration. An enhancement of 30.4% efficiency is achieved than that of basefluid.
Bhalla et al., 2018 [118]	Water	Al_2O_3, Co_3O_4	Optimum mass fraction have average temperature (19.4°C) rise than ambient temperature compared to others mass fractions.
Mehrali et al ., 2018 [64]	Water	Ag-rGo, rGO	For low volume fraction, receiver efficiency 0f 77% is achievable. A receiver height of 20mm can be used for practical applications.
Zeiny et al., 2018 [119]	Water	Ag, Cu, C	The blending of fluid does not affect solar energy absorption efficiency. Carbon black is most suitable when considering photo thermal conversion efficiency and economic cost.
Beicker et al., 2018 [120]	Water	Ag, MWCNT	Linear relationship amongst stored energy and nanofluid volume fraction. MWCNT shows good dispersion stability as compare to Ag nanoparticles.
He et al., 2018 [121]	Water	Au	Different shapes of Au nanoparticles have been investigated. Thorny Au perform better as compare to quasi-spherical Au nanoparticles.
Campos et al., 2019 [122]	Water	Ag, Au, Cu, GO	Non-spherical Ag and hybrid GO/Ag nanofluid perform better under low and high solar concentration.
Li et al., 2019 [82]	EG	SiC, MWCNT	Hybrid nanofluid absorb 99.9% of solar incident energy at path length of 1cm. Solar thermal conversion efficiency is 48.6% higher as compare to pure EG.
Zanetti et al. 2021 [96]	Water	SWCNH	Circulation, radiative flux and working temperature of nanofluid affect the stability. Functionalised nanoparticles are alternatives to surfactant based nanofluids.

Table 2.3: A brief summary of high temperature nanofluid-based VASCs.

Author (s); Year	Base-Fluid	Nanoparticle	Research Findings
Taylor et al., 2011 [123]	Therminol VP-1	Ag, Al, Cu, graphite	An enhancement of 5-10% is possible for a nanofluid based receiver. Large scale nanofluid based plant can be economical beneficial.
Lenert et al., 2012 [124]	Therminol VP-1	Carbon coated cobalt	Optical thickness for the volumetric receiver is 1.7±0.1. System efficiency of more than 35% is predicted.
Veeraragavan et al., 2012 [125]	Therminol VP-1	Graphite	The bulk fluid temperature is more than that of surface temperature. System efficiency of 35% is presented.
Khullar et al., 2013 [126]	Therminol VP-1	Al	The results predicted that the potential to use solar energy of nanofluid based CPSC is more as compared to conventional receiver. To get the optimum output Size, shape and material of nanoparticle have to be carefully chosen.
Luo et al., 2014 [127]	Texatherm	Al_2O_3, Ag, Cu, CNTs, graphite, TiO_2	Thermal conductivity improves with nanofluid volume fraction and decrease as with rise in the temperature. A maximum 122.7% photo thermal conversion efficiency from graphite based nanofluid as compared to the surface coating collector.
Y.S. Hewakuruppu et al., 2015 [128]	Water-EG-Therminol	MWCNT	Nanofluid wavelengths (short and long) found as a function of temperature and solar concentration. There is a need to search for new material for DACs as an existing collector in not comparable to the surface based collector.
Liu et al., 2015 [129]	Ionic liquid	Graphene	Receiver efficiency directly depends upon the height and solar concentration and inversely proportional to nanofluid concentration.
Wang et al., 2017 [61]	Silicone oil	ZnO-Au	Photo thermal conversion efficiency of the nanofluid is 17% higher than that of basefluid.
Seifiker et al., 2021 [95]	PEG-200	CQD	Surface temperature of nanofluid reaches 145° in 1-hour solar radiation. CQD having good dispersion stability and simple to synthesize without using any dispersant.

2.3 Literature review based on parabolic trough volumetric absorption solar collector

Table 2.4: A brief summary of nanofluid-based PTVASCs.

Author (s); Year	Basefluid	Nanoparticle	Research Findings
Moradi et al., 2015 [130]	Water, Glycol	Carbon-nanohorn	Temperature distribution is maximum inside the fluid domain itself. Water based nanofluid has higher efficiency as compared to glycol having a higher outlet temperature.
Guoying Gu et al., 2015 [131]	Synthetic Oil	CuO	A uniform temperature distribution is obtained in case of nanofluid based collector. Heat transfer in case of nanofluid dispersion based collector is higher than that of surface based collector

Kasaeian et al., 2017 [132]	EG	MWCNT-Nanosilica	Outlet temperature is a function of concentration of the nanoparticle. An increase of 94% in outlet temperature for MWCNT and 45% for nanosilica nanoparticle. The thermal efficiency is 72.8% for MWCNT and 63.6% for silica based nanoparticle.
Menbari et al., 2017 [133]	Water-EG	Al_2O_3-CuO	Ethylene glycol is better for use in a wide range of temperature as compare to water-EG mixture. Binary nanofluid has maximum absorption spectra and thermal conductivity for optimum stable dispersion.
Khullar et al., 2017 [62]	Water	Amorphous Carbon	Out of various nanoparticle for solar application, amorphous carbons nanofluid is best because of its highest solar weight absorptivity at a low volume fraction as that of other nanoparticles. Three times higher temperature increase is achieved as compared to basefluid.
Potenza et al., 2017 [134]	Air	CuO	Mean efficiency of 65% with a maximum temperature of 180^{o}C is achieved. The problem of pipe dirtying is observed in the experiment.
Bortolato et al., 2017 [135]	Water	SWCNH	There is a decrease in thermal efficiency with time. Thermal efficiency reached a maximum of 87% and then decline to 69% after 8 hours of solar exposure. Stability of the nanofluid is the main factor behind decrease in efficiency.
O'Keeffe et al., 2017 [136]	Therminol Vp-1	Al	At low temperature heat mirror coating on nanofluid based receiver is not much efficient. Emissivity of heat mirror is varying at all temperatures.
Sreekumar et al. 2019 [79]	Water	ATO/AG	Results shows a thermal efficiency of 63.5%. Exergy analysis indicates need to reduce heat loss.
Heyhat et al. 2019 [137]	Water	CuO	Arrangement of nanofluid and metal foam improves the efficiency. Thermal efficiency increases from 29% to 46%.
Joseph et al., 2020 [138]	Water	SiO_2/Ag-CuO	At flow rate of 90lph, thermal efficiency enhancement of 48.7%. Exergy efficiency enhancement by 8.4% at 60lph.

2.4 Literature review based on Fresnel lens based volumetric absorption solar collector

Table 2.5: A brief summary of nanofluid-based FLVASCs.

Author (s); Year	Base-fluid	Nanoparticle	Research Findings
Vijayraghavan etal., 2013 [139]	Water	$CuSo_4$	The performance of the collector is not affected by flow rate and optical concentration. High thermal losses in the collector as heat input is reduced.
Kaluri et al., 2015 [140]	Water	$CuSO_4$- Graphite	An increase in solar concentration ratio of 48 to 683 enhances the thermal efficiency from 12.9% to 28.8%. Collector efficiency is influenced by the absorption coefficient of gray fluid whereas the flow rate did not show any effect.
Mesgari et al., 2016 [3]	Water-Therminol 55, PG	CNT	Out of different functionalisation technique used to increase the stability KPS treated nanoparticle show maximum stability. Nanofluid suspension found to be stable up to 250^{o}C.

Muraleedharan et al., 2016 [141]	Therminol 55	Al_2O_3	Absorbance, thermal conductivity and refractive index increase as the volume fraction of nanoparticle increases. A thermal efficiency of 62.7% and maximum temperature of 132ºC is obtained from 0.1% volume fraction of the nanoparticle.
Qiyuan Li et al., 2016 [142]	Therminol55	MWCNT	At 80ºC black chrome coated receiver has a greater collector efficiency of 68% in comparison to nanofluid based solar receiver having 54%. Even after using ITO coated nanofluid based tube has a thermal efficiency, lower than surface based tube.
Kalidoss et al., 2019 [143]	Therminol55	TiO_2	Maximum efficiency of 82.63% is achieved by using secondary refelctors.
Jin et al., 2019 [144]	Water	Au	Pump free volumetric absorption solar collector is presented. Higher amount of solar energy can be captured by using Au nanoparticles which leads to generation of bubbles.
Qu et al., 2020 [88]	Therminol 66	GO/MWCNT	A higher temperature of 153°C is achieved, 56°C higher than basefluid. Receiver efficiency increased from 52% (basefluid) to 70% (nanofluid)
Shen et al., 2020 [145]	Water	ATO/GO	Lighting and heating system has been introduced. At 0.025%/0.0001 volume fraction, light transmission efficiency was 19.5% and photo thermal efficiency was 25.35%. Flow rate has no effect on light transmission.

2.5 Research gaps

- Under real life flow conditions; volumetric absorption based receiver designs have lower thermal efficiency as compared to the surface based receivers. So more research has to be done on the design of volum High temperature and longetric receivers.
- High temperature stability is still a standing issue with nanoparticle dispersions.
- No real time analysis has been done for effect of thermal cycle and pumping action on the stability of nanofluid.
- Most of the theoretical models developed in the literature have not been experimentally validated.

2.6 Objectives of the study

- Design and fabrication of nanofluid-based volumetric absorption concentrating solar collector.
- Experimental Investigation of the performance (in terms of typical temperatures reached and thermal efficiencies achieved) of nanofluid-based volumetric absorption concentrating solar collector.
- Identification of the key operating parameters and quantification of their effect on the

performance of the collector.

- Investigation into the effect of thermal and pumping cycles on the stability, thermo-physical and optical properties of nanofluid.

Chapter 3

Nanofluid synthesis and stability quantification

3.1 Introduction

Building upon the idea of utilizing nanostructures for solar to thermal energy conversion process; volumetrically absorbing solar thermal systems employing nanoparticle dispersions (nanofluids) have been devised by various researchers. Theoretically (and on laboratory scale), particularly at high solar concentration ratios (solar flux), the nanofluid-based volumetrically absorbing solar thermal systems have been shown to have higher thermal efficiencies, lower embodied energies and lower carbon footprints relative to their surface absorption based counterparts [4,18,97,146]. However, these promising novel systems have not been able to outperform the incumbent solar thermal platforms under the sun owing to inefficient receiver designs and instability of nanofluids in real world service conditions - nanoparticles tend to agglomerate and hence settle down; this drastically affects the optical efficiency and hence the overall performance of these systems [135,142]. Presently, a lot of efforts are underway to tailor solar selective, low cost, high temperature, and long term stable nanoparticle dispersions [3,13,69,147–150,25,26,36,47,50–52,61].

3.2 Nanoparticles synthesis

we propose 'used engine oil' (owing to the presence of carbon soot particles) could be employed to synthesize broad wavelength absorption nanoparticle dispersions (volumetrically absorbing solar selective heat transfer fluid).

Annually, approximately 24 million metric tons of 'used engine oil' is discharged into the environment without any recycling or treatment [151]. Therefore, forming one of the most hazardous wastes; having irreversible environmental and health implications. Putting this otherwise hazardous waste to harness solar energy could prove to be a sustainable option.

Pristine (or un-used) engine oil essentially consists of base oil (or blend of base oils) and an additive package to enhance its anti-oxidant, anti-wear, anti-foaming, and dispersancy characteristics. During its operation, the engine oil comes in contact with high temperature cylinder liners and washes away the carbon soot particles (left after combustion) from the cylinder circumference. Furthermore, a host of metallic particles (as a result of wearing action)

enter the engine oil. The blow-by gases also enter the crankcase which may tend to oxidize the engine oil; and here comes the role of anti-oxidant which interrupts the oxidation mechanism by reacting with the reaction intermediates[152–156]. The presence of dispersant molecules helps in dispersing the aforementioned foreign particles in the oil by forming an envelope around these particles. The polar part of the dispersant molecule attaches itself to the surface of the particle; whereas the oleophilic long chain hydrocarbon part helps in mobility of the particle. This ensures that the soot particles do not interact with each other and hence prevents agglomeration of the soot particles; i.e.; agglomeration is prevented through steric stabilization[153]. Now, the effectiveness of dispersant in dispersing the soot particles depends on the effective reactive surface area available on the soot particle where adsorption of the polar part of the dispersant could take place. This is important as many researchers have observed that certain combustion conditions result in un-reactive soot particles; and furthermore, other polar molecules in the engine oil may also get adsorbed on the soot surface and hence reducing the effective reactive surface area available for the dispersants[152,156].

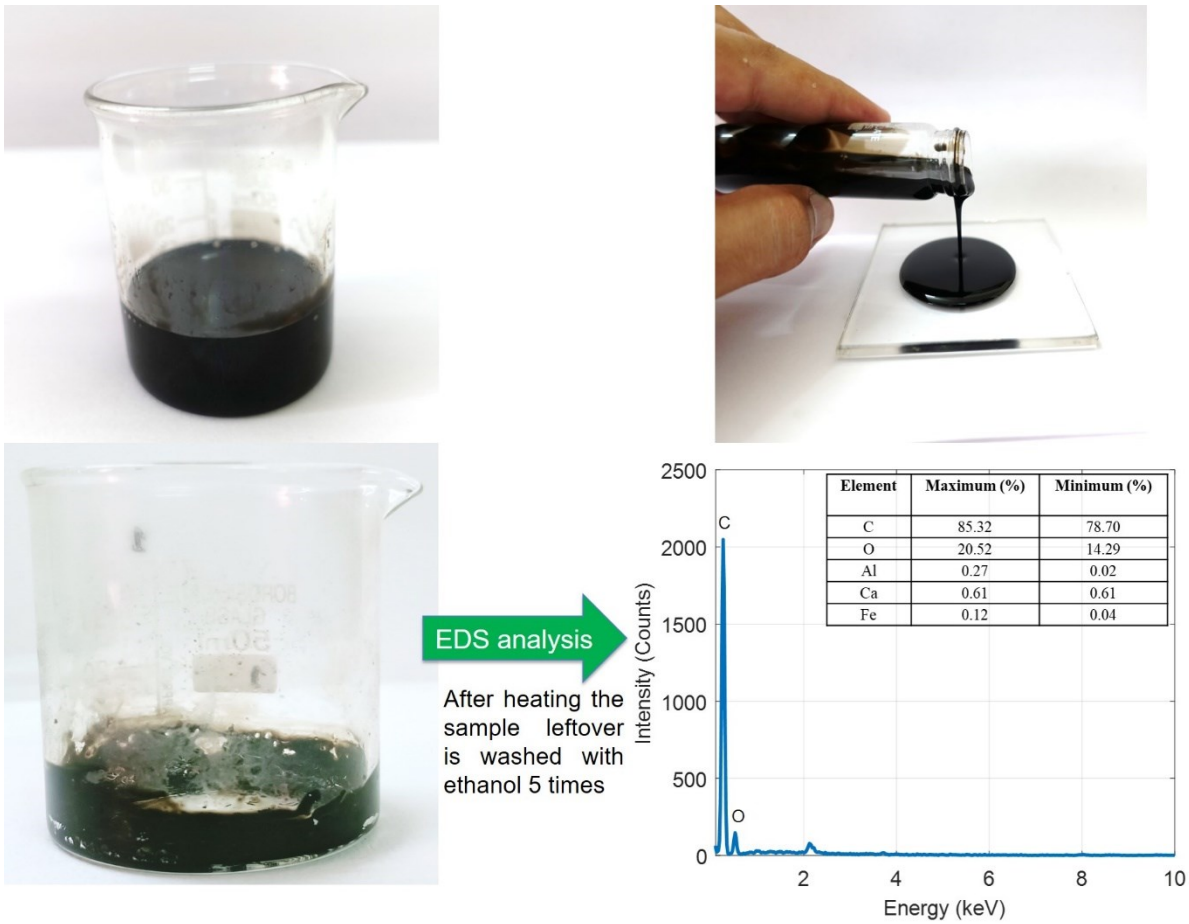

Fig. 3.1 Procured and EDS analysis of the used engine oil.

In the service life of the engine oil, as the concentration of the soot particles increases; more number of soot particles compete for the available dispersant and also thermal degradation (resulting in conformal changes in the oleophilic chain of the dispersant) as well as the oxidation of the dispersant happens - this results in decrease in dispersancy of the soot particles and hence thickening of the engine oil owing to soot particles agglomeration[152,156]. As shown in Fig. 3.1, through Energy-dispersive X-ray spectroscopy (EDS), the percentage of carbon soot particles extracted from the as-prepared nanoparticle dispersion has been found to be on the order of ~85% by weight (other notable elements being O, Al, Ca, and Fe). Used engine oil cannot be directly analyzed by EDS because of the presence of oil which may contaminate the electron beam. So sample was prepared by evaporating 20ml sample at 160°C and the leftover after evaporation was collected. The collected solid particles were then washed with the ethanol (5 times) in order to remove any traces of oil. Finally, the washed particles were loaded onto the copper grid for EDS analysis.

After the end of the engine's service life, oil, in addition to resin, sludge, etc., consists of a large number of nano-sized soot particles that are still enveloped by dispersant molecules.

Filtered oil has been checked for its amount of nanoparticles. Soot particles are extracted by co-flocculation. 1ml and 2ml samples of filtered oil have been mixed with n-butanol (3:1), resulting co-flocculation of the particle at bottom of the beaker. Then the samples are heated in a furnace at 300°C (evaporating light hydrocarbon), and 500°C (evaporating heavy hydrocarbon and dispersants) is present in samples. After heat treatment, the sample weight difference is measured that's comes out to be 0.85% shown in Fig. 3.2.

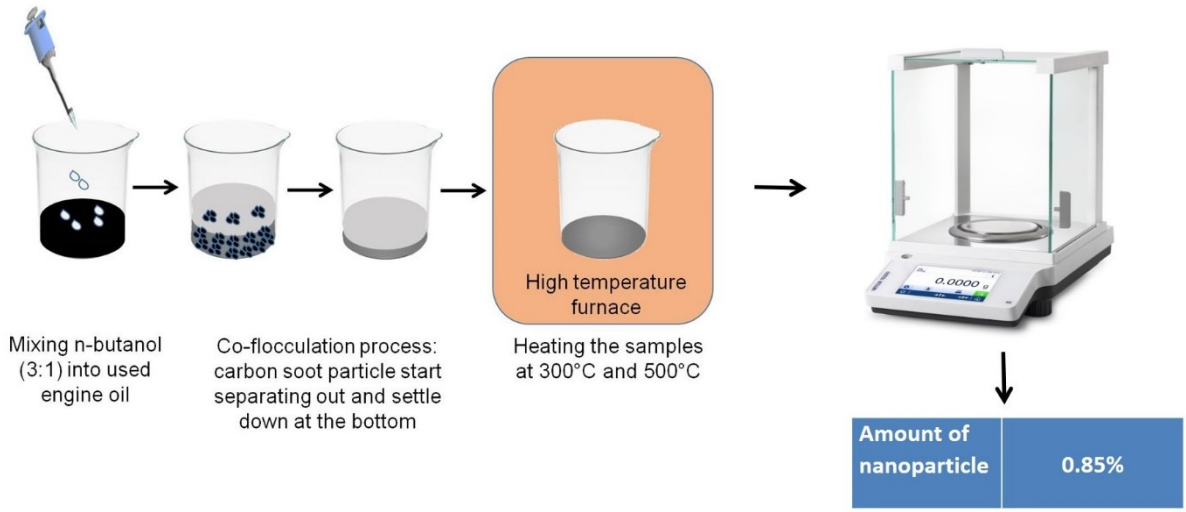

Fig. 3.2 Quantification of amount of nanoparticle in used engine oil.

It is essentially the presence of these carbon soot particles' in the used engine oil that qualifies it to be used as a precursor for synthesizing heat transfer fluid for direct absorption of solar energy. The volume fraction has been determined by the percentage of filtered used oil in pure paraffin light oil per litre.

3.2.1 Understanding soot dispersancy in used engine oil

In order to understand the reasons for dispersancy of soot particles in used engine oil; in addition to 'used engine oil', we also need to analyze two variants of soot particles extracted from the used engine oil -namely - the one in which dispersant macromolecules remain attached to the soot particles (referred to as Type-1) and the other in which there are no attached dispersant macromolecules (referred to as Type-2). Now, in order to extract the two aforementioned soot types from used engine oil, we need to understand solution thermodynamics. The interaction energy between the solvent and polymer macromolecule is given by Eq. (3.1) as [157]

$$\Delta\varepsilon = -K\left(\delta_s - \delta_p\right)^2 \tag{3.1}$$

where K is a positive constant, and δ_s and δ_p are the Hildebrand solubility parameters of solvent and polyolefin (polymer macromolecule) respectively. A value $\Delta\varepsilon$ near zero [in other words, low magnitude of (δ_s - δ_p)] signify good solubility; whereas, values away from zero [high magnitude of (δ_s - δ_p)] signify poor solubility [157–159]. Firstly, in order to extract Type-1 soot particles, we use 1-butanol (3:1), an extraction-flocculent solvent, which through it anti-solvent action on the polymeric macromolecules results in co-flocculation of soot and polymeric soot particles together. This may be attributed to the high value of (δ_s - δ_p), for 1-butanol as the solvent.

Now, in order to extract Type-2 soot particles, we follow the same procedure as followed in extraction of Type-1 soot particles, followed by treatment with a hydrocarbon based solvent (n-heptane in the present work). Here, Type-1 soot particles are mixed in n-heptane followed by centrifugation (for 10 minutes @8000 rpm) - resulting in removal of oil as well as dispersant macromolecules from the carbon soot particles [the value of (δ_s - δ_p) being small with n-heptane as the solvent] [158,159]. Finally, Thermo-gravimetric analysis (TGA) was carried out on all the three samples namely- 'used engine oil', 'Type-1 soot particles', and 'Type-2 soot particles'. Figures 3.3(a) and 3.3(b) show weight loss (%) and differential weight loss (%) as function of temperature. Clearly five distinct regions could be identified in these plots [marked as regions 'A' (30°C - 200 °C), 'B' (200°C - 310 °C), 'C' (310°C - 400 °C), 'D' (400°C - 500 °C), and 'E'

(500°C - 800 °C)]. Region 'A' depicting no appreciable weight loss, region 'B' showing weight loss due to evaporation of light hydrocarbons, region 'C' depicting weight loss due to evaporation of relatively heavy hydrocarbons, region 'D' depicting decomposition/desorption of the attached dispersant molecules and region 'E' represents the pyrolysis of the carbon soot particles. Here, the region 'D' is of particular interest as it represents the quantum of dispersant macromolecular-soot particles interactions - being highest in the Type-1 soot particles - confirming that indeed dispersant macromolecules are adsorbed on the soot particles.

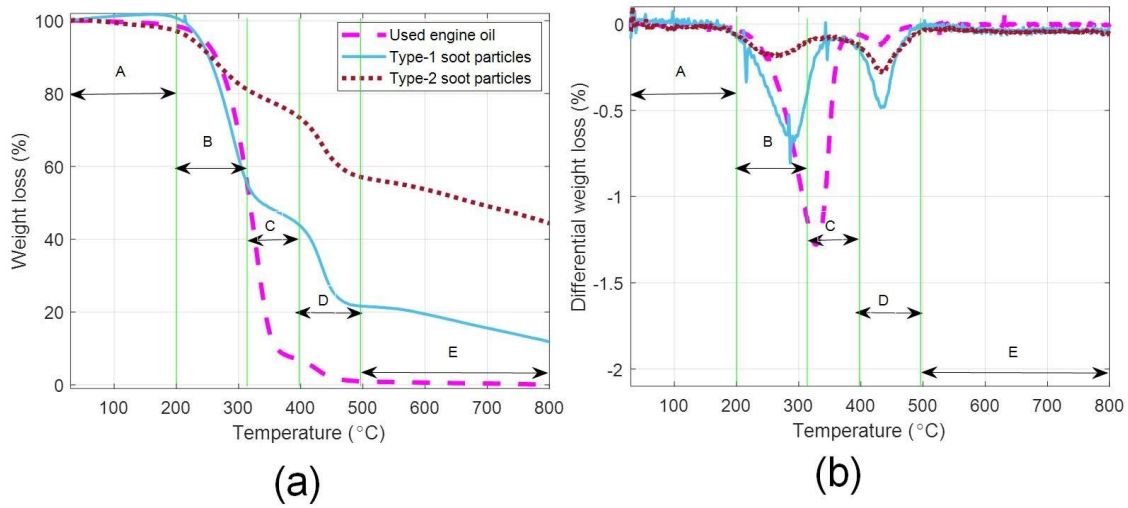

Fig. 3.3 TGA: Weight (%) loss and (b) differential weight loss as a function of temperature for used engine oil, Type-1 soot particles and Type-2 soot particles (Nitrogen atmosphere, 30°C to 800°C at a heating rate of 10°C/min, TGA/DSC 1 - Thermogravimetric Analyzer, Mettler Toledo).

Furthermore, when two soot particle types (Type-1 and Type-2) were separately dissolved into paraffin oil; Type-1 soot particles showed complete miscibility in paraffin oil. Complete reversal of flocculation is a characteristic of sterically stabalized dispersion [160]. Hence, confirming that soot particles are sterically stabalized in engine oil.

However, in case of Type-2 soot particles, partial miscibility was observed - particles separating out of the solution. The partial miscibility could be attributed to incomplete removal of oil/dispersant macromolecules during treatment with n-heptane [this is also apparent from the TGA of Type-2 soot particles; see region D, Fig. 3.3(b)].

3.3 Nanofluid synthesis philosophy and elemental-morphological analysis

Used engine oil has been collected from a 15000 km run 4-stroke diesel engine. To filter out sludge, resin etc. a cotton cloth has been used. Subsequently, the filtered 'used engine oil' was furthered filtered with 0.7μm filter paper. Desired fractions of the resulting filtered 'used engine oil' (after undergoing filtration process) have been mechanically mixed with compatible non polar base oil (paraffin oil light, (840 kgm^{-3})) followed by 30 minutes of ultra-sonication in a bath type ultasonicator (Bath type - 250 W, Sarthak Scientific) - thus forming nanofluids of different concentration.

The mixture was then ultra-sonicated to get the required nanoparticle dispersions (see Fig. 3.4). Figure 3.5(a) shows the picture of as-prepared nanofluids of different concentrations (1.25, 2.5, 5, 10 and 20 ml/L) of 'used engine oil' in pristine paraffin oil. Transmission electron microscopy (TEM) images show that the soot particles are present in the form of nano-clusters of irregular curvilinear geometry [see Fig. 3.5(c)]. The sample for TEM analysis was prepared by solvent extraction method. The used oil was mixed with n-heptane (1:60) and ultra-sonicated for 30 minute. The prepared sample was then placed on the carbon grid and washed with n-heptane to remove any traces of oil on the surface of soot particles. Furthermore, to get the better image quality, sample was washed with diethyl ether (2 times). Hydrodynamic particle size has been measured through DLS (Malvern Zetasizer Nano S (ZEN 1600)); particle size varies in the range of 15 nm to 68 nm, average particle size being 38 nm [see Fig. 3.5(b)].

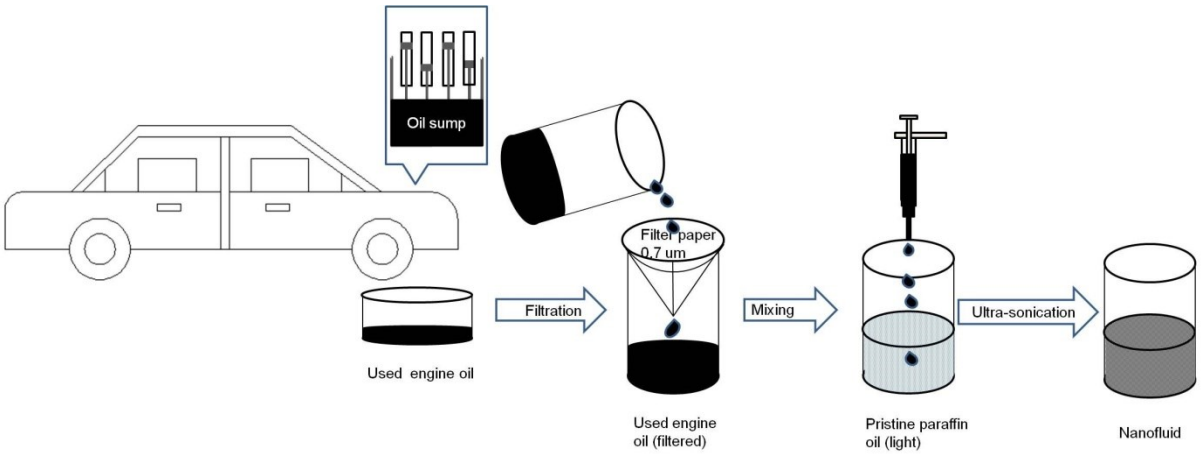

Fig. 3.4 Schematic showing the steps involved in nanoparticle dispersion synthesis.

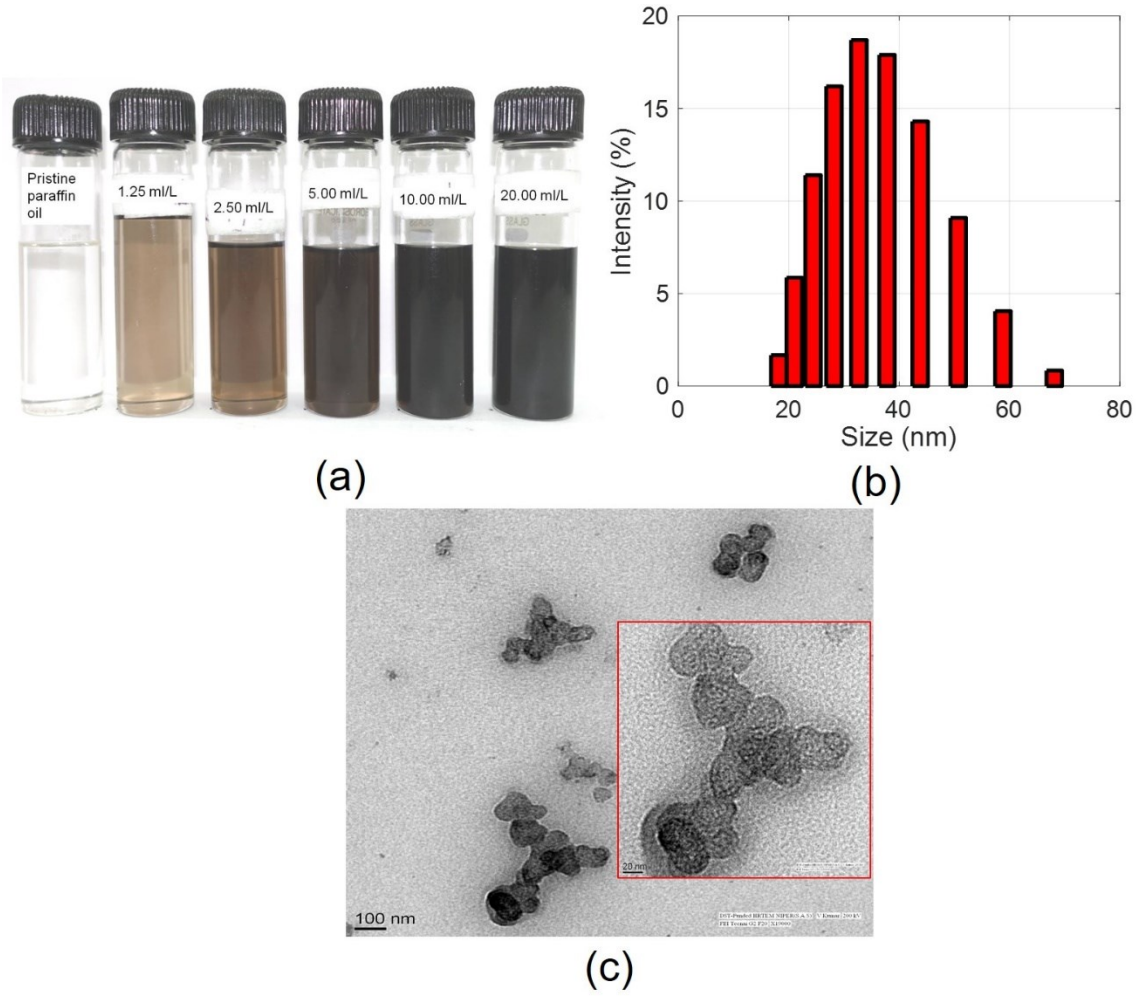

Fig. 3.5 (a) Photographs of the as-prepared nanofluids of different concentrations, and (b) Dynamic light scattering (DLS) measurements of the as-prepared nanofluid sample (5 ml/L), and (c) TEM images of the soot particles in the used engine oil (FEI Tecnai G2 F20, Netherlands).

3.4 Experimental investigation of nanofluid stability

In the past decade, extensive work has been carried out in relation to volumetric absorption solar thermal systems. However, stability of nanoparticles dispersions under practical operating conditions (nanoparticles agglomerate and stick to the piping/plumbing components [135]) fundamental standing issues in the development of these volumetrically absorbing systems. Most of reported work only express optical spectra of nanofluid and the stability of nanofluid by natural sedimentation or stagnation stability for some days or weeks (chapter-2). In order to use the nanofluid in practical application, stability should be extensively checked.

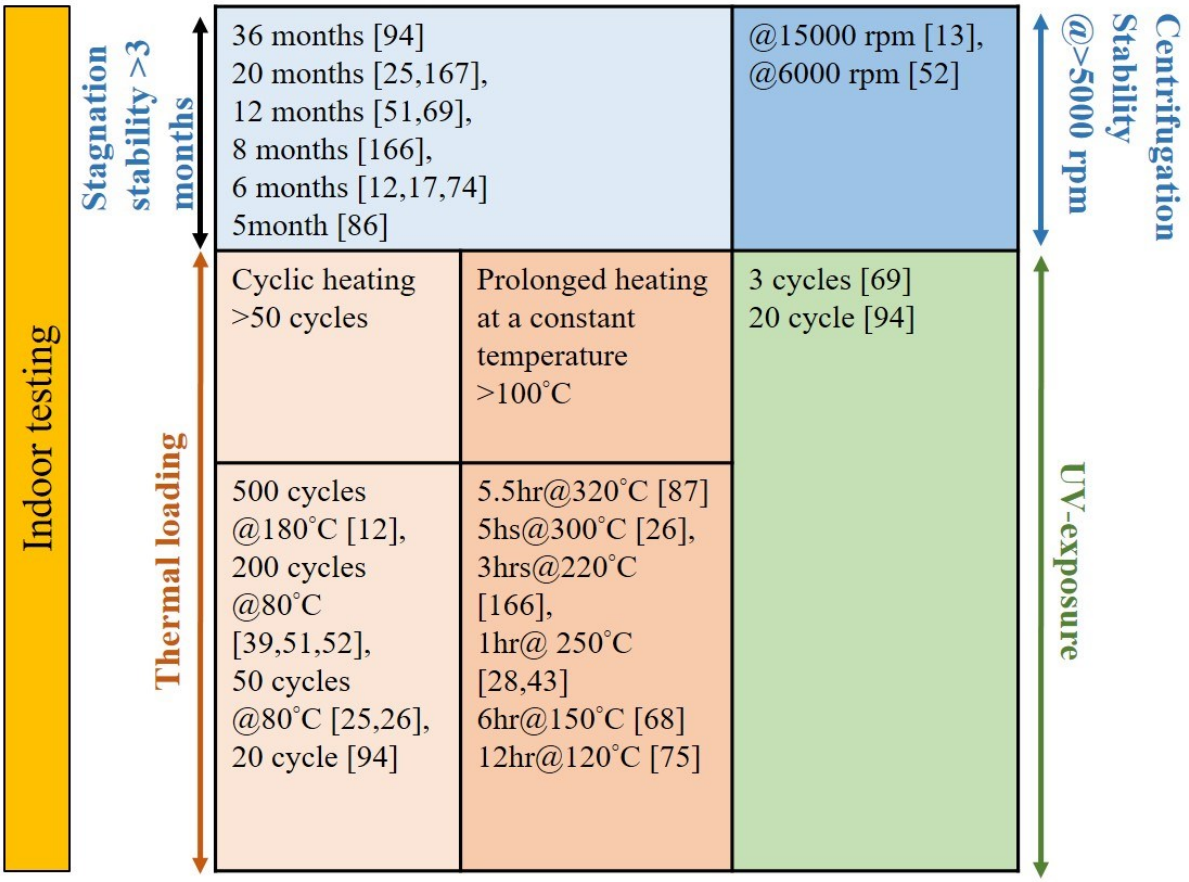

Nanofluid stability tests

Outdoor testing

Concentrated radiation		Non-concentrated radiation	
Flow condition	Non-flow condition	Flow condition	Non-flow condition
Particles start to agglomerate within 3h of sunlight exposure [135] Particles deposit on the walls of the receiver [181]			Particles precipitate after 20 days of sunlight exposure [23]

Fig. 3.6 Nanofluid stability testing (indoor and outdoor) under various operating conditions

In relation to nanofluid stability, there have been recent breakthroughs in synthesizing stable nanofluids through chemical/plasma nanoparticles functionalization techniques [3,161].
Majority of the reported works in the literature are limited to laboratory scale stability testing of nanofluids (chapter-2). Reported work for stability under laboratory scale is scrutinize by four condition, categorized as stagnation (>3 months), centrifugation (>5000 rpm), thermal loading and UV-exposure stability. Figure 3.6 lists the reported works relevant to the nanofluid stability. The as-prepared nanofluid as explain has been examine for stability by all the four method under laboratory as well as outdoor condition.

3.5 Stability of the as-prepared nanofluid

3.5.1 Long-term stability

As 'heat transfer fluids' in volumetric absorption platforms; nanofluids are expected to maintain their optical and thermo-physical properties under extended periods without any appreciable degradation for consistent and efficient photo-thermal conversion. Long-term stability of the as-prepared nanofluid dispersions has been assessed under natural and accelerated sedimentation (centrifugation) conditions.
The as-prepared nanofluid is kept under stagnation condition for 6 months. After that period nanofluid has been tested spectrally for their change in transmittance as well as hydrodynamic particle size. The nanofluid also accessed for stability by accelerated sedimentation i.e., centrifugation. Nanofluid has been centrifuge at 8000 rpm for 90 minutes. During centrifugation, the fluid experiences severe shear stresses- simulating real flow conditions which the heat transfer fluid may be subjected to in actual solar thermal systems [162–167]. After centrifugation sample checked for their change in transmittance and hydrodynamic particle size. Figure 3.7 reveals that the as-prepared nanofluids exhibit remarkable long term stability and can withstand high shear stresses without any appreciable change in their optical characteristics, and nanoparticle hydrodynamic size distribution.

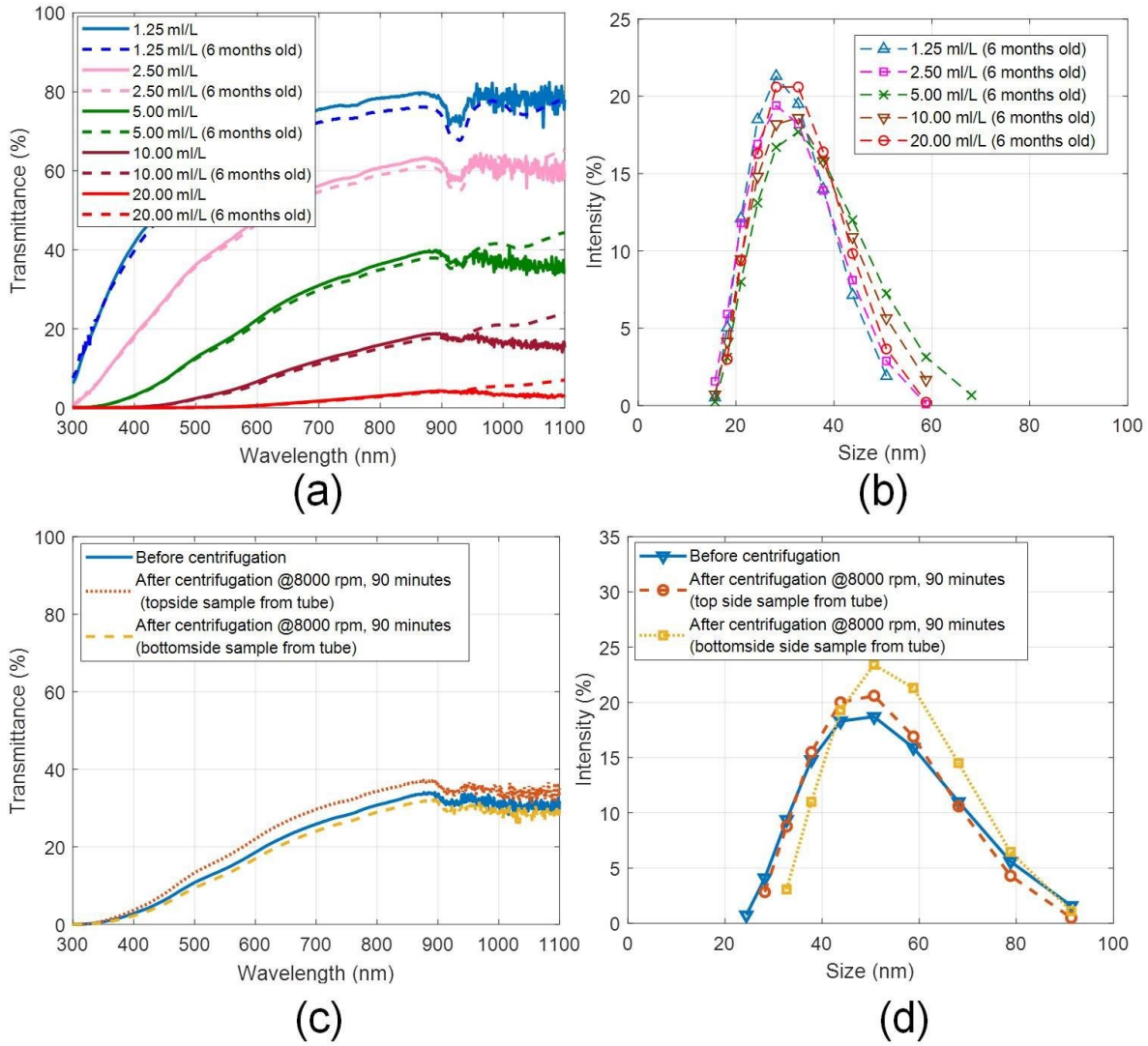

Fig. 3.7 (a) Spectral optical characteristics (Shimazdu UV-2600), and (b) hydrodynamic particle size distribution of the as-prepared and six months old nanofluid samples (Malvern Zetasizer Nano S (ZEN 1600)); and (c) spectral optical characteristics, and (d) hydrodynamic particle size distribution of the as-prepared and after centrifugation (for 90 minutes @8000 rpm) nanofluid samples (5 ml/L).

3.5.2 High temperature stability

The nanofluids should maintain their desired characteristics under constant and cyclic thermal loads. In its service life, the nanofluids are expected to absorb high solar flux (particularly in high solar concentration solar thermal systems), which in turn shall result in rapid and significant temperature rise. Furthermore, the nanofluid shall transfer the absorbed energy to a secondary fluid (such as water) - thus experiencing rapid temperature drops. These rapid heating and cooling cycles form the integral part of any power cycle in general and solar

electricity generation systems (SEGS) in particular. The as-prepared nanofluids were found to possess excellent stability and retain their functional characteristics under constant as well as cyclic thermal loads. During cyclic thermal loading, the nanofluid was rapidly heated to a particular fixed temperature and then was suddenly cooled by dipping it into the water bath maintained at room temperature (see Fig. 3.8).

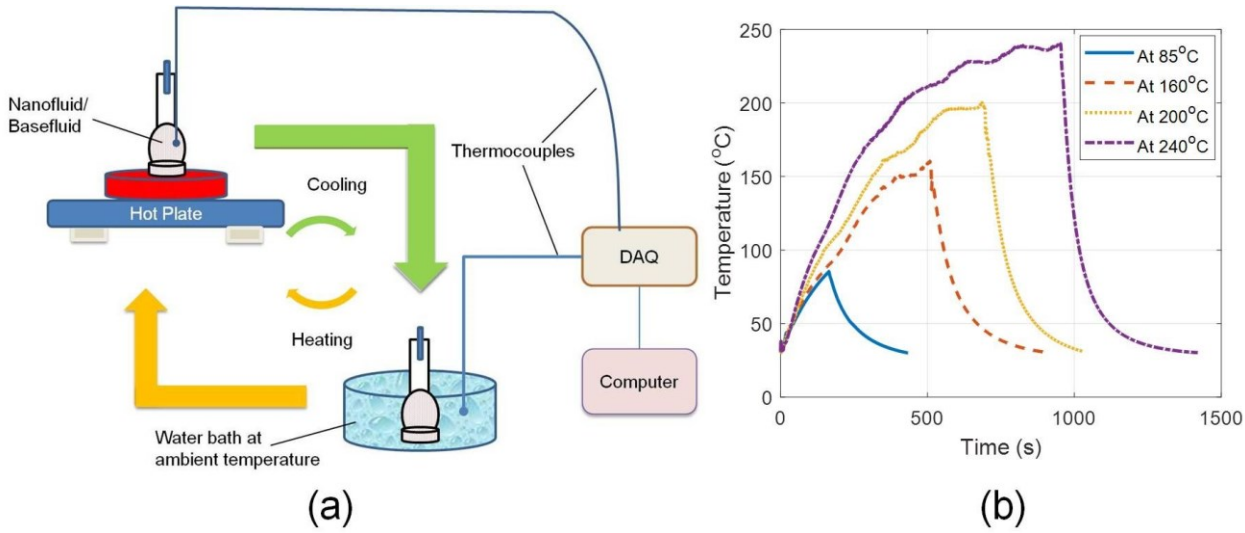

Fig. 3.8 (a) Schematic showing the procedure followed for carrying out thermal cyclic tests, and (b) heating - cooling curves for the thermal cycling at different temperatures.

For the purpose of tracking the temperatures, K-type thermocouple remained dipped in the nanofluid during the entire testing period. This however allowed the ambient air (oxygen) to interact with the nanofluid which in effect resulted in the oxidation of the basefluid (paraffin oil, Fig. 3.9) as well as the oxidation of added used engine oil (See Fig. 3.10) - proving to be detrimental to the stability of the nanofluids particularly at high temperatures.

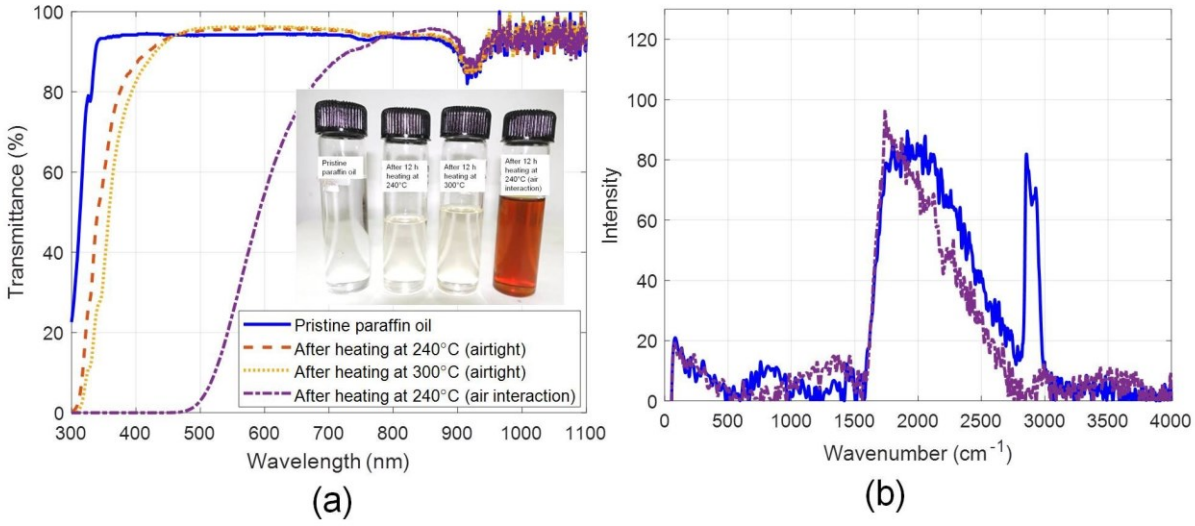

Fig. 3.9 (a) Effect of oxidation on the (a) optical properties, and (b) Raman spectra of pristine paraffin oil (Measured at 532 nm, Horiba Scientific).

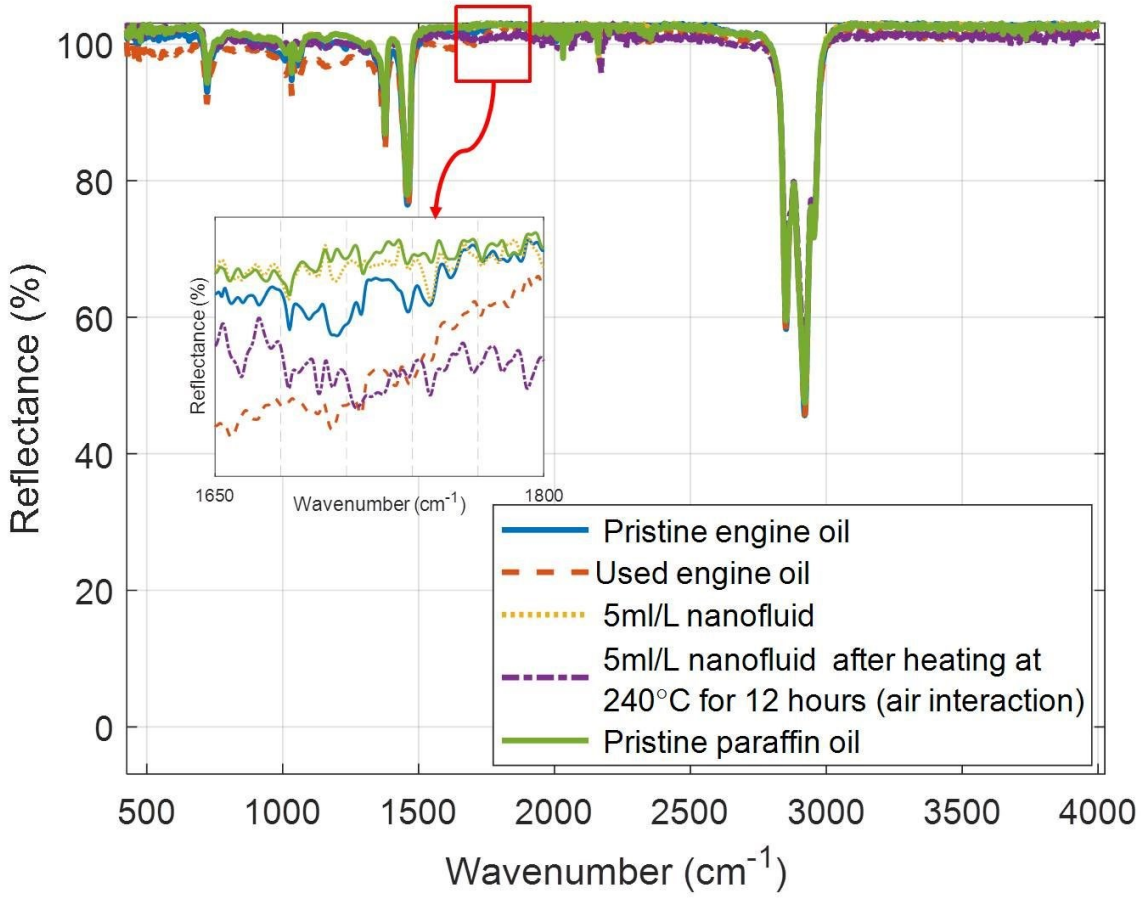

Fig. 3.10 ATR-FTIR spectra showing the effect of oxidation on nanofluid (5ml/L); 1650 cm^{-1} - 1800 cm^{-1} being the region of oxidation products [168]. For better comparison; spectra have also been shown for pristine engine oil, used engine oil and pristine paraffin oil. Fourier

transform infrared (FTIR) spectroscopy (Infrared measurements were made using attenuated total reflectance (ATR) technique with help of Nicolet iS50 FT-IR)

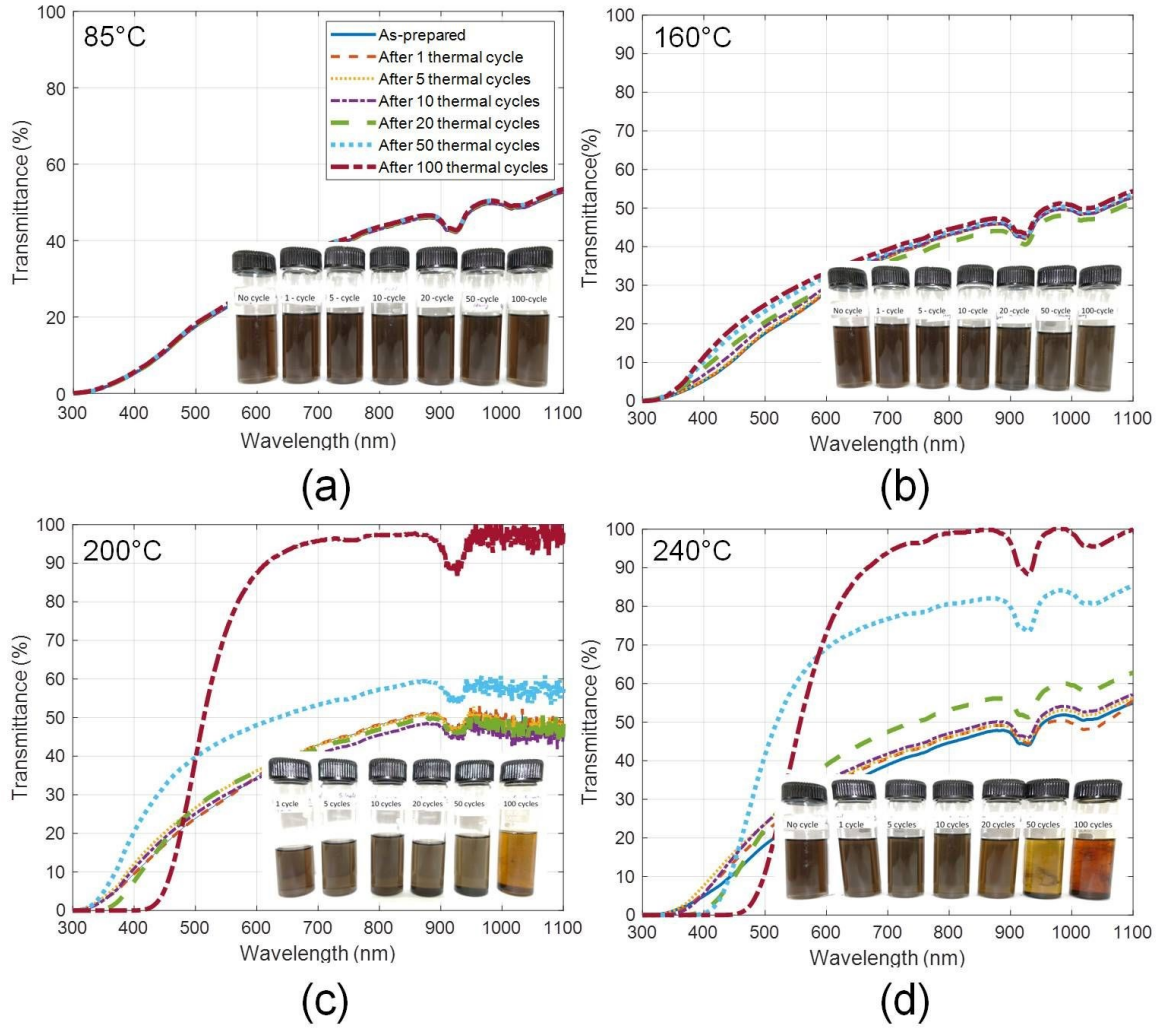

Fig. 3.11 (a) Effect of cyclic thermal loads on the optical properties of the as-prepared nanofluids at (a) 85°C, (b) 160°C, (c) 200°C, and 240°C.

Similar phenomenon was discovered during constant thermal loading (12 hours heating at constant temperature) as well (see Fig. 3.11,3.12, and 3.13) - indicating that it is not the thermal stresses but oxidation of the nanofluid that renders the nanofluid unstable at high temperatures. Interestingly, when nanofluid was prepared using oxidized paraffin oil as the basefluid; it was observed that the added used engine oil was not fully miscible - as clouds of used engine oil could clearly be seen (although particles did not settle out). Thus, oxidation of basefluid hampers the solubility of the used engine oil. As a whole; instability of the nanofluid happens both by oxidation of the basefluid as well as the oxidation of the dispersant macromolecule

attached to the soot particle - the later being responsible for settling out of soot particles from the solution.

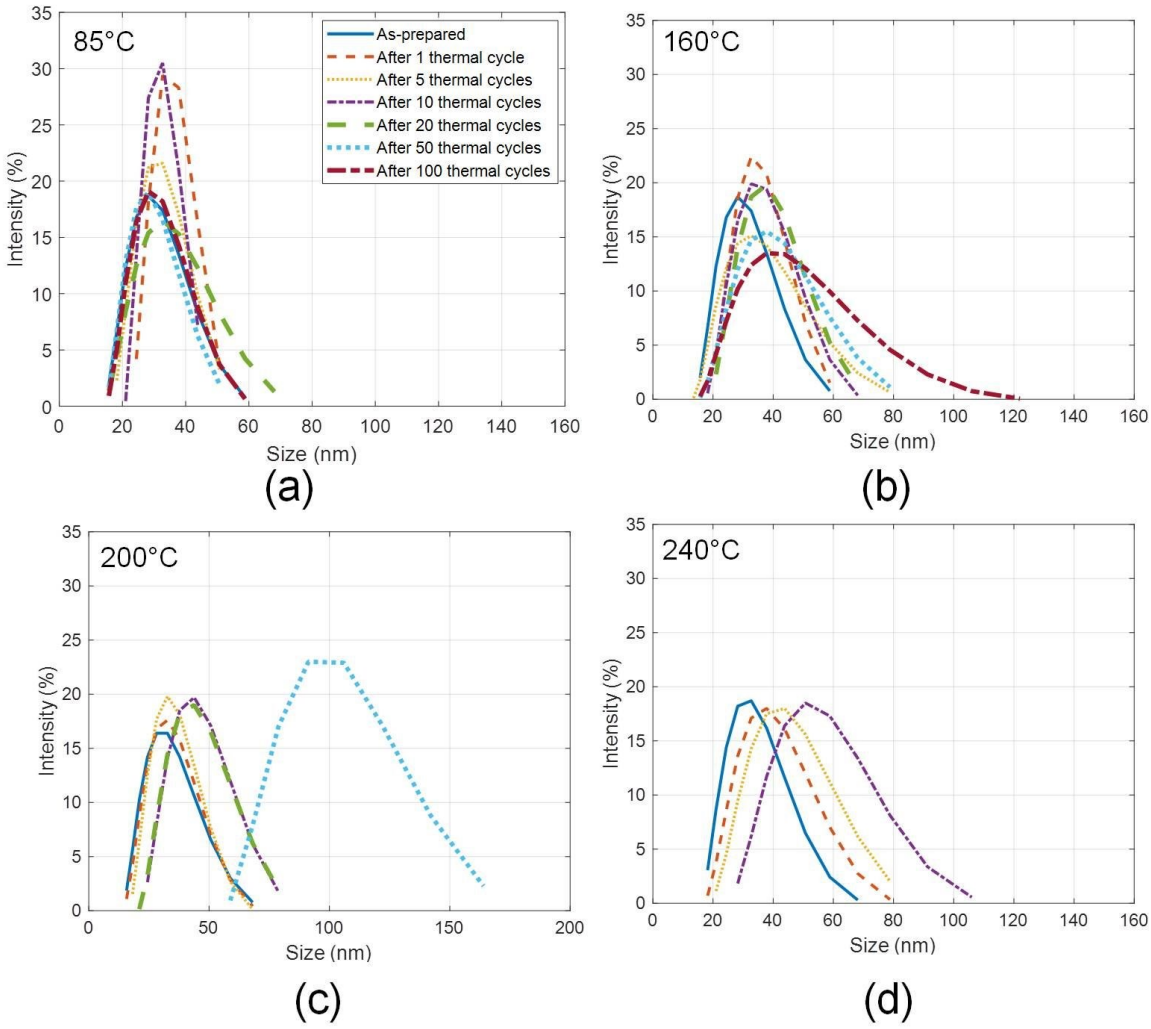

Fig. 3.12 (a) Effect of cyclic thermal loads on the hydrodynamic size distribution of the as-prepared nanofluids at (a) 85°C, (b) 160°C, (c) 200°C, and 240°C.

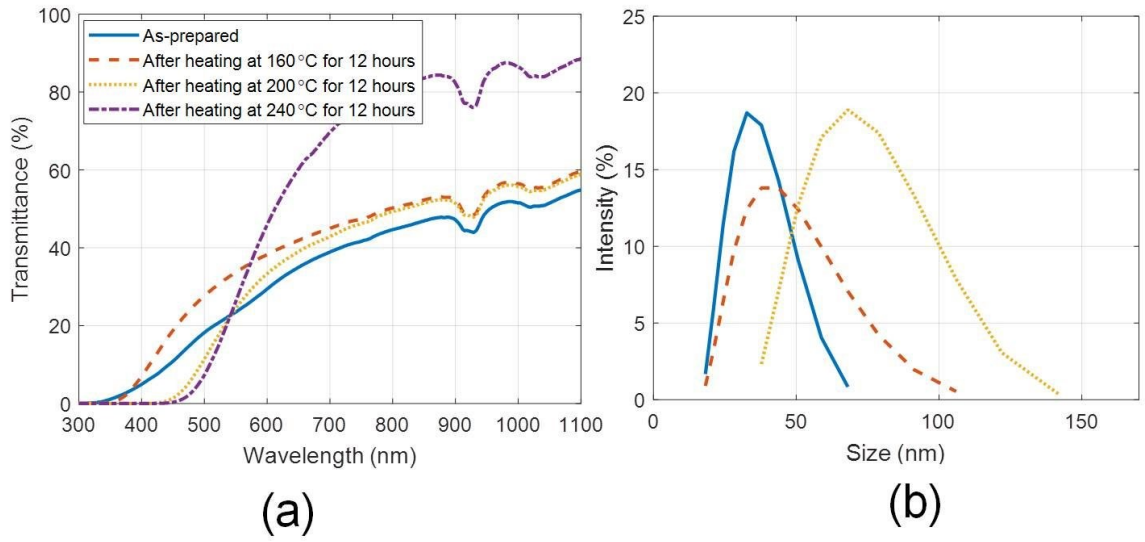

Fig. 3.13 (a) Effect of prolonged heating (for 12 hours) on the (a) optical properties, and (b) hydrodynamic size distribution of the as-prepared nanofluid (5 ml/L).

Instructively, when the constant and cyclic heating tests were carried out by making the container housing the nanofluid 'airtight' (i.e., sealed, to ensure that no outside air enters the container); no agglomeration or settling of the nanoparticles was observed for both constant [see Figs. 3.14(a) and 3.14(b)] as well as cyclic heating tests [see Figs. 3.14(c) and 3.14(d)]. Moreover, nanoparticle size distribution and optical characteristics were retained even after constant heating for 12 hours at 300°C [see Figs. 3.15(a) and 3.15(b)]. However, if the heating period is extended to longer duration (72 hours at 300°C), the particles tend to agglomerate [see Fig. 3.15(d)]. Although, no particle separation was observed, but some thin deposition on the walls of the container (above the liquid free surface) was observed (due to evaporation and subsequent condensation of the nanofluid on the container surface). This resulted in change in optical properties of the nanofluid [see Fig. 3.15(c)].

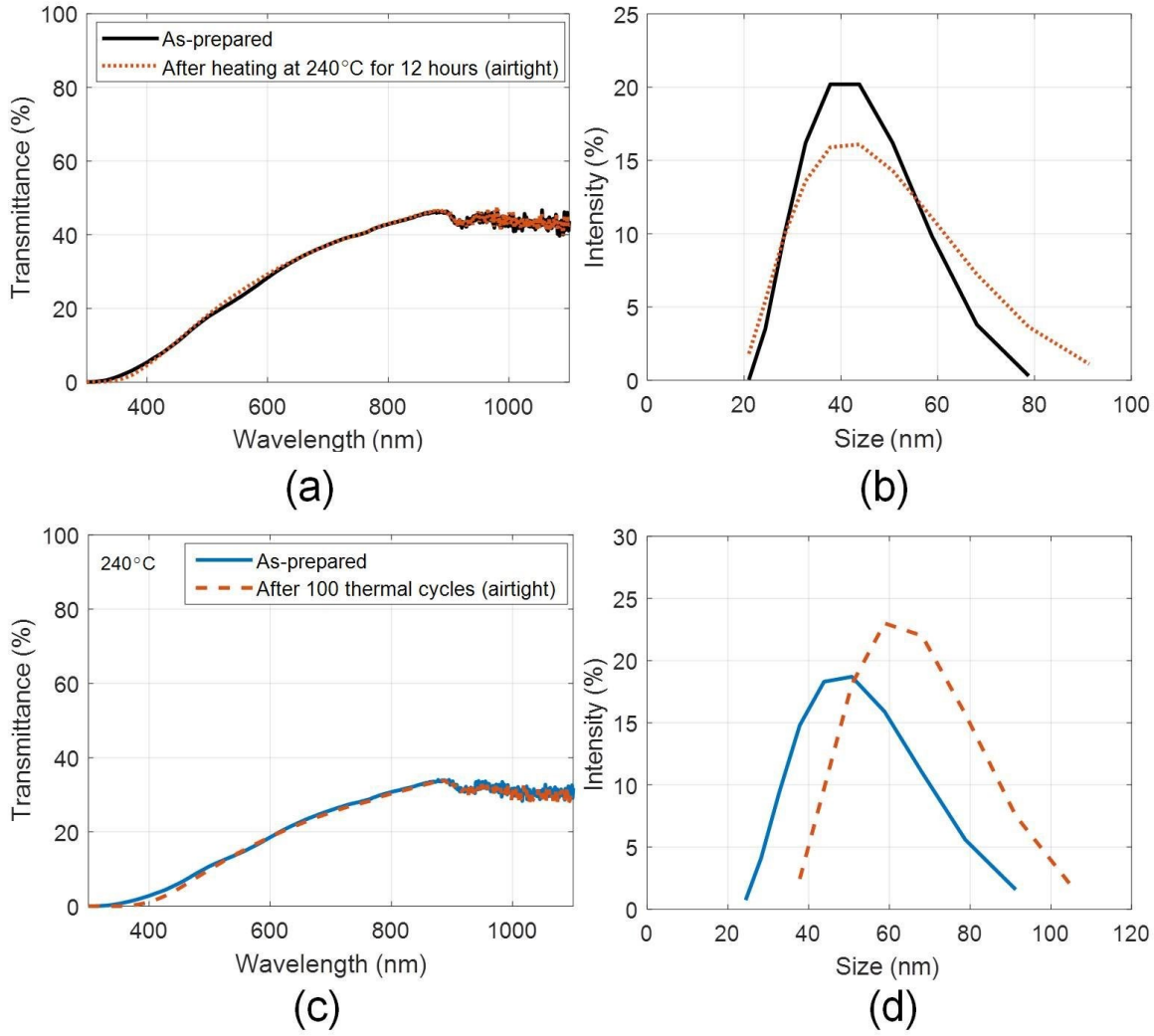

Fig. 3.14 (a) Spectral optical characteristics, and (b) hydrodynamic particle size distribution of the as-prepared and after heating (for 12 hours at 240°C) nanofluid samples; and (c) spectral optical characteristics, and (d) hydrodynamic particle size distribution of the as-prepared and after 100 thermal cycles nanofluid samples (5 ml/L); tested under airtight conditions.

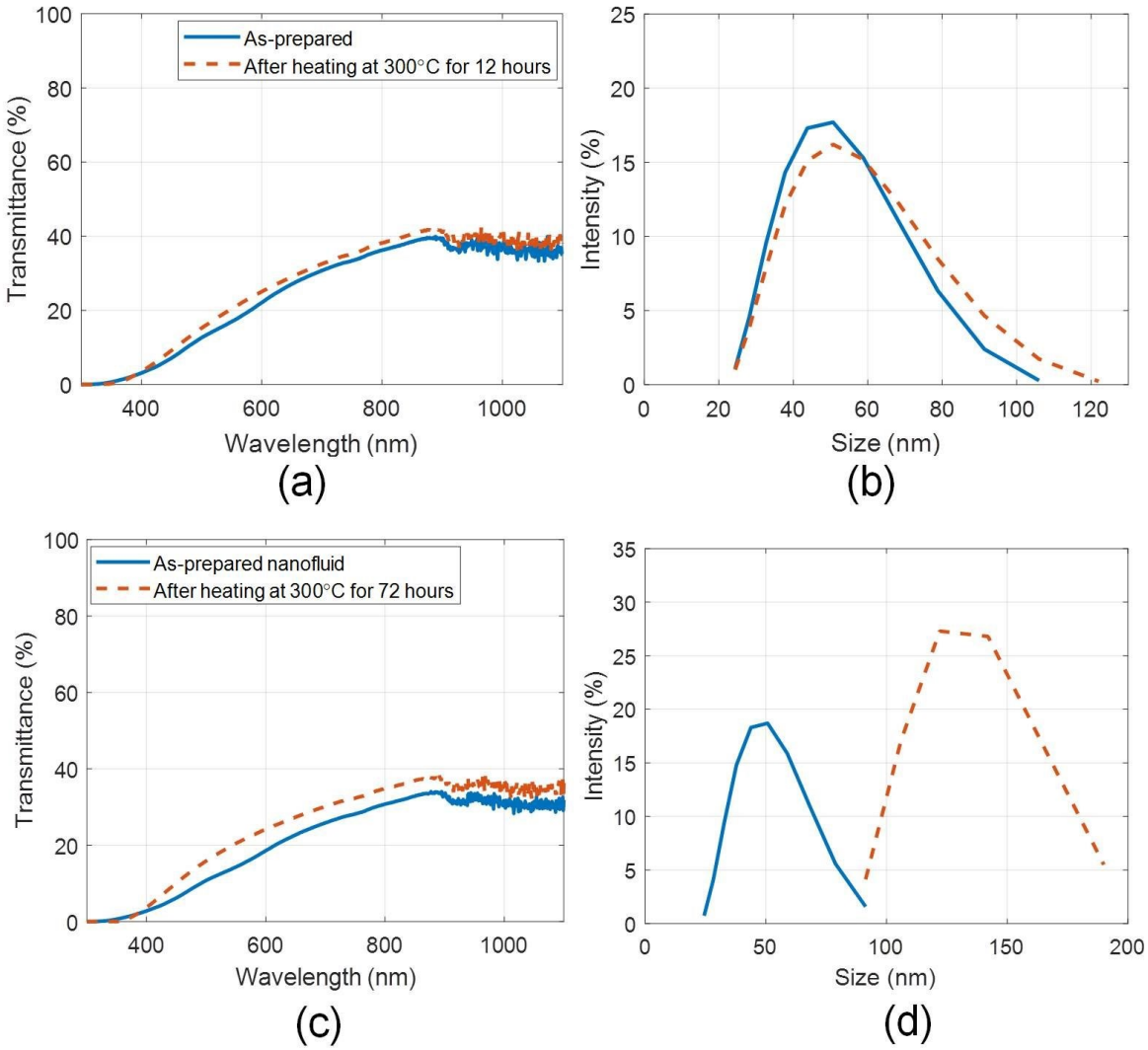

Fig. 3.15 (a) Spectral optical characteristics, and (b) hydrodynamic particle size distribution of the as-prepared and after heating (for 12 hours at 300°C) nanofluid samples; and (c) spectral optical characteristics, and (d) hydrodynamic particle size distribution of the as-prepared and after heating (for 72 hours at 300°C) nanofluid samples (5 ml/L); tested under airtight conditions.

3.5.3 Stability under ultra-violet (UV) light exposure

Although ultraviolet radiations form only a small fraction of the incident solar energy; but given the fact that these are very high energy radiations, and may amount to significant values in case of concentrating solar thermal systems - the as-prepared nanofluids were tested exclusively under UV exposure. UV exposure tests have been done in a custom designed ultraviolet light chamber (photo-chemical reactor). The UV light source being a 125 W (HPL-

N 125W E27, Philips) mercury vapor lamp (outer phosphorous coated cover removed) surrounded with water jacket to maintain a constant temperature of the lamp.

The nanofluid to be tested was housed in a glass tube and was placed at a distance of 70 mm from the UV light source. The incident flux at the location was measured to be 117 ± 2 Wm^{-2} with the help of a thermopile detector (818P-015-18HP, Newport) and power meter (1918-R, Newport, calibrated at λ = 355 nm).

Now, in order to calculate the total exposure energy; Schwarzschild law has been invoked, given by Eq. (4.1) as

$$E = It^{\rho} \tag{3.2}$$

where E is the measured exposed energy, I (= 117 Wm^{-2}) is the light source intensity, t is the time and ρ (= 0.9) is the Schwarzschild coefficient. Exposed energy (E) for 8 hours light exposure amounts to approximately 760 Whm^{-2}.

Now, taking E = 760 Whm^{-2} and peak solar UV intensity (AM 1.5) reaching the nanofluid to be 6.5 Wm^{-2}; Eq. (3) is invoked to calculate t. This comes out to be 198.53 hours (or 24.8 days, with each day of 8 hours sunshine) of peak sunlight, i.e., 8 hours of UV exposure in the UV chamber is equivalent to 24.8 days [69].

In the present work, the nanofluid sample has been tested for 5 UV cycles. Each cycle consisting of 8 hours of UV exposure, followed by 16 hours of darkness (this is in accordance with the procedure given in Ref [69]). In other words, the nanofluid has been effectively tested for 124 days of sunlight exposure.

Interestingly, the nanofluids were found to be stable and retain their properties even after prolonged exposure to UV radiations (see Fig. 3.16) - as there is only a small change in average particle size (~ 2%) and also very less change in the optical characteristics. This is a significant improvement, as exposure to UV radiations has been known to significantly impact the stability of the nanofluids, i.e., extensive agglomeration and settling of the untreated nanoparticles occurs when exposed to UV radiations [69].

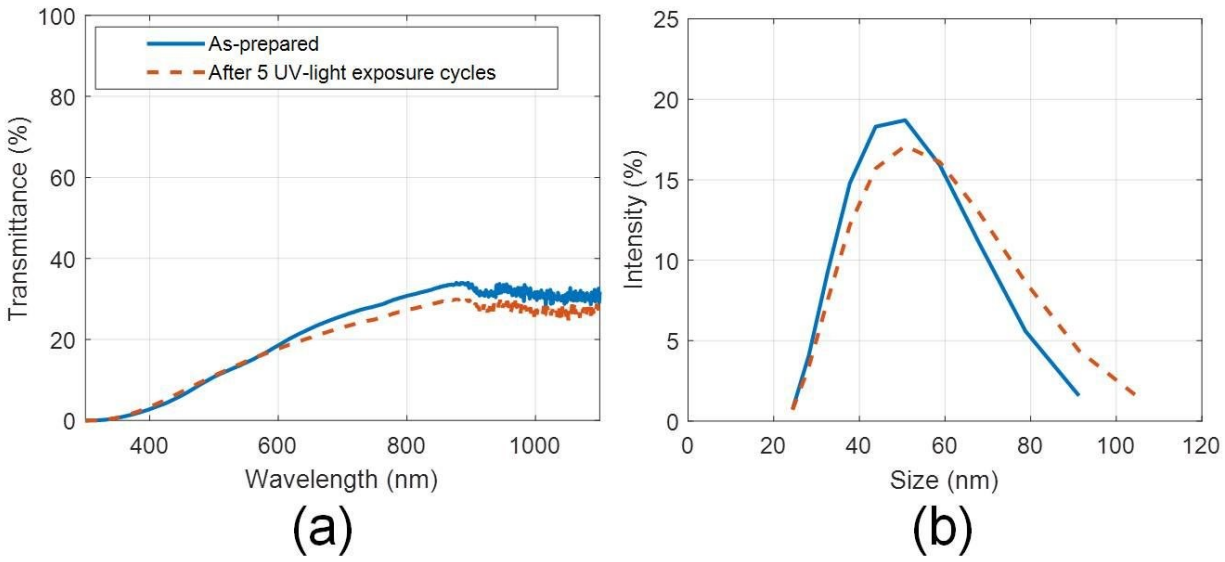

Fig. 3.16 (a) Effect of UV exposure (5 cycles) on the (a) optical properties, and (b) hydrodynamic particle size distribution of the as-prepared nanofluid (5 ml/L).

3.5.4 Stability under prolonged on-sun exposure

In non-concentrating type solar thermal systems, as-prepared nanofluid could be employed as the working fluid. Therefore, it has also been tested for stagnation stability under prolonged on-sun conditions. A fixed quantity of nanofluid having volume fraction f_v = 0.5% has been placed outside under the sun as shown in Fig. 3.17(a).

Average global solar radiation during 3 months' period from 9:00 AM to 5:00 PM has been recorded using pyranometer (Kipp & Zonen) and is shown in Fig. 3.17(d). After 90 days of on-sun exposure, nanofluid is checked for stability, i.e., optical characterization (using UV-VIS-NIR spectrophotometer, Shimadzu UV-2600) and hydrodynamic particle size distribution (using Malvern Zetasizer Nano S ZEN 1600) measurements [see Fig. 3.17(b) and (c)]. There is no visible agglomeration in the dispersion and negligible change in optical characteristics and hydrodynamic particle size distribution even after 3 months of exposure. Therefore, the as-prepared nanofluid is stable and suitable to use as working fluid in non-concentrating type volumetrically absorbing solar thermal systems.

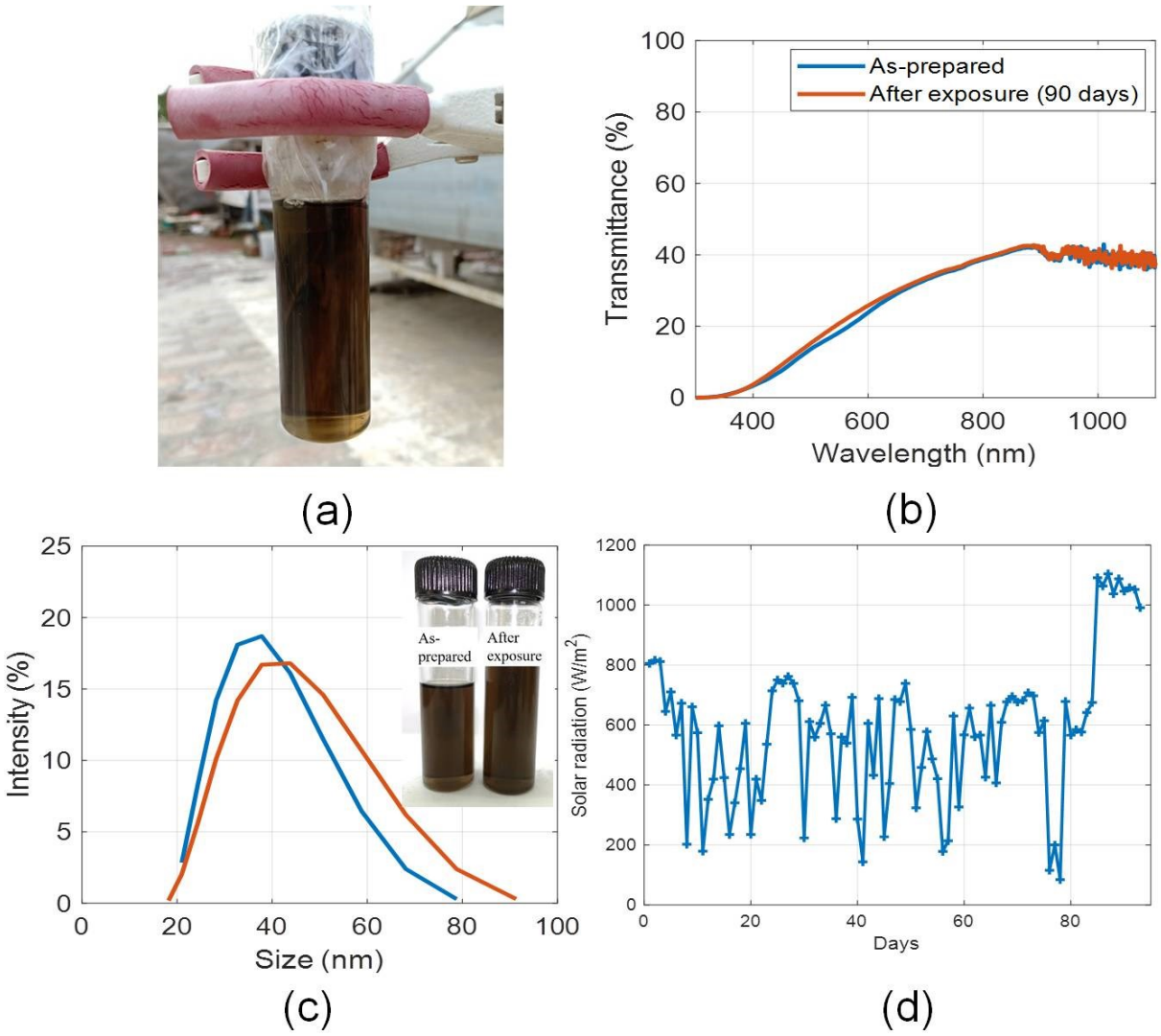

Fig. 3.17 (a) Pictorial view of nanofluid sample under outdoor on-sun exposure (b) spectral optical characteristics (c) hydrodynamic particle size distribution of samples before and after on –sun heating, and (d) solar radiation data for the 90 days of experiment (averaged over each day)

Chapter 4

Experimental investigation of volumetric absorption solar collector

4.1 Introduction

Rigorous testing of the as-prepared nanofluids has revealed that indeed these could operate under real world service conditions without losing their functional properties. Optimum volumetric receiver design (that achieves high thermal efficiency) is the fundamental standing issues in the development of these volumetrically absorbing systems. In volumetric absorption mode, the as-prepared nanofluids (of different concentrations) were examined experimentally. Herein, the nanofluid directly absorbs the energy and convert into thermal energy through non-radiative decay of the absorbed photons. Subsequently, the absorbed energy is transferred to the surrounding medium at staggeringly rapid rate (owing to the extremely small size of the particles). In this chapter nanofluid has been checked volumetrically under stagnation as well as under flow condition. Stability being a key factor, the as prepared nanofluid has been tested for the effect of prolonged concentrated solar energy heating, circulation through pipes/valves and pumping cycles action on the stability (chapter-3). Under experimental conditions, nanofluid interaction with solar receiver constituent materials can alter their properties. The changes in optical and surface properties of solar receiver materials are investigated through spectral optical properties and surface roughness.

4.2 Photo-thermal conversion efficiency

As a first step, optical signatures of various nanofluid concentrations have been measured in the UV-VIS-NIR region (300 nm - 1100 nm). Figure 4.1(a) clearly shows that pure paraffin oil transmits nearly all the incident radiation whereas 20 ml/L nanofluid absorbs nearly in the entire wavelength band; thus giving us a fair idea about the absorption capability of the as-prepared nanofluids. This data was then employed to calculate the solar absorption fraction for different nanofluid concentrations as a function fluid layer thickness as given by Eq. (4.1)

$$\text{Solar absorption fraction} = \frac{\int_{300nm}^{1100nm} S_\lambda \left[1-\exp\left(-K_{a\lambda} y\right)\right] d\lambda}{\int_{300nm}^{1100nm} S_\lambda d\lambda}, \qquad (4.1)$$

where S_λ is the spectral solar irradiance (AM 1.5 spectra), $K_{a\lambda}$ is the spectral absorption coefficient, and y is the fluid layer thickness.

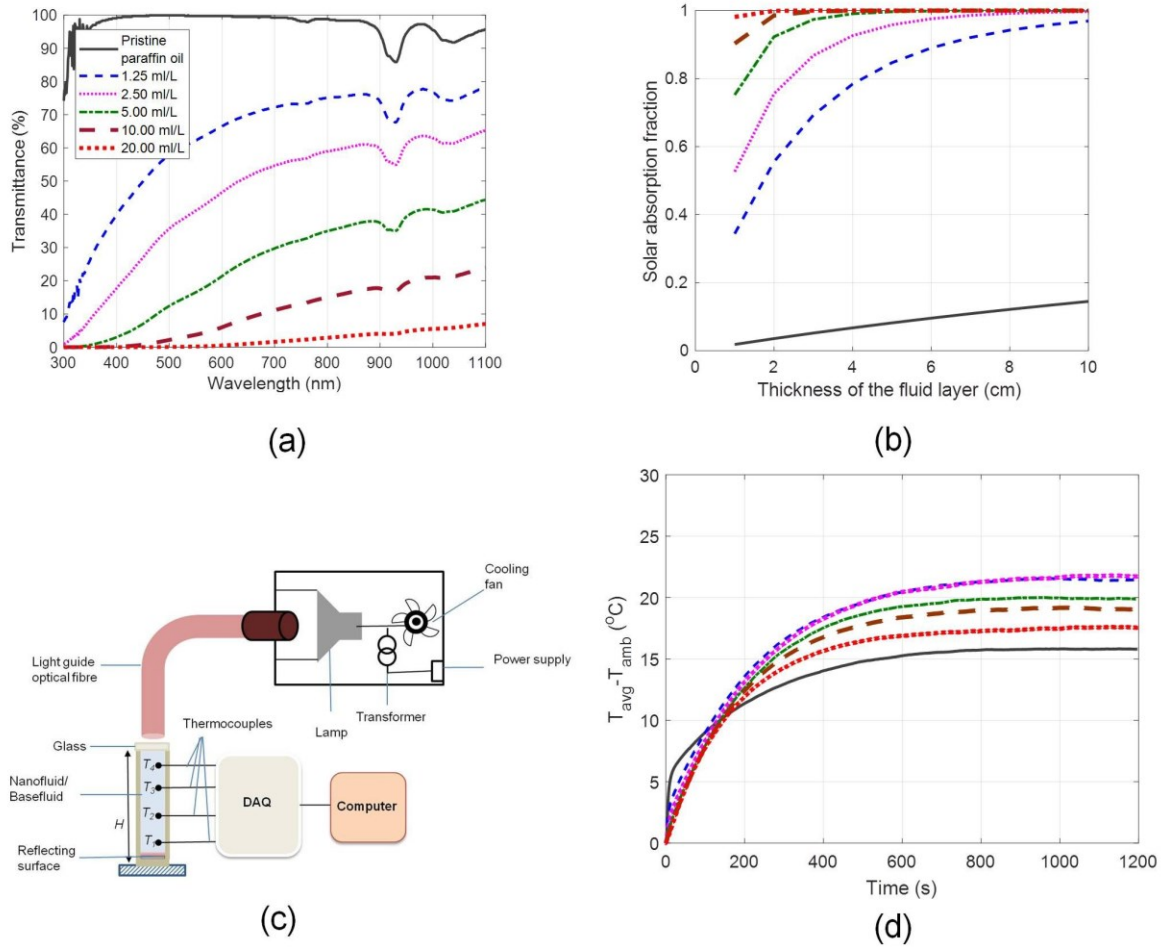

Fig. 4.1 (a) Spectral transmittance of the as-prepared nanofluids in the UV-VIS-NIR region, (b) Solar absorption fraction for various nanofluid concentrations as a function of fluid layer thickness, (c) schematic showing the experimental set-up for photo-thermal conversion experiments, and (d) steady state temperatures for various concentrations of nanofluids. $T_{avg} = (T_1 + T_2 + T_3 + T_4)/4$

Solar absorption fraction essentially gives the fraction of the incident solar energy that could be absorbed by a given thickness of the fluid layer. Clearly, solar absorption capability increases rapidly with increase in concentration. Moreover, to achieve the desired value of solar

absorption fraction, we could either increase the concentration or increase the physical thickness of the nanofluid layer - in effect increasing the optical depth.

In order to clearly gauge the photo-thermal conversion efficiency of the as-prepared nanofluids, laboratory scale experiments have been carefully designed. Nanofluids (housed in a cylindrical column with reflective surface at the bottom) of different concentrations were illuminated with a broad spectrum white light source (Light guide connected to a 3200K color temperature halogen lamp (250 W), Philips) [see Fig. 4.1(c)]. Samples were illuminated until these reached steady state temperatures. These measured steady state temperatures (averaged across the entire depth of the nanofluid column) essentially represent the photo-thermal conversion efficiencies of various nanofluid concentrations under optical heating. Figure 4.1(d) clearly points out that nanofluids have higher steady state temperatures (on the order of ~31 higher) relative to the case of pure paraffin oil.

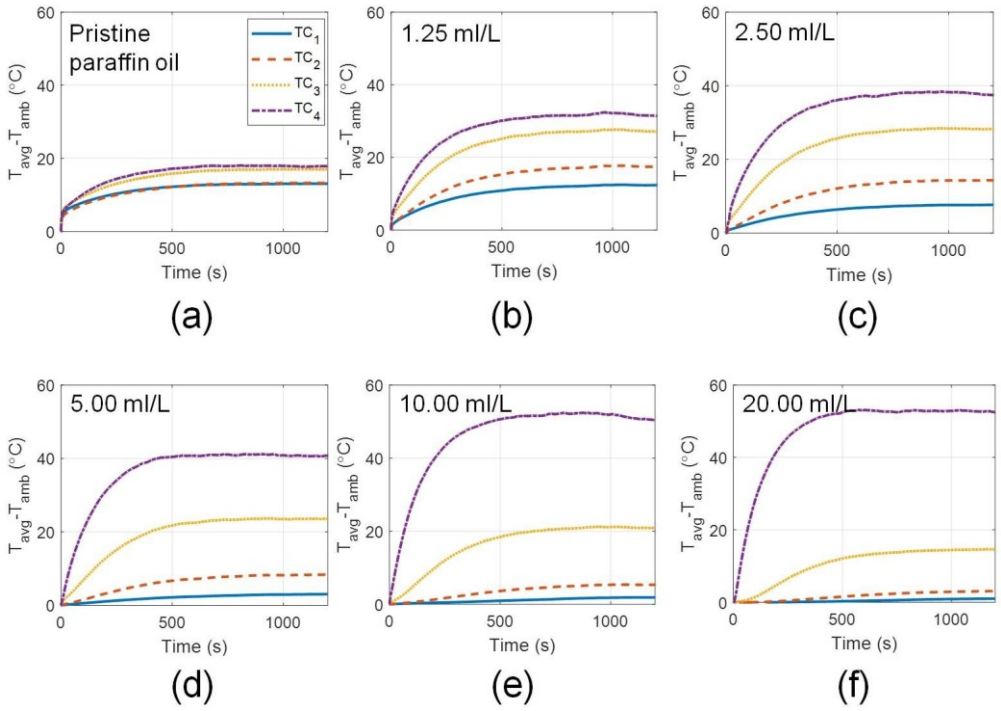

Fig. 4.2 Spatial temperature distribution, when the as-prepared nanofluids are illuminated under a white light source. (a) Pristine paraffin oil, (b) 1.25 ml/L, (c) 2.50 ml/L, (d) 5.00 ml/L, (e) 10.00 ml/L, and (f) 20.00 ml/L.

Interestingly, the highest concentration nanofluid (20 ml/L) does not have the highest photo-thermal conversion efficiency; instead it is highest for the nanofluid with a moderate concentration (2.5 ml/L). This could be understood from the spatial temperature distribution

across the depth of the nanofluid column for various nanofluid concentrations (see Fig. 4.2). Spatial temperature field gives us insights into the photo-thermal conversion process. For a fixed physical thickness of the fluid layer, with increase in nanoparticle concentration, the photo-thermal conversion process tends to be limited to only top layers; not allowing the light to reach the lower layers-hence resulting in lower average steady state temperatures at very high concentrations.

4.3 Thermo-physical properties

Thermal conductivity, viscosity and contact angle are amongst the key thermo-physical properties that impact the redistribution of the absorbed energy within the fluid and pumping power requirements respectively. The as-prepared nanofluids show thermal conductivity (measured using transient hot wire method, KD2 pro) enhancements [see Fig. 4.3(a)] of typically 2-4% (relative to pure paraffin oil); although not a significant enhancement, but could prove to be beneficial under high solar flux conditions.

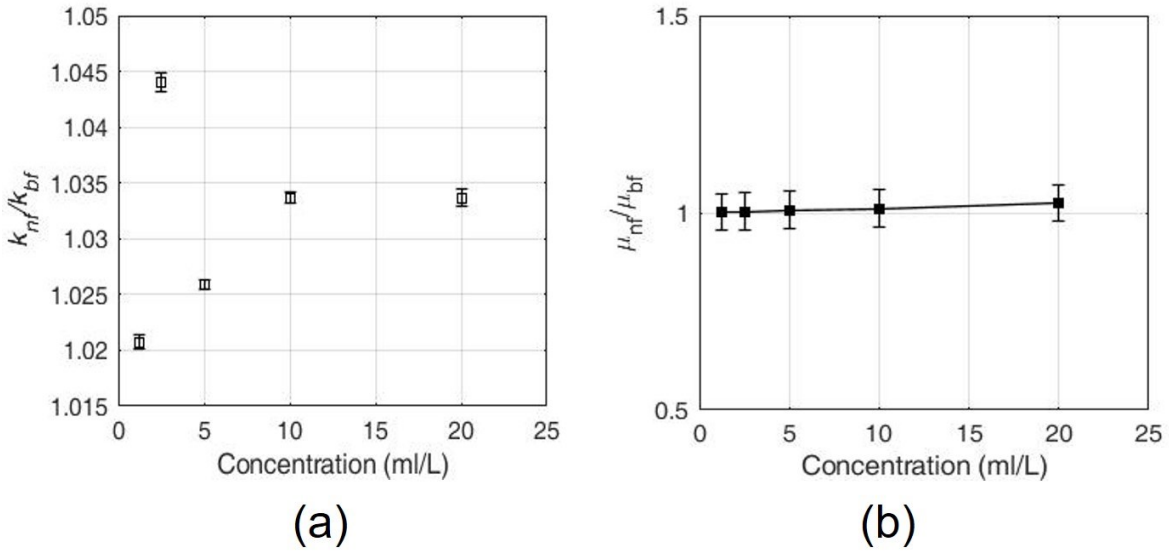

Fig. 4.3 (a) Thermal conductivity ratio (k_{nf}/k_{bf}), and (b) kinematic viscosity ratio (μ_{nf}/μ_{bf}) as a function of nanofluid concentration. Error bar represents the standard deviation and is given by

$$\sigma = \sqrt{\frac{\sum_{i=1}^{n}(\bar{x}-x_i)^2}{n}}$$

Thermal conductivity enhancements may be attributed to the combined effects of ballistic phonon motion, Brownian motion, thermal boundary resistance, and mass difference scattering

[169,170]. However, more detailed work is required to understand the dominant mechanisms resulting in changes in thermal conductivity values.

Viscosity measurements (made using capillary action viscometer) show linear increase in the viscosity with increase in concentration of the nanofluid, the increase being not greater than 2.5% [see Fig. 4.3(b)] even for the highest concentration (20 ml/L). Therefore, there shall not be requirement of additional pumping power when using these fluids in actual practice. Next, the role of contact angle as thermo-physical property and in altering the optical properties has been explored [171]. A contact angle of less than 90° means that the fluid shall wet the surface - i.e., liquid shall adhere to the surface and in effect change its optical properties.

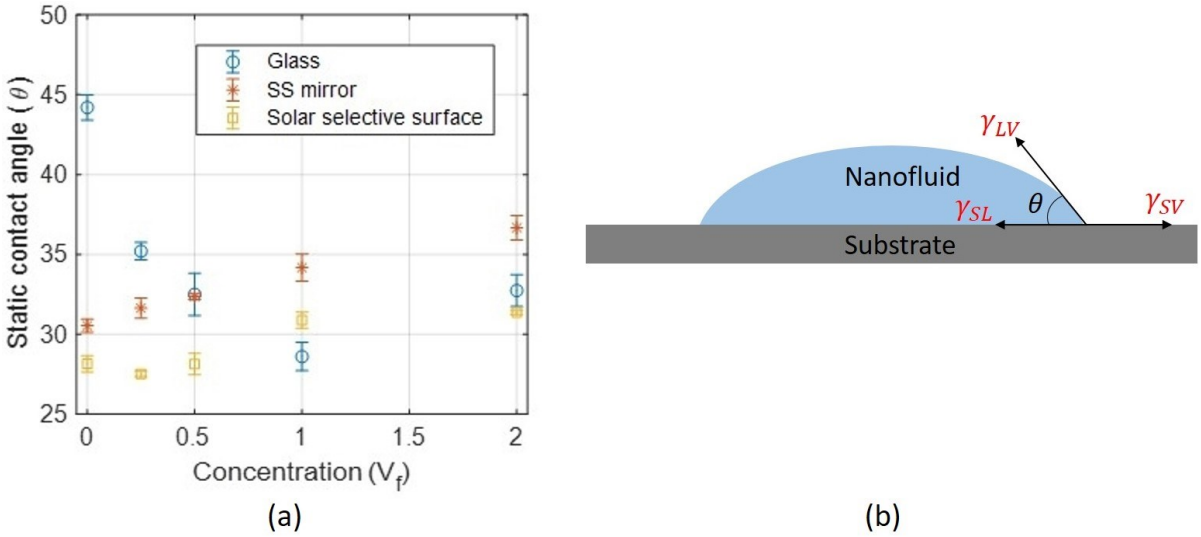

Fig. 4.4 (a) Static contact angle measurements for different concentrations of nanofluid having substrate materials as glass, SS mirror, and solar selective surface, and (b) schematic of interfacial forces at triple point. Error bar represents the standard deviation

Moreover, contact angle shall play a significant role in dictating the flow and heat transfer behaviour in the conduit [172–175]. A goniometer (KRUSS) based on Sessile drop method has been used to measure contact angle. Contact angle as a function of nanoparticles volume fraction for different substrate materials is shown in Fig. 4.4. As per contact angle measurements, it is clear from the graph that nanofluid wets (as $\theta < 90°$) the receiver constituent materials - thus confirming the role of contact angle in altering the optical properties. For a given substrate, the wettability is a function of the volume fraction of the nanoparticles.

In case of SS mirror as the substrate material, the contact angle clearly increases with increase in the volume fraction of the nanoparticles. In case of solar selective surface, it fluctuates

between 28° and 31°. Interestingly, in case of glass, the contact angle decreases up to a particular nanoparticles volume fraction and then starts to increase with further increase in the volume fraction of the nanoparticles.

The wettability is governed by many factor such as (i) physical properties of fluid, substrate and surrounding medium; (ii) homogeneity and non-homogeneity of substrate [176,177].

The static contact angle measured at the interface (solid-liquid-vapour) or triple line is expressed by Young's equation assuming solid surface (smooth, homogenous, rigid, chemically and physically inactive) as

$$\cos\theta = \frac{\gamma_{SV} - \gamma_{SL}}{\gamma_{LV}} \tag{4.2}$$

Where γ_{SV}, γ_{SL}, γ_{LV} are solid-vapour, solid-liquid and liquid-vapour interfacial tension at the triple point shown in Fig. 4.4(b)

Liquid-vapour tension (γ_{LV}) can be measured experimentally with optical tensiometer. It varies by different factors such as interaction between particles, fluid-particles interaction, presence of surfactants in nanofluid, physical properties of nanofluid (density, viscosity).

Solid-liquid tension (γ_{SL}) depends upon the surface morphology, surface potential, adhesive and cohesive forces, nanofluid properties (size, concentration and shape). It is calculated from Young's equation as direct measurement of γ_{SL}, γ_{SV} force in not possible.

Interfacial tension affected by disjoining pressure at triple point. Disjoining pressure further expressed as sum of three components electrical forces (electrostatic interaction), molecular (van der waals interaction) and structural (nanofluid particles in wedge film) forces [176,177].

In the presence of various factor, contact angle mechanism become complex and therefore, an in-depth study is required to clearly identify the dominant forces responsible for the observed results. A more detailed study investigating the mechanisms behind the contact angle variation and effect on heat transfer properties shall be done as a part of the future work.

4.4 Volumetric receiver design

The basic constructional details of various volumetrically absorbing receiver (VAR) designs is given in Fig. 4.5. Further, in order to get the 'big picture' the reported works are carefully categorized - flow/non-flow, indoor/outdoor, and concentrating/non-concentrating. In relation to volumetric receiver design; numerous receiver design configurations have been reported in the literature
[3,37,107,111,123,127,131–135,139,74,140–142,144,178,75,79,83,85,95,96,105].

Careful look into these designs reveal that the receiver walls housing the nanofluid either are made of glass or glass/black surface combination. The former configuration has the advantage of efficiently capturing the incident concentrated sunlight. There are operational issues, which need to be addressed to realize a practically robust 'total glass' receiver design. Moreover, at low nanoparticle volume fractions, some part of the incident concentrated sunlight may go unutilized. On the other hand, at high volume fractions of nanoparticles, the system emulates surface absorption. Therefore, it is imperative to make sure that all the incident energy is captured at low nanoparticles volume fractions to ensure volumetric absorption.

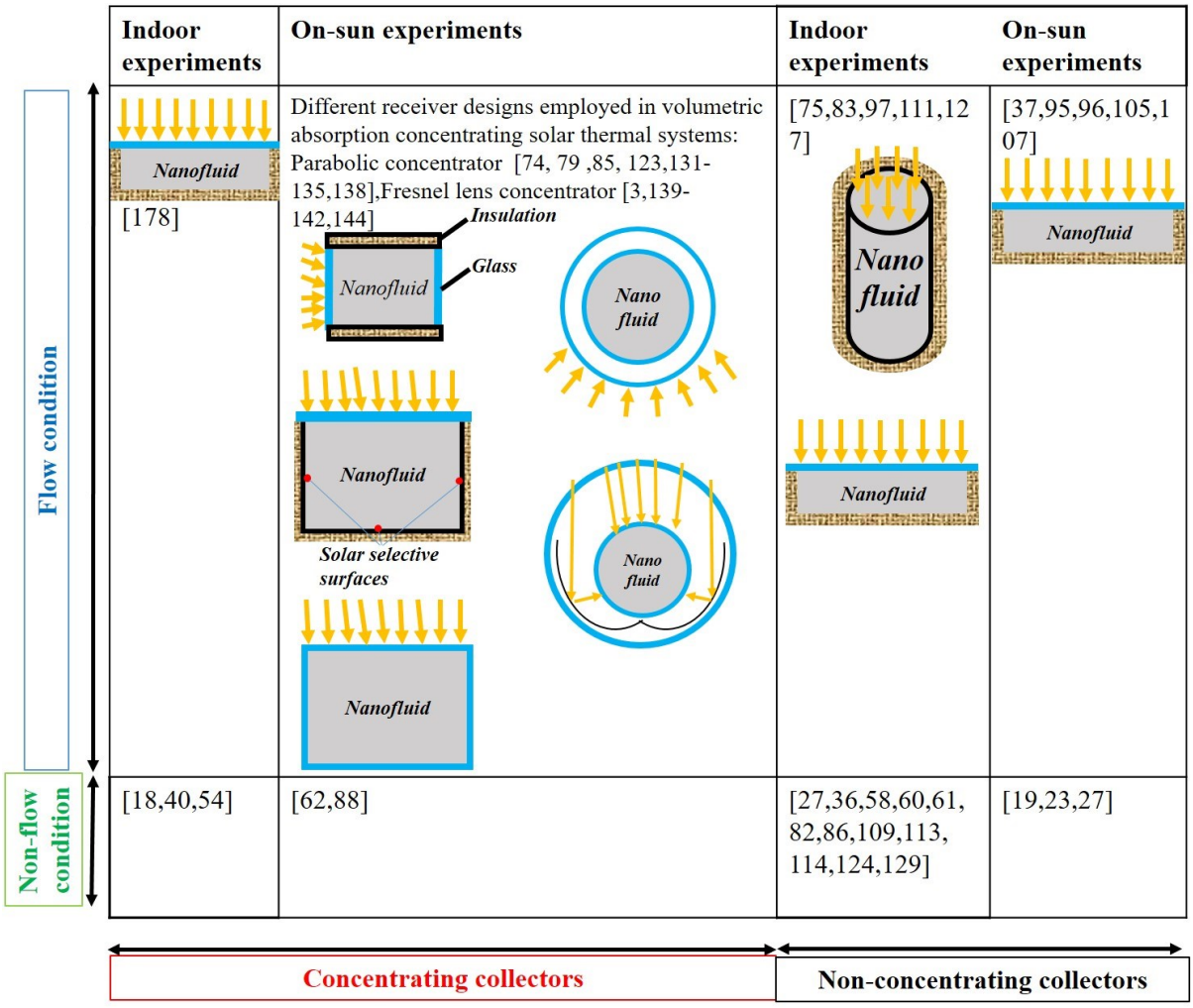

Fig. 4.5 Selected works relevant to VAR designs under various operating conditions.

4.5 Design and test circuit of the as-prepared nanofluid based volumetric absorption solar thermal platform

A novel nanofluid based volumetric absorption solar thermal system with inner reflecting surfaces has been designed and fabricated. All the experiments on the receiver have been

performed under the on-sun condition with a solar thermal system having geometric concentration ratio (GCR) = 20.

We have designed a volumetrically absorbing solar thermal system, wherein a linear Fresnel lens is used to concentrate the incident normal solar irradiance onto the receiver lying along the focal line of the concentrator. The receiver is essentially a closed rectangular conduit in which the fluid is made to flow.

In volumetric absorption mode, the as-prepared nanofluids (of different concentrations) were made to flow through the receiver. Herein, the nanofluid directly absorbs the solar energy - nanoparticles owing to their broad wavelength absorption characteristics; convert the solar energy into thermal energy through non-radiative decay of the absorbed photons. Subsequently, the absorbed energy is transferred to the surrounding medium at staggeringly rapid rate (owing to the extremely small size of the particles). This results in efficient photo-thermal conversion of the incident solar energy.

4.5.1 Receiver design and constructional details

The most important part of any solar thermal system is its receiver design as it significantly influences the performance characteristics. In the present work, a volumetrically absorbing receiver with rectangular cross-section has been designed and fabricated [see Fig. 4.6(a) and 4.6(b)].

Topside of the receiver is transparent, whereas, the remaining three sides are reflecting. A 2mm layer of silicon and polyethylene foam sheet is employed to insulate the receiver. Spectral transmittance and specular reflectance values (measured using spectrophotometer) of materials used to fabricate the receiver are shown in Fig. 4.6(c). Reflecting 'side' and 'bottom' walls facilitate testing of large range of nanofluids (nanoparticles volume fractions). Moreover, 'reflecting walls' effectively increase the optical depth without having the need to increase the physical depth and/or the nanoparticles volume fraction. Therefore, this configuration retains its volumetric absorption characteristics in a relatively large range of nanoparticles volume fractions.

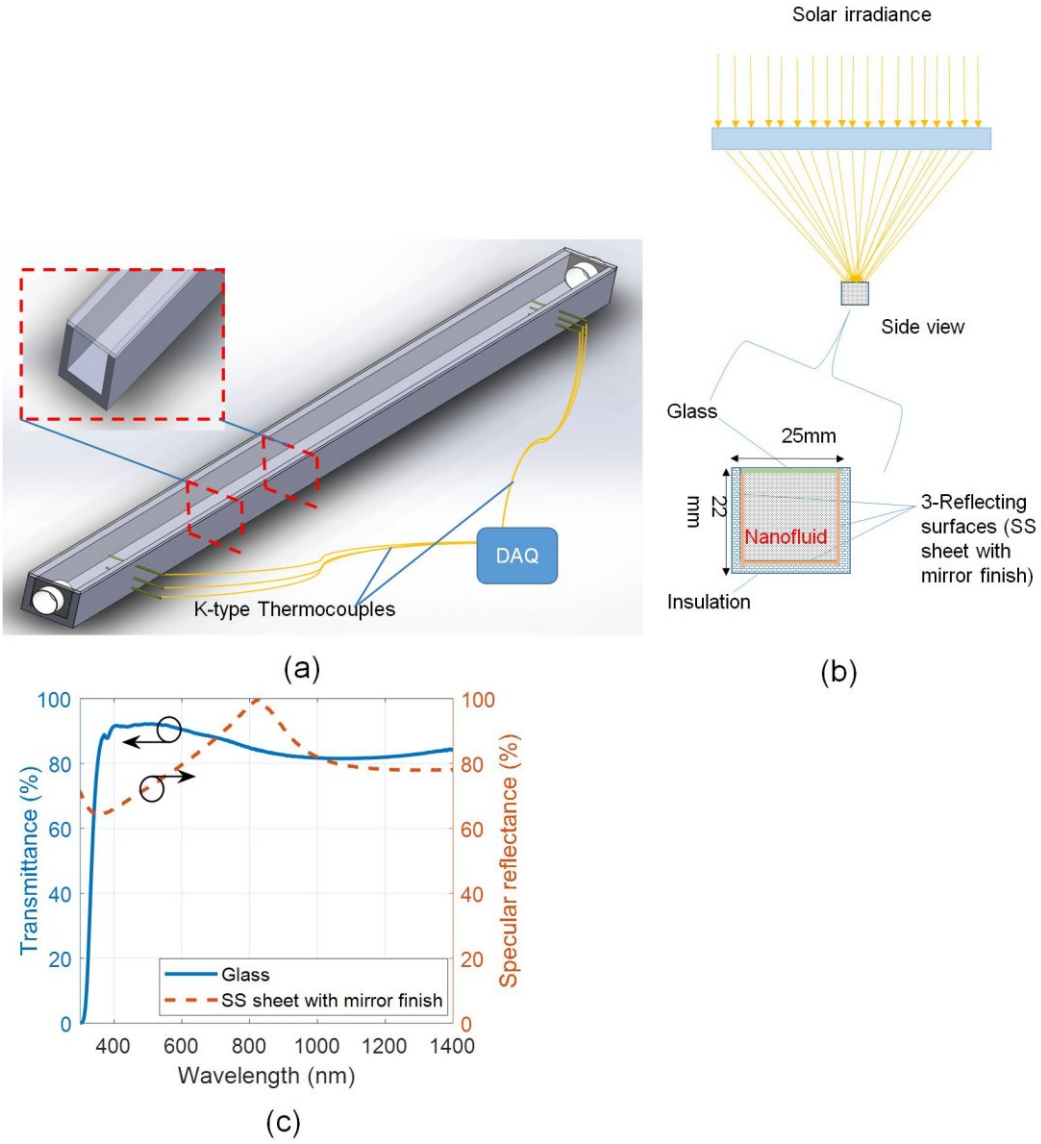

Fig.4.6 (a) Schematic showing the (a) basic design, (b) side view and the geometrical details of the receiver design, and (c) spectral transmittance of glass and specular reflectance of the stainless steel sheet used to build the receiver.

4.5.2 On-sun experimentation test circuit

To assess the stability of the as-prepared nanofluid and the performance of the volumetric receiver design under the sun, an experimental test circuit is designed. Figure 4.7 shows the schematic of the test circuit employed in the present work.

The test circuit comprises of a dual-axis solar tracker, receiver, positive displacement gear pump, data acquisition system, pipes, valves, and storage tank. Receiver, pipes and storage tank are insulated to minimize thermal losses. A positive displacement gear pump (Liquiflo) is employed to maintain a constant flow rate of (0.5 l/pm (8.33×10^{-6} m^3s^{-1}) across the collector.

To measure the temperature of the circulating fluid, six K-type thermocouples are inserted across the depth (three each) at inlet and outlet sections. One thermocouple is up in the air in shadow to measure the ambient temperature. All the temperature readings are logged using a data acquisition system (NI, cDAQ-9721 using LabVIEW platform). Direct normal incidence (DNI) radiation is measured using a ring shaded pyranometer (Kipp and Zonen). Various geometrical dimensions of the solar concentrating system and the receiver used in the study are detailed in Table 4.1.

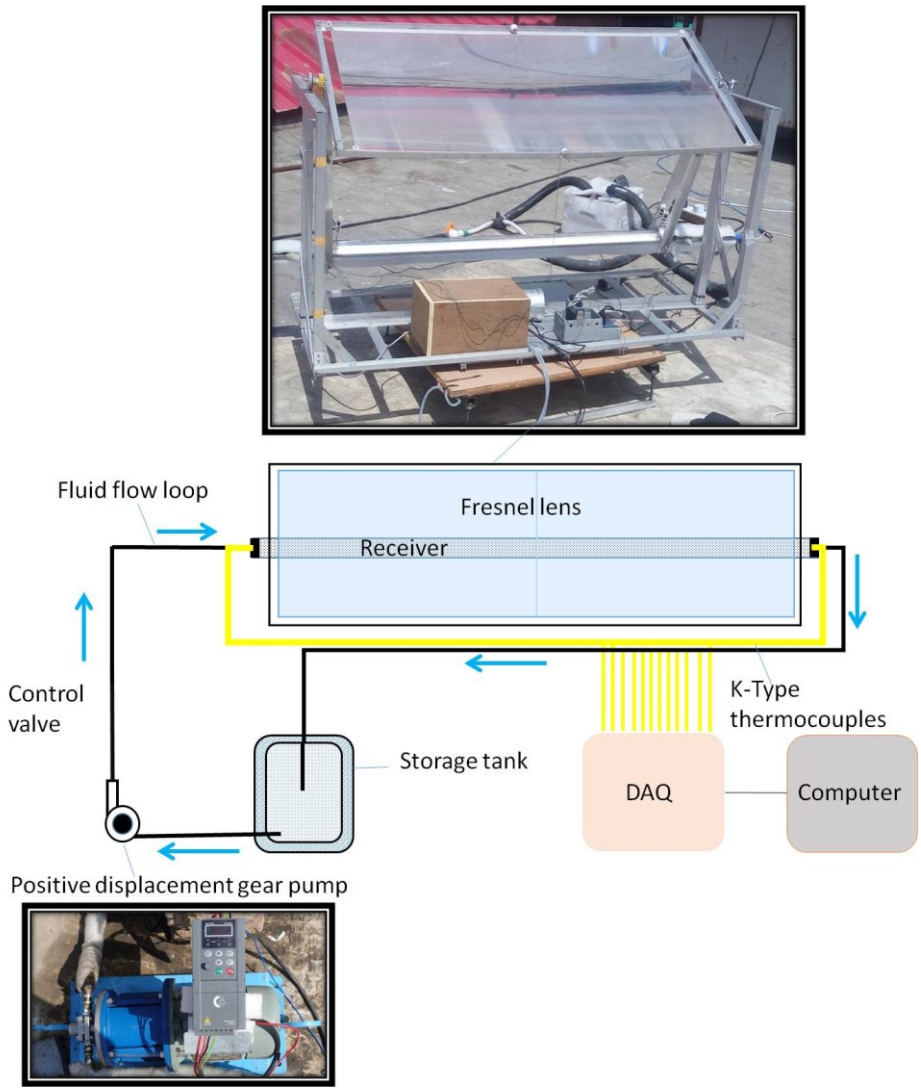

Fig.4.7 The experimental test circuit employed for on-sun testing.

Table 4.1 Geometrical details of solar concentrating system and the receiver.

Components of VASC	**Parameter**	**Dimensions**
Concentrator (Fresnel lens)	Length	1000 mm
	Width	500 mm
	Focal length of the concentrator	500 mm
	Focal line width	25 mm
	Aperture area	0.5 m^2
	Lens thickness	3 mm
	Lens material	PMMA
	Optical efficiency	90%
Receiver	*L*	1000 mm (concentrating)
	B	25 mm
	W	22 mm
	Glass thickness	2 mm

4.6. On-sun performance of the receiver

4.6.1 Time constant

The Time constant is an important parameter for solar thermal systems when operating under transient outdoor conditions. Its value gives the response time of the system to stabilize to its steady state performance characteristics after a sudden fluctuation in operating conditions (such as sudden change in solar irradiation value due to clouds) has happened. Moreover, time constant is a very useful parameter to gauge the thermal mass (heat capacity) of the receiver - more the time constant value, larger the heat capacity [179–181]. In the present work, the time constant of the designed receiver has been measured as per the ASHRAE standards [179]. Initially, the receiver is deliberately shaded so that there is no solar flux incident on the receiver. The fluid inlet temperature is set close to atmospheric temperature. Subsequently, the solar tracker is started, and within few seconds, concentrated radiation incident on the receiver. Average DNI (direct normal irradiance) measured to equal 586 Wm^{-2} during the experiment (Ring shaded Pyranometer, Kipp & Zonen). The temperature at the outlet is noted until it reaches steady state i.e. rate of increase in outlet temperature of the nanofluid is not greater than 1° per minute. Receiver time constant is the time needed by receiver to vary the

temperature of nanofluid, 63.2% of its steady state value when a sudden change occurs in the incident solar radiation [179] (mathematically given by Eq. 4.4). The time constant of present volumetric absorption solar receiver is 60 seconds (that means the receiver stabilizes fast). Increment in receiver outlet temperature above ambient has been plotted against elapsed time in Fig 4.8.

$$(T_{out} - T_{atm})_{initial} = 0.632 \times ((T_{out} - T_{atm})_{final} \tag{4.3}$$

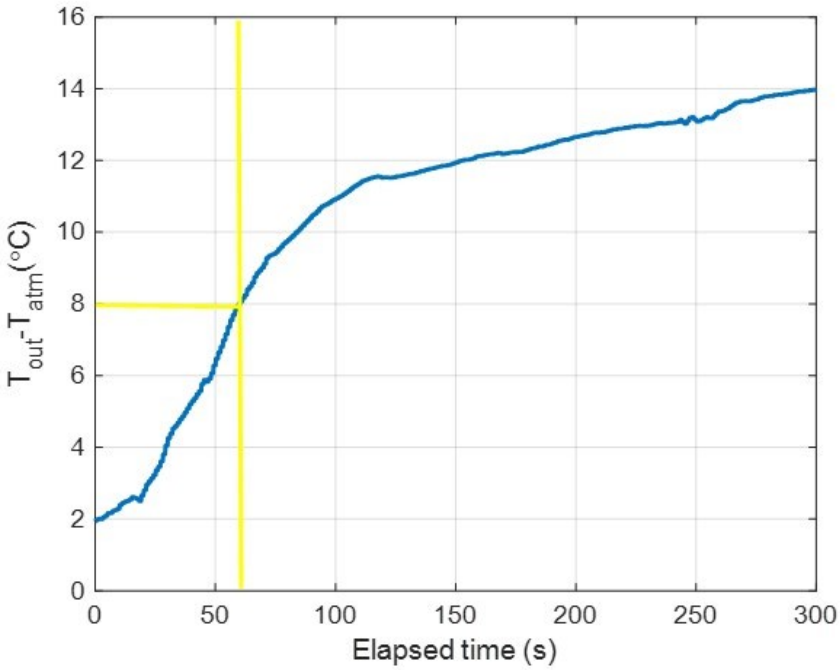

Fig.4.8 Time constant of VAR for f_v = 0.5%.

4.6.2 Steady state thermal efficiency of the receiver

Steady-state thermal efficiency defined as the ratio of sensible heat gain by heat transfer fluid (nanofluid) to the incident solar irradiance on the receiver and is given by Eq. (4.5) as

$$\eta_{th} = \frac{mc_p(T_{out} - T_{in})}{CG} \tag{4.4}$$

Wherein, C is concentration ratio and G is direct solar radiation (Wm^{-2}). For a given volume fraction of nanoparticles, at least three experiments are carried out to ensure repeatability. Each experiment is carried out for a period of 30 minutes at a constant flow rate of 0.5 l/pm. The temperatures at the inlet and outlet are recorded and then these values are employed to calculate

the receiver efficiency. This aforementioned exercise is repeated for various volume fractions of the nanoparticles. Steady state thermal efficiency as a function of nanoparticles volume fraction is plotted in Fig. 4.9. Interestingly, the efficiency increases with increase in volume fraction up to a point and then starts to decrease as the volume fraction is further increased. This may be attributed to the fact that up to a particular limit, increasing the nanoparticles volume fraction enhances the solar absorption capability. However, further increase in nanoparticles volume fraction results in absorption of the incident sunlight within few fluid layers at the surface. Thus, not allowing the sunlight to interact with the bulk of the fluid - rendering the average nanofluid temperature increase to be low.

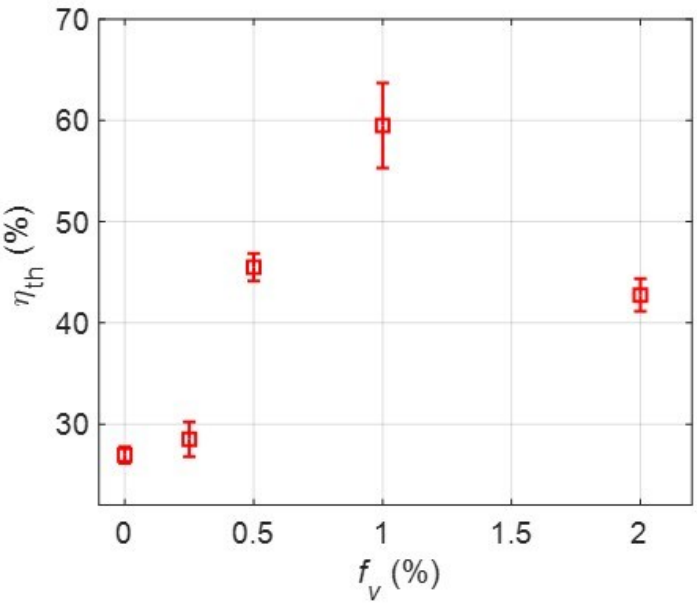

Fig. 4.9 Steady state thermal efficiency for the different volume fractions of nanoparticles. Error has been calculated by uncertainity analysis as $\left(\sigma_\eta = \sqrt{\left(\frac{\Delta\eta}{\Delta T}\Delta T\right)^2 + \left(\frac{\Delta\eta}{\Delta G}\Delta G\right)^2}\right)$. Here σ_η is error corresponding to thermal efficiency and ΔT, ΔG represents variation in temperature and direct solar irradiation for each experiment.

In the present work, maximum steady-state thermal efficiency of ~60% could be achieved (η_{th} = 59 ± 5.5% at f_v = 1%). In comparison with the volumetric absorption systems (operating in similar temperature range) reported in the literature, our system's thermal efficiency (59% collector efficiency at 72°C) is indeed of the same order as reported in the literature (54% collector efficiency at 80°C [142]).

Employing anti-reflective coated glass as well as by incorporating a glass envelope could further improve the system efficiency.

4.7 Stability of the as-prepared nanofluid

4.7.1 Effect of exposure to concentrated solar energy heating and pumping cycles on the stability of the as-prepared nanofluid

In VARs the nanofluid has to interact directly with concentrated solar radiation and has to flow through pipes, valve and the pumping system.

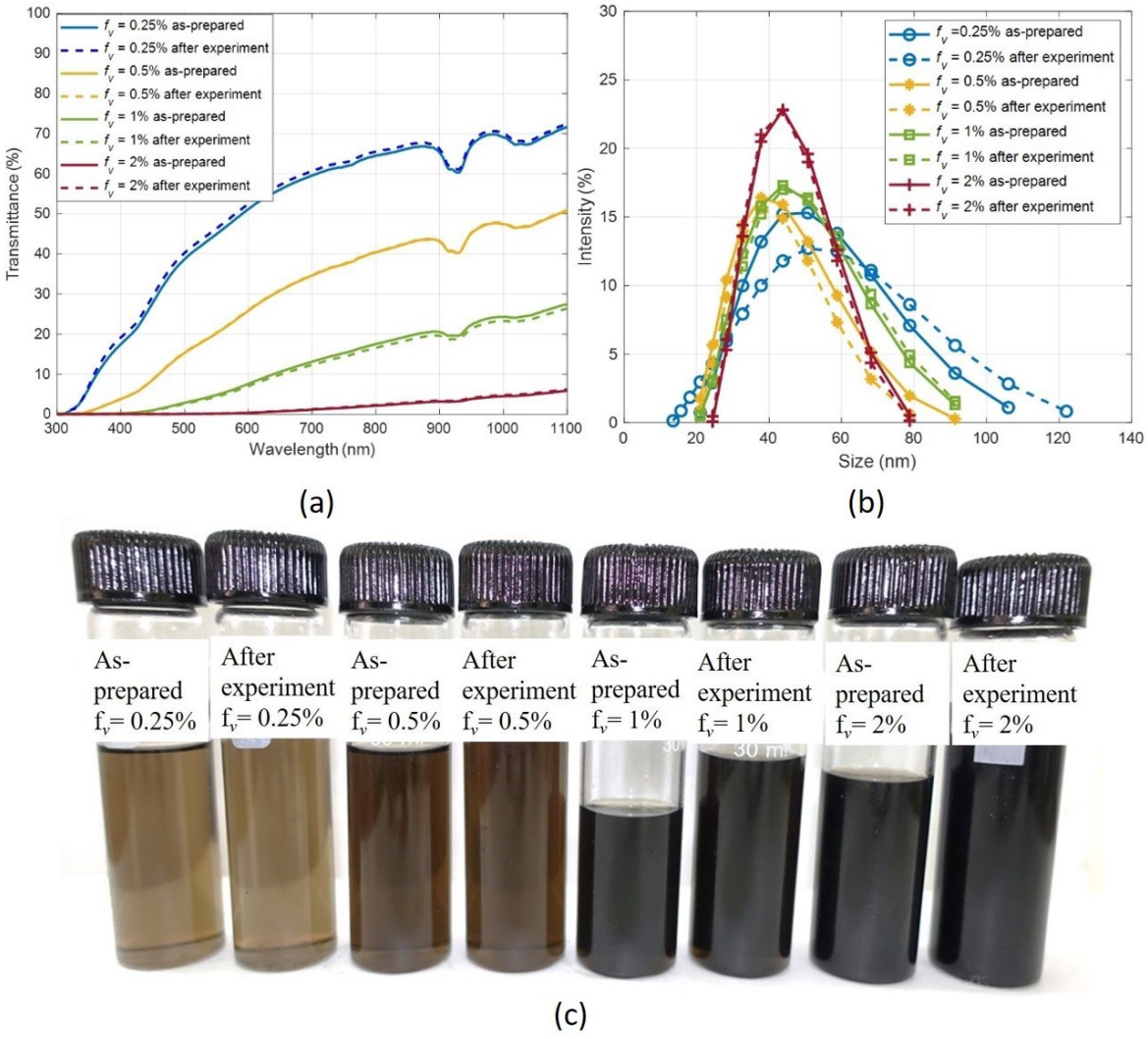

Fig. 4.10 (a) Spectral optical characteristics, and (b) hydrodynamic particle size distribution for the different volume fraction of nanoparticles, sample taken before and after the on-sun testing, and (c) photographs of different concentrations of nanofluid samples (as-prepared and after experiments).

Concentrated radiation can affect the dispersion stability of nanofluid, which ultimately affects the overall performance of the system. The agglomeration of nanoparticles will not only affect the overall system efficiency but also can lead to erosion and wear of parts of the solar thermal system. Therefore, it is imperative to assess the impact of concentrated solar irradiance and pumping cycles under on-sun conditions on the stability of the as-prepared nanofluid. The nanofluid stability has been examined through spectral transmittance and hydrodynamic particle size measurements of nanofluid samples taken before and after each experiment as shown in Fig. 4.10. There is negligible variation in nanofluid transmittance even after 1.5 hours of concentrated heating and pumping cycles under the on-sun conditions. Figure 4.10(c) shows pictures of nanofluid samples (different nanoparticles volume fractions) before and after the experiments. It can be concluded that as-prepared nanofluids retain their stability even after moving through the flow loops, pump, temperature variation and concentrated solar flux.

4.8 Effect of nanofluid interaction on VAR constituent materials

When as-prepared nanofluid is used as the working fluid in VAR, it has to interact with glass, reflecting surfaces of the receiver. In realistic outdoor operation, as the time progresses, nanofluid interaction can alter the optical and surface properties of the receiver constituent surfaces, which shall further affect the overall system performance.

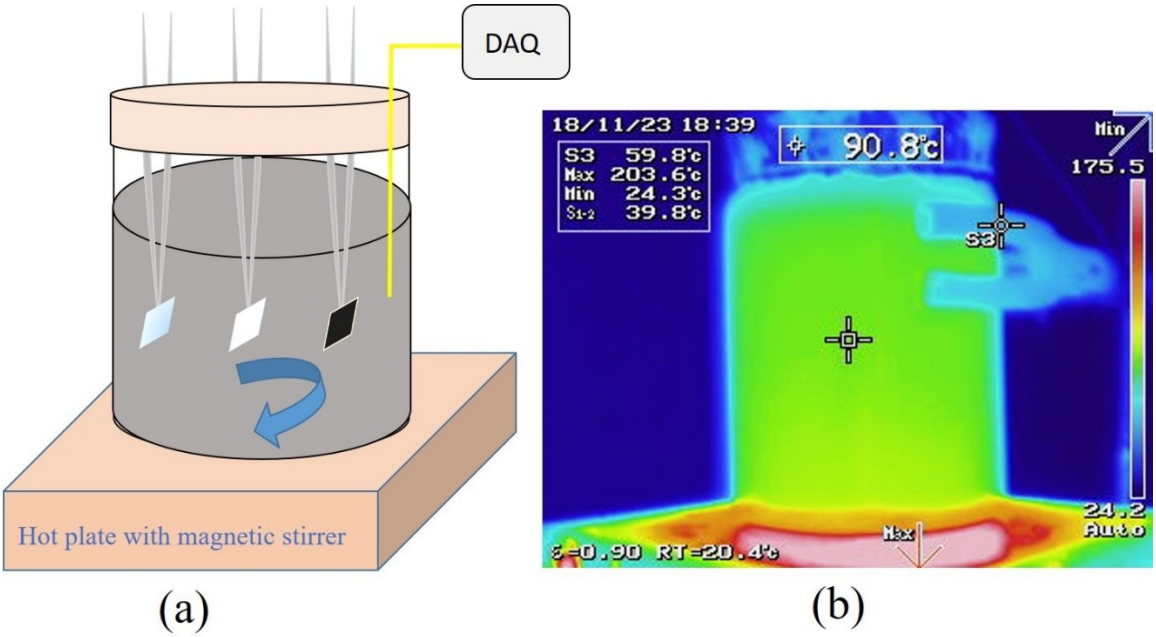

Fig. 4.11 (a) Schematic diagram, and (b) IR-image of experimental set up developed for testing nanofluid interaction effect on solar receiver constituent materials (infrared camera, Keysight).

Researchers have reported adhesion of nanoparticles on the walls of receiver in hybrid CPV/T system [182]. The nanoparticles (metallic or non-metallic) erosive effect when comes in contact with common industry material has also been reported in the literature [183–188]. Therefore, any nanofluid should be assessed for its interaction with the system components before accepting it for actual applications. A set-up is designed to assess the effect of as-prepared nanofluid on solar receiver surface materials. Constituent materials samples (glass, SS sheet mirror, solar selective surface) have been suspended in the glass enclosure as shown in Fig. 4.11. The glass enclosure filled with nanofluid having f_v=1% is placed on a hot plate (Metal top and ceramic based hot plates) with a magnetic stirrer. Magnetic bar rotation is fixed at 1800 rpm for maintaining continuous flow over the sample surfaces - simulating flow condition and the heater ensures that the nanofluid temperature remains at 100°C. The experiment is conducted for 10 days (12 hours/day). In lieu of the fact that some hybrid solar volumetric absorption receiver designs employ solar selective surfaces(SSS) [189], these surfaces have also been included for assessing the effect of nanofluid interaction.

4.8.1 Effect of nanofluid interaction on the transmittance of glass

Interaction with nanofluid can affect the transmissivity of the glass [τ_{sw}, solar weighted transmittance, defined by Eq. (4.5)]. This in turn can affect the optical efficiency [$\eta_{optical}$, defined by Eq. (4.6)] and hence the thermal efficiency of the system. Moreover, the optical efficiency of the system dictates the magnitude of the solar radiant energy flux that is able to reach the nanofluid.

$$\tau_{SW} = \frac{\int_{300nm}^{1400nm} S_\lambda \exp(-K_{a\lambda} y) d\lambda}{\int_{300nm}^{1400nm} S_\lambda d\lambda} \tag{4.5}$$

$$\eta_{optical} = \frac{G_r}{CG} \tag{4.6}$$

where

$$G_r = CG\eta_{lens}\tau_{sw}K_i(\theta) \tag{4.7}$$

and

$$C = \frac{A_{lens}}{A_{rec}} \tag{4.8}$$

Wherein, $K_i(\theta)$ is incident angle modifier, C is concentration ratio, G is direct solar irradiation (Wm^{-2}), and θ is the angle which concentrated radiation makes with normal to the receiver surface. In the present work, the maximum value of the aforementioned incident angle has been calculated (as per geometrical dimensions of the concentrator and the receiver) and equals 25.40°. This value of θ is within the range (<30°) in which the value of $K_i(\theta)$ is nearly unity [142,179]. Noting that $\eta_{lens} = 0.90$, $\tau_{sw} = 86.81$, and $K_i(\theta) = 1$, we get $\eta_{optical}$ =78.12%.

After 120 hours of interaction, the samples have been checked for their optical properties like transmittance, specular and diffuse reflectance through spectrophotometry. The effect on the transmittance of glass due to nanoparticle interaction is shown in Fig. 4.12.

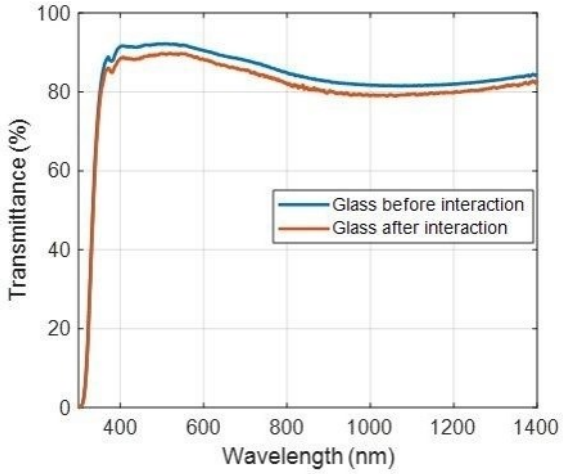

Fig. 4.12 Nanofluid interaction effect on the transmittance of glass.

Transmittance data is used to calculate the solar weighted transmittance of glass before and after the interaction. Now, due to the interaction of the nanofluid with the glass, there is reduction in the solar weighted transmittance of glass from 86.81% to 84.32% (a decrease of ~2.24%). Optical efficiency being a function of solar weighted transmittance also reduces by ~2.24%; which in turn affects the useful energy gain and the thermal efficiency of the system. Hence, interaction of nanofluid with VAR constituent materials does affect the overall performance of the system.

4.8.2 Effect of nanofluid interaction on the reflectance of VAR constituent materials

The effect of nanofluid interaction on diffuse and specular reflectance of solar receiver constituent materials is also examined. There is a small change in specular and diffuse reflectance for all three materials as shown in Fig. 4.13. Overall, the difference in optical characteristics due to nanofluid interaction can be attributed to the change in surface properties such as surface roughness and contact angle. Changes in surface roughness can not only change optical properties but also can alter flow behaviour within the conduit. The surface roughness of specimens before and after the experiment has been measured with a portable surface roughness tester (Mitutoyo SJ-400). There is negligible change in the average roughness (R_a) of all the three samples [Glass (0.03 μm), SS sheet (0.03 μm), and solar selective surface (0.12 μm)]. It may be noted that the change in roughness could be less than 5nm as least count of measuring instrument is 5 nm.

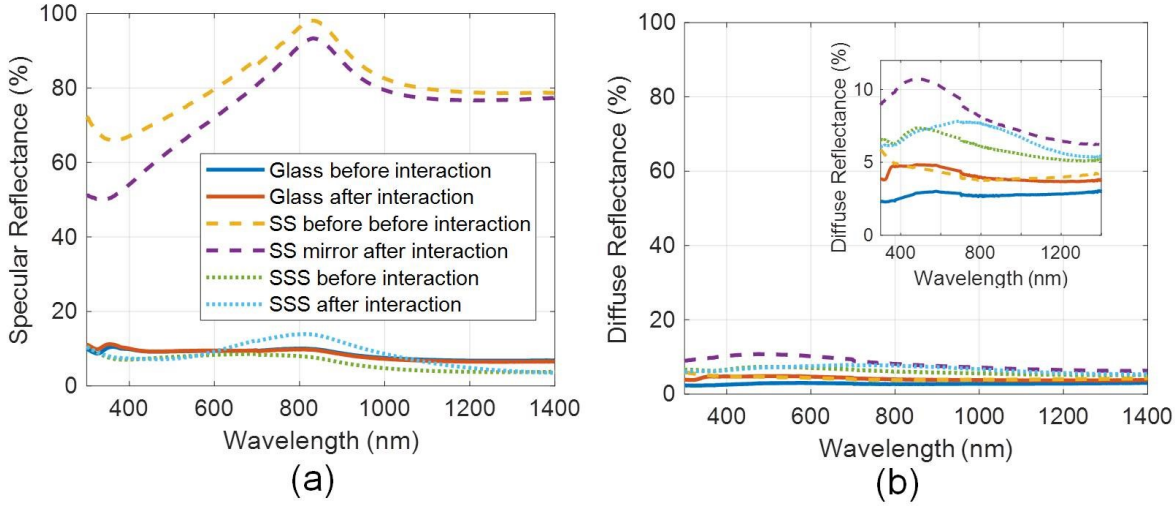

Fig. 4.13 (a) Specular, and (b) diffuse reflectance of solar receiver constituent materials.

As there is no measurable change in surface roughness, this reveals that surface roughness is not the reason for change in optical properties of surfaces.

Finally, the nanofluid employed in the interaction experiments has itself also been assessed. Figure 4.14 clearly shows that even after days of operation there is negligible change in the particle size distribution as well as optical characteristics.

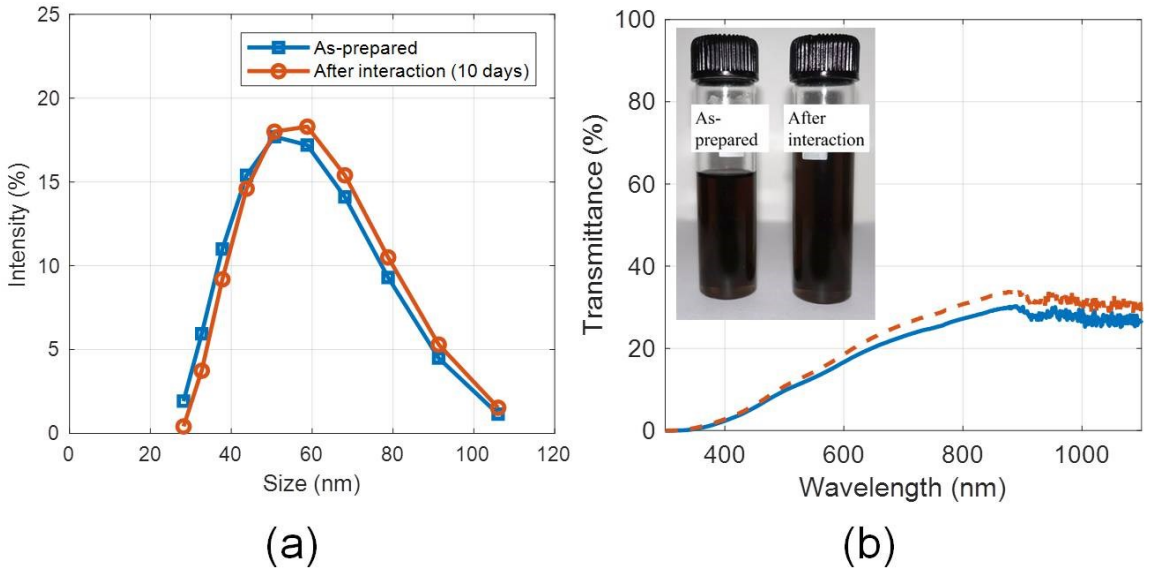

Fig. 4.14 (a) Hydrodynamic particle size distribution, and (b) spectral optical characteristics of the nanofluid employed in the interaction experiments with the solar receiver constituent materials. (Inset picture of sample f_v = 1% taken before and after interaction experiments).

Chapter 5

Experimental and theoretical estimation of thermal loss from volumetric absorption solar collector

5.1 Introduction

In relation to meeting heating and cooling energy demand (which accounts for nearly 50% of the total energy demand), solar thermal technologies potentially promise much greater dividends. Paradoxically, the current worldwide deployment of solar-thermal platforms is meager; this may be ascribed to their relatively low thermal efficiencies and high capital investments. Therefore, there is an urgent need to significantly improve the existing solar thermal systems. To this end, nanofluid based volumetrically absorbing systems have emerged as one of the potent candidates that promise high energy conversion efficiencies and lower material requirements [18,97,99,124] . Opposed to conventional surface absorption based systems (SAS); in volumetric absorption based systems (VAS), solar radiation directly interacts with the working fluid without requiring any intervening solar selective surface. Thus resulting in negligible temperature overheat and hence better photo-thermal energy conversion [62].

On-sun testing of surface and volumetric absorption based systems, wherein, the final thermal loss to the surrounding happens via free liquid surface (or 'glass' in contact with the working liquid) reveals that indeed higher conversion efficiencies can be achieved in case of the Nanofluid based VAS through careful control of the nanoparticles volume fraction and receiver height in low temperature range, 50˚C - 80˚C [189,190].

However, if the SAS is configured such that the heat loss surface is not the free liquid surface (or glass), but the solar selective surface (characteristic of state of the art surface absorption based receiver design) outperforms its volumetric absorption based counterpart [142].

This may be attributed to the higher thermal losses in case of VAS. At a given surface temperature, radiative losses ($Q_{\text{radiation}} \approx \varepsilon T^4$) are greater in case of glass (or working liquid) as compared to the solar selective surface. To address this concern, many researchers have explored the idea of coating the glass surfaces with transparent heat mirror coatings to suppress the thermal losses. These transparent heat mirror coatings allow the sunlight to pass through

and directly interact with the nanofluid and at the same time reflect back the infrared radiations emitted by the nanofluid [128,191–195]. However, majority of the reported studies are limited to either theoretical modeling [128,195] and or laboratory scale experiments on confined stagnant fluid [194]. A very few have explored the candidature of transparent heat mirrors in curbing thermal losses in fluid flow situation but with limited success [142,196].

In the present work, comprehensive experimental and theoretical modeling frameworks have been developed to understand and quantify the role played by transparent heat mirror coatings in reducing the thermal losses. In particular, a critical investigation into the side of the substrate (low iron glass) which should be coated has been dealt with. Moreover, detailed comparison of various configurations [glass-glass, glass-heat mirror (SF side coated) and glass-heat mirror (RF side coated)] in terms of the cover surface temperatures and thermal losses has been presented. Finally, fundamental performance limits of ideal transparent heat mirrors (with sharply defined distinct cut-off wavelengths) have been quantified.

5.2 EXPERIMENTAL MODELING OF THERMAL LOSSES

5.2.1 Basic concept and receiver geometries

Figure 5.1 shows various receiver geometries pertinent to volumetric absorption based solar thermal systems studied in the present work. All these systems essentially have the working fluid flowing in a conduit/tube ('receiver') with at least one optically transparent window to allow direct interaction of the incident sunlight and the working fluid. Additionally, a cover is incorporated to curb convective and radiative (thermal) losses (see Figs. 5.1(b) – 5.1(d)). Inherently, all liquids whether in pristine form or having nanoparticles dispersed in them have high absorptivity/emissivity in the infrared region due to intra-band molecular transitions. Moreover, the aforementioned optically transparent window is invariably low iron glass, and has high emissivity in IR region. Aforementioned facts point out that high radiative losses are inherent in volumetrically absorbing solar thermal systems. Therefore, to improve the performance of these systems it is imperative to curb radiative losses.

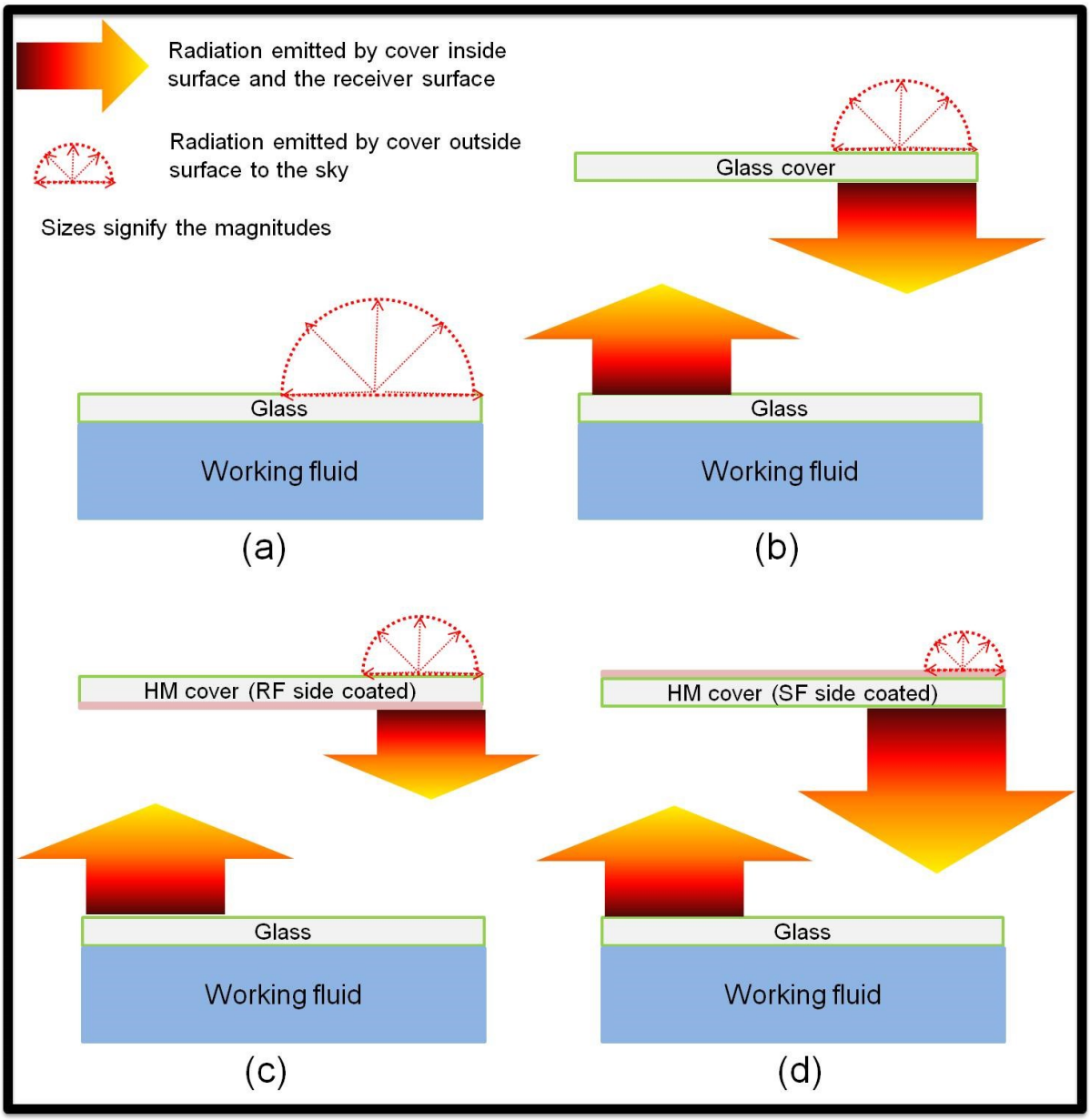

Fig. 5.1 Schematic diagrams of receiver configurations investigated in the present work.

5.2.2 Cover materials and characterization

In the present study, low iron glass has been coated with thin film of ZnO (via sputtering process at HHV- Vacuum Technology, Bangalore, India). Figures 5.2(a) and 5.2(b) show the FESEM and EDS mapping of the ZnO coated low iron glass substrate. Looking into Figs. 5.2(c) and 5.2(d), it is clear that thin ZnO film ensures high transmittance in visible-near infrared regions and at the same time high reflectance in the mid-infrared region. Hence, ZnO coated low iron glass is ideal for being employed as a cover material in volumetrically absorbing solar thermal systems. For pictorial comparison, images of low iron glass and ZnO coated low iron glass have also been provided in Fig. 5.2(e).

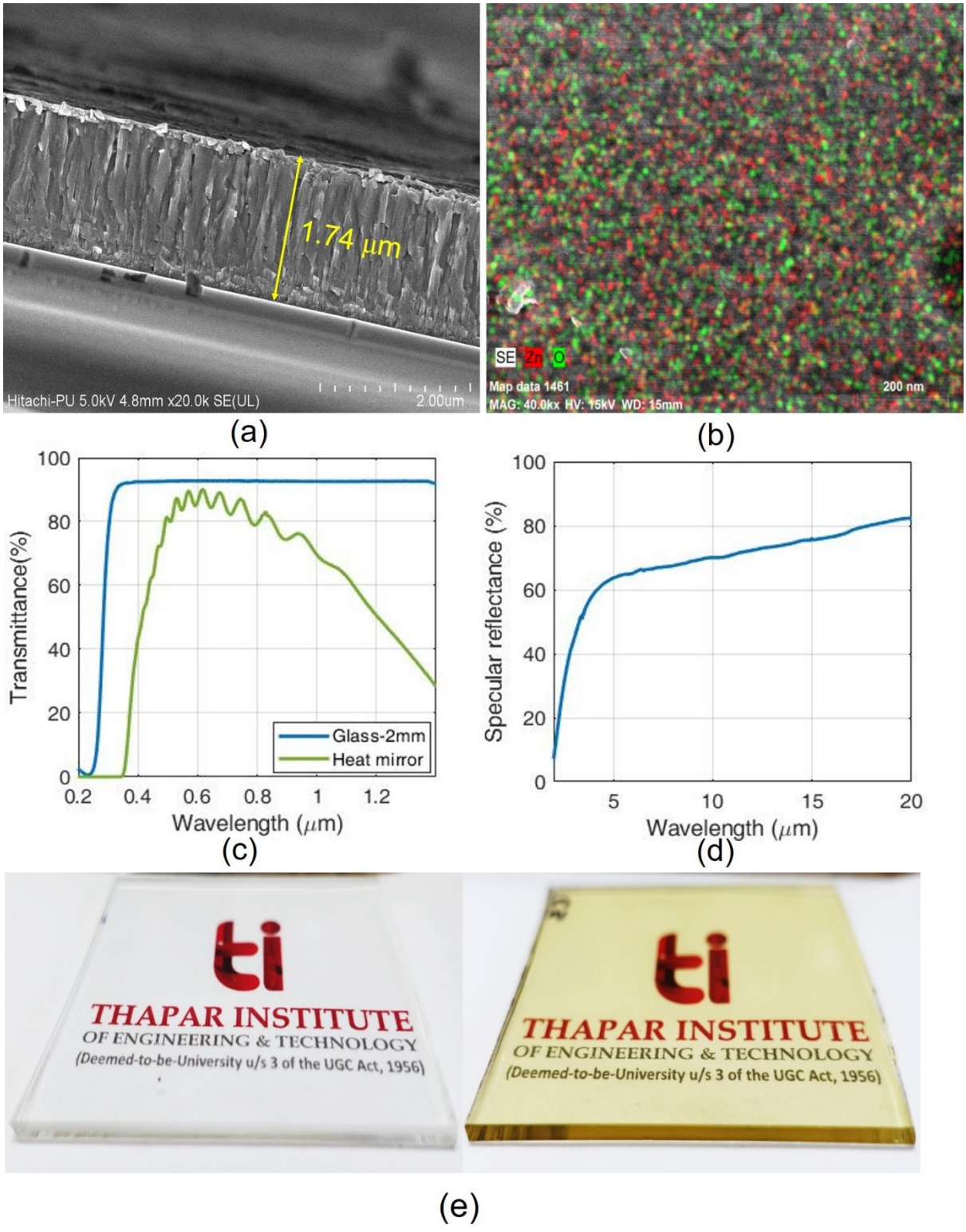

Fig. 5.2 (a) FESEM image of ZnO coating deposited on glass substrate, (b) EDS mapping of the coating, (c) spectral transmittance of the heat mirror in range (0.2 μm - 1.4 μm) (Shimadzu UV-2600), (d) specular reflectance of the coating (2 μm – 20 μm) (PerkinElmer Frontier FTIR - FIR spectrometer) and, (e) images of low-iron glass substrate (left side) and ZnO coated low-

iron glass substrate (right side) on a piece of paper with TIET logo (Copyright 2022, Thapar Institute of Engineering and Technology, Patiala, India).

5.3 Experimental setup for heat loss estimation

Figure 5.3(a) details the experimental test circuit designed for carrying out thermal loss estimation experiments. The four receiver designs described in Fig. 5.1 have been designed and fabricated. The schematics and photographs of the receiver are shown in Figs. 5.3(b) – 5.3(e). Each of the receivers is 1m in length with the optically transparent window being toughened low-iron glass (4mm). Three of the aforementioned four receiver designs have covers to curb thermal losses. The flow rate of the working fluid (paraffin oil) was maintained at 1 l/pm (1.66×10^{-5} m^3s^{-1}) using a positive displacement gear pump (Liquiflo), and it was ensured that the fluid is in direct thermal contact with the optically transparent window. Before entering the receiver, the working fluid was heated using a coil heater to the desired temperatures. As the heated fluid flows through the receiver, heat loss from the surface (facing the sky) will mimic the loss from the volumetric receiver.

K-type thermocouples are fixed in pairs on the receiver and cover surfaces to measure the real-time temperatures. Eight thermocouples were inserted in the fluid flow (four each) at the inlet and at the outlet to measure the average fluid temperature. One thermocouple is kept in shadow to measure ambient temperature. The temperature data was logged with the help of the data acquisition system (NI, cDAQ-9721, using LabVIEW platform). PID controller and variac transformer have been employed to control the heater temperature. The receiver has been housed in a box type enclosure to suppress the effect wind. Moreover, during the experiment, the box was covered to exclude the effect from external radiation. The fluid flow loop (pipes) of the experimental setup has been wrapped with high-temperature insulation silica tape having thermal conductivity (= 0.3385 $Wm^{-1}K^{-1}$, measured using guarded hot plate method).

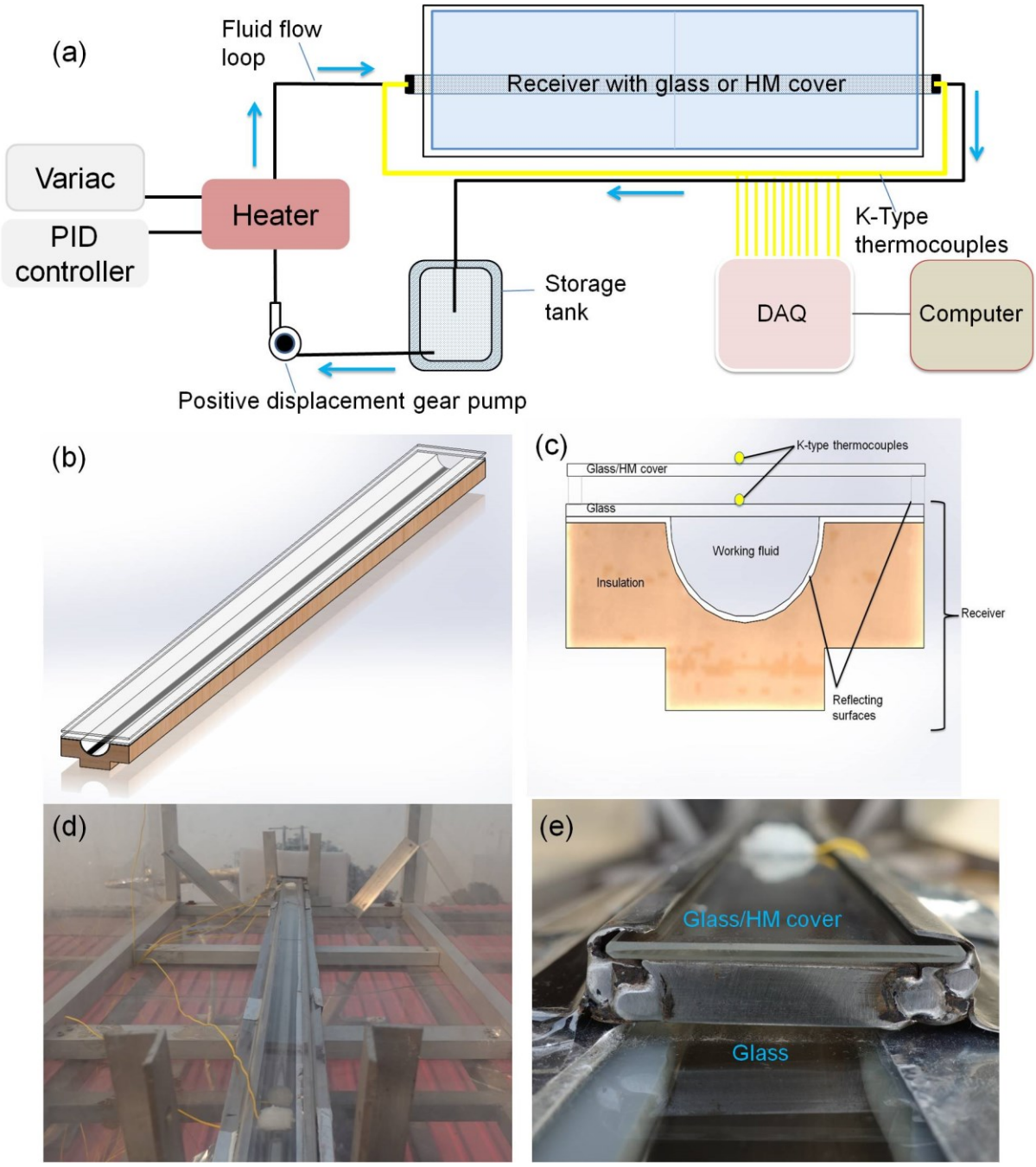

Fig. 5.3 (a) Schematic of the test circuit, (b) three dimensional view of the receiver, (c) cross-sectional view of the receiver, (d) photograph of the receiver (housed in the box type enclosure), and (e) zoomed in photograph of the receiver.

5.4 Theoretical modeling of thermal losses

5.4.1 Mathematical modeling of thermal loss mechanisms in various receiver geometries

Figures 5.4(a) and 5.4(b) detail the heat loss mechanisms and the corresponding thermal resistance networks pertinent to various receiver geometries. The receiver and the cover surface temperatures along with the emissivity values finally dictate the heat loss magnitudes in receivers without and with covers respectively. Under steady state condition (in case of receivers with cover), the heat loss from the receiver to the inner surface of the cover (Q_{loss1}), subsequently the heat transfer through the cover (Q_{loss2}) and finally the heat loss from the outside surface of the cover to the surrounding (Q_{loss3}) - all have the same magnitudes.

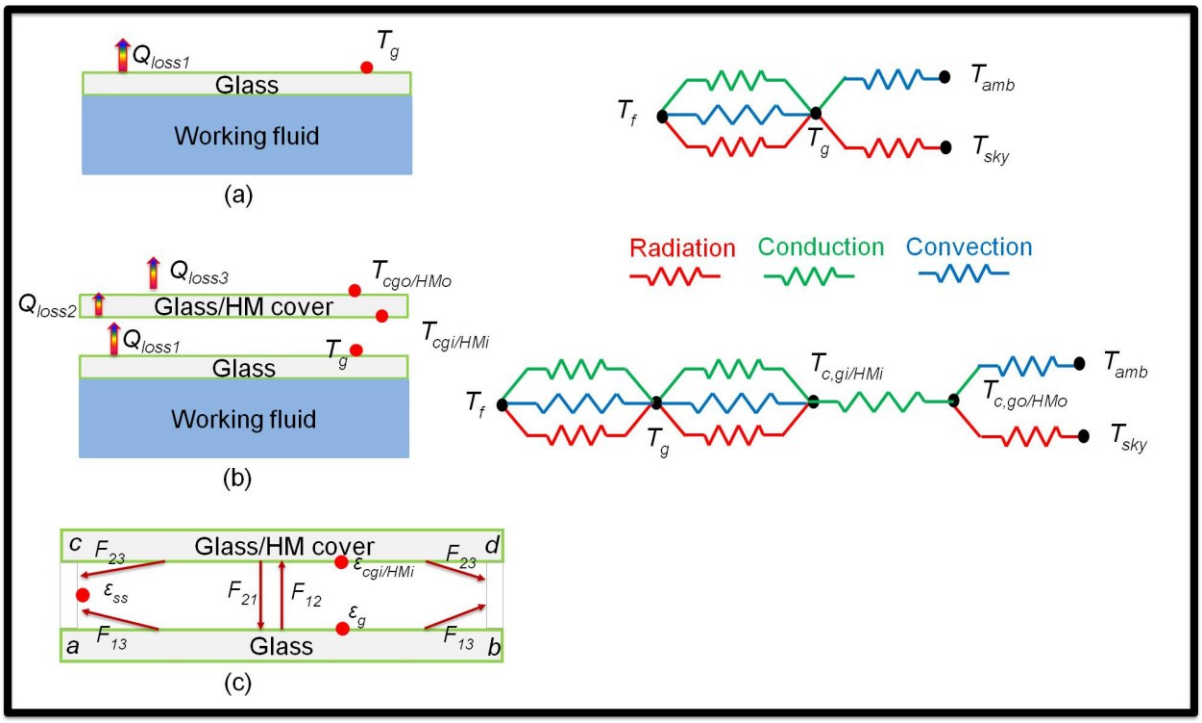

Fig. 5.4 Thermal losses (along with corresponding resistance diagrams) in volumetrically absorbing solar thermal systems: (a) without cover, (b) with cover; and (c) view factors among various surfaces. Here, "*ab*" (receiver surface) represents surface 1, "*cd*" (cover inside surface) represents surface 2 and combined "*ac*" and "*bd*" (sides of cover, stainless steel) represents surface 3.

Heat loss from the receiver surface to the inner surface of the cover happens via conduction, convection and radiation and is mathematical represented by Eq. (5.1) as

$$Q_{loss1} = \frac{kA(T_g - T_{cgi/HMi})}{l} + h_{gc}A(T_g - T_{cgi/HMi}) + \frac{\varepsilon_{cgi/HMi}}{1-\varepsilon_{cgi/HMi}}(\sigma {T_{cgi/HMi}}^4 - J_2) \quad (5.1)$$

Herein, convective heat transfer coefficient of the air (h_{gc}) between receiver and cover inner surface has been calculated from the correlation describing relationship between Nusselt number (*Nu*) and Rayleigh number (*Ra*) for parallel plates and is given by Eq. (5.2) [197] as

$$Nu = 1 + 1.44\left[1 - \frac{1708\,(\sin 1.8\beta)^{1.6}}{Ra\,\cos\beta}\right]\left[1 - \frac{1708}{Ra\,\cos\beta}\right]^{+} + \left[\left(\frac{Ra\,\cos\beta}{5830}\right)^{1/3} - 1\right]^{+} \quad (5.2)$$

'+' sign in the above equation signify that the terms in the brackets are accounted for only if positive; β (= 16°) is the inclination angle of the receiver (measured using the angle finder protractor).

The net radiative heat transfer rates between receiver surface, cover surface (glass/heat mirror), and side reflecting stainless steel surfaces (see Fig. 5.4(c)) have been computed using radiosity (*J*) and view factor relations, Eqs. (5.3) - (5.5). In order to calculate net radiative heat transfer, the surfaces have been assumed to be diffuse and grey (experiencing uniform and steady irradiation and radiosity).

$$\left(1 - F_{11} + \frac{\varepsilon_g}{1-\varepsilon_g}\right)J_1 - F_{12}J_2 - F_{13}J_3 = \frac{\varepsilon_g}{1-\varepsilon_g}\sigma {T_g}^4 \quad (5.3)$$

$$-F_{21}J_1 + \left(1 - F_{22} + \frac{\varepsilon_{cgi/HMi}}{1-\varepsilon_{cgi/HMi}}\right)J_2 - F_{23}J_3 = \frac{\varepsilon_{cgi/HMi}}{1-\varepsilon_{cgi/HMi}}\sigma {T_{cgi}}^4 \quad (5.4)$$

$$-F_{31}J_1 - F_{32}J_2 + \left(1 - F_{33} + \frac{\varepsilon_{ss}}{1-\varepsilon_{ss}}\right)J_3 = \frac{\varepsilon_{ss}}{1-\varepsilon_{ss}}\sigma {T_g}^4 \quad (5.5)$$

View factors have been evaluated using view factor algebra described as

$$\sum F_{ij} = 1 \quad (5.6)$$

$$A_i F_{ij} = A_j F_{ji} \quad (5.7)$$

Furthermore, Q_{loss2} and Q_{loss3} have been computed using Eqs. (5.8) and (5.9) respectively.

$$Q_{loss2} = \frac{k_g A(T_{cgi/HMi} - T_{cgo/HMo})}{t_g} \quad (5.8)$$

$$Q_{loss3} = \varepsilon_g A\sigma\left({T_{cgo/HMo}}^4 - {T_{atm}}^4\right) + h_{ga}A(T_{cgo/HMo} - T_{atm}) \quad (5.9)$$

where convective heat transfer coefficient (h_{ga}) from the outside cover surface to the ambient has been calculated using natural convection correlation for air and is mathematically given by Eq. (5.10) as

$$Nu = 0.68 + \frac{0.670Ra^{1/6}}{\left[1+(0.492/Pr)^{9/16}\right]^{4/9}} \qquad Ra \lesssim 10^9 \quad (5.10)$$

Properties of air in the aforementioned equations have been computed using the following equations [198]:

$$k = 0.0047 + 8 \times 10^{-5}T_{avg} - 10^{-8}{T_{avg}}^2 \quad (5.11)$$

$$\nu = 10^{-5} + 10^{-7}T_{avg} + 5 \times 10^{-11}{T_{avg}}^2 \quad (5.12)$$

$$Pr = 0.885 - 0.0008T_{avg} + 10^{-6}{T_{avg}}^2 - 5 \times 10^{-10}{T_{avg}}^3 \quad (5.13)$$

Figure 5.5 details the algorithm implemented in MATLAB and the values of various parameter/properties employed to compute the outside cover temperature values for given receiver surface temperature.

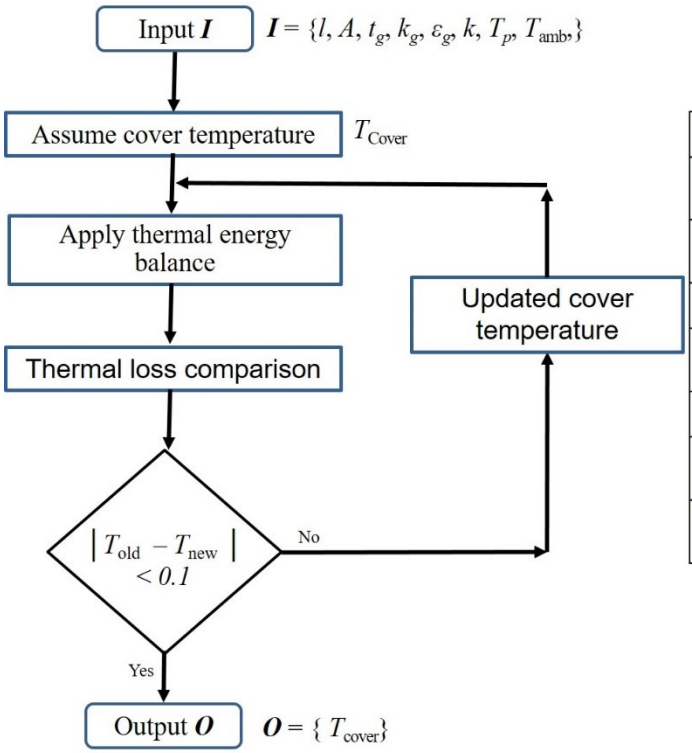

Property/parameters	Values/relation
Stefan-Boltzmann constant	$5.67*10^{-8}$ $Wm^{-2}k^{-4}$
Space between surface and cover (l)	0.009 m
Area of cover (A)	0.025 m^2
Thermal conductivity of glass (k_g)	0.8 $Wm^{-1}k^{-1}$
Thickness of glass (t_g)	0.002 m
Atmospheric temperature (T_{atm})	30°C
Emissivity of glass plate (ε_g)	0.88

Fig. 5.5 Details the algorithm implemented in MATLAB and the values of various parameter/properties employed.

5.4.2 Mathematical modeling of optical and radiative properties of heat mirror covers

As presented in Fig 5.2(d), spectral reflectance values have been experimentally measured in the NIR - MIR wavelength region (2 μm – 20 μm) using FT - IR spectrometer. However, spectral reflectivity (and hence emissivity) being a key factor in dictating the radiative losses necessitates its determination in the entire wavelength band ranging from ultra violet (UV) to far infrared (FIR) i.e., from 0.2 μm – 100 μm. To this end, Drude free carrier model and Fresnel relations have been invoked.

Optical constants, i.e., indices of refraction ($n_{h,\lambda}$) and absorption ($k_{h,\lambda}$) are prerequisites, to find out spectral reflectance values. As shown in Eqs. (5.14) and (5.15) (Drude free carrier model), optical constants are function of E_p (plasma energy), E_c (relaxation energy), and E_λ (spectral photon energies); ε_∞ being the adjustment parameter for the ZnO film [193,199]

$$n_{h,\lambda}{}^2 - k_{h,\lambda}{}^2 = \varepsilon_\infty - \frac{E_p{}^2}{E_\lambda{}^2 + E_c{}^2} \tag{5.14}$$

$$2n_{h,\lambda}k_{h,\lambda} = \frac{E_c E_p{}^2}{E_\lambda(E_\lambda{}^2 + E_c{}^2)} \tag{5.15}$$

Spectral optical constants are input parameters to Fresnel relations in evaluation of effective spectral reflectivity (Eq. (5.16) - (5.20)).

$$\rho_{\perp,\lambda} = \frac{(n_a \cos\psi - u)^2 + v^2}{(n_a \cos\psi + u)^2 + v^2} \tag{5.16}$$

$$\rho_{\parallel,\lambda} = \frac{\left[(n_{h,\lambda}{}^2 - k_{h,\lambda}{}^2)\cos\psi - n_a u\right]^2 + \left[2n_{h,\lambda}k_{h,\lambda}\cos\psi - n_a u\right]^2}{\left[(n_{h,\lambda}{}^2 - k_{h,\lambda}{}^2)\cos\psi + n_a u\right]^2 + \left[2n_{h,\lambda}k_{h,\lambda}\cos\psi + n_a u\right]^2} \tag{5.17}$$

$$\rho_{\text{eff},\lambda} = \frac{\rho_{\perp,\lambda} + \rho_{\parallel,\lambda}}{2} \tag{5.18}$$

$$2u^2 = \left(n_{h,\lambda}{}^2 - k_{h,\lambda}{}^2\right) - n_a{}^2 sin^2\psi) + \sqrt{\left(n_{h,\lambda}{}^2 - k_{h,\lambda}{}^2\right) - n_a{}^2 sin^2\psi)^2 + 4n_{h,\lambda}{}^2 k_{h,\lambda}{}^2} \tag{5.19}$$

$$2v^2 = -\left(n_{h,\lambda}{}^2 - k_{h,\lambda}{}^2\right) - n_a{}^2 \sin^2\psi)\sqrt{\left(n_{h,\lambda}{}^2 - k_{h,\lambda}{}^2\right) - n_a{}^2 \sin^2\psi)^2 + 4n_{h,\lambda}{}^2 k_{h,\lambda}{}^2} \tag{5.20}$$

Where, u and v are the real and imaginary parts of the complex variable $u + iv$, and ψ is the angle of incidence (assumed to be zero, i.e., $\psi = 0$ in the present work); $\rho_{\perp,\lambda}$, $\rho_{\parallel,\lambda}$, and $\rho_{\text{eff},\lambda}$, are spectral perpendicular, parallel and effective reflectivity values. The entire procedure to calculate the spectral reflectivity and hence spectral emissivity values is presented in the form of flowchart shown in Fig. 5.6.

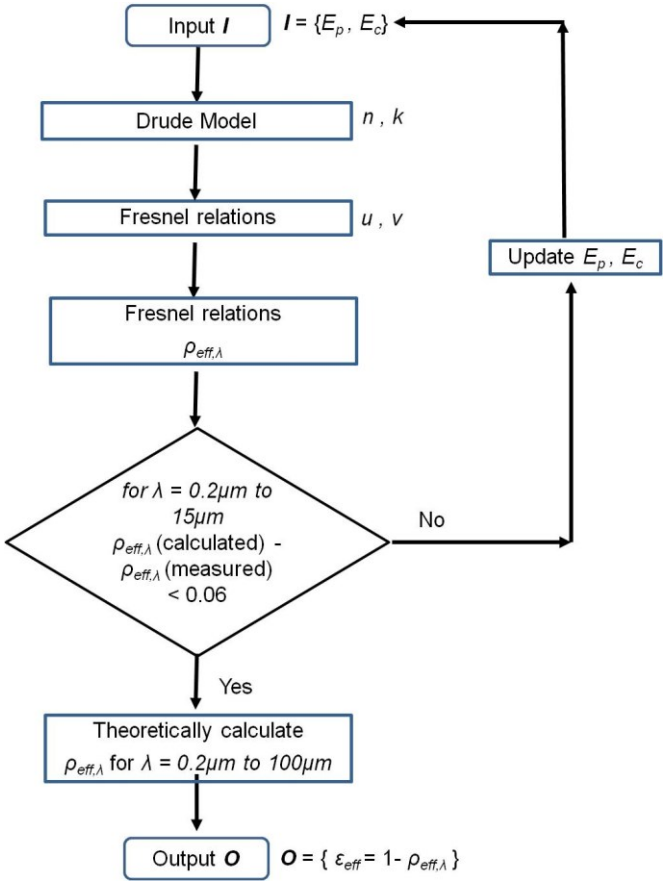

Fig. 5.6 Theoretical calculation of spectral reflectance and hence emissivity values using Drude model and Fresnel relations.

In present work, plasma energy (E_p) and relaxation energy (E_c) values have been varied and checked for best fit with respect to the experimentally measured spectral reflectance values of ZnO coating in the 2 μm to 20 μm wavelength range.

Plasma energy (E_p) value is varied between 1eV to 1.5eV, whereas relaxation energy (E_c) is varied between 0.2eV to 0.3eV [200]. As shown in Figs.5.7 (a) and 5.7(b); experimentally measured reflectance data closely follow the theoretically calculated values corresponding to E_p = 1.2eV and, E_c = 0.241eV; therefore, these have been employed to calculate the spectral values from 0.1μm to 100μm (see Fig. 5.7(c)). Figure 5.7(d) shows wavelength and emissive power weighted average effective emittance (ε_{eff}, defined in Eq. (5.21)) as a function of cover temperature. The theoretical values of E_p =1.2eV and, E_c =0.241eV have been found through iteration mechanism see Fig. 5.6. The minimum, average and maximum errors are 0.22%, 1.48% and 6% respectively. The possible reasons for the difference between the experimentally measured and theoretically calculated reflectance values may be attributed to the mismatch in

the optical constants data (index of refraction and index of absorption) for actual ZnO coating and that obtained from the literature.

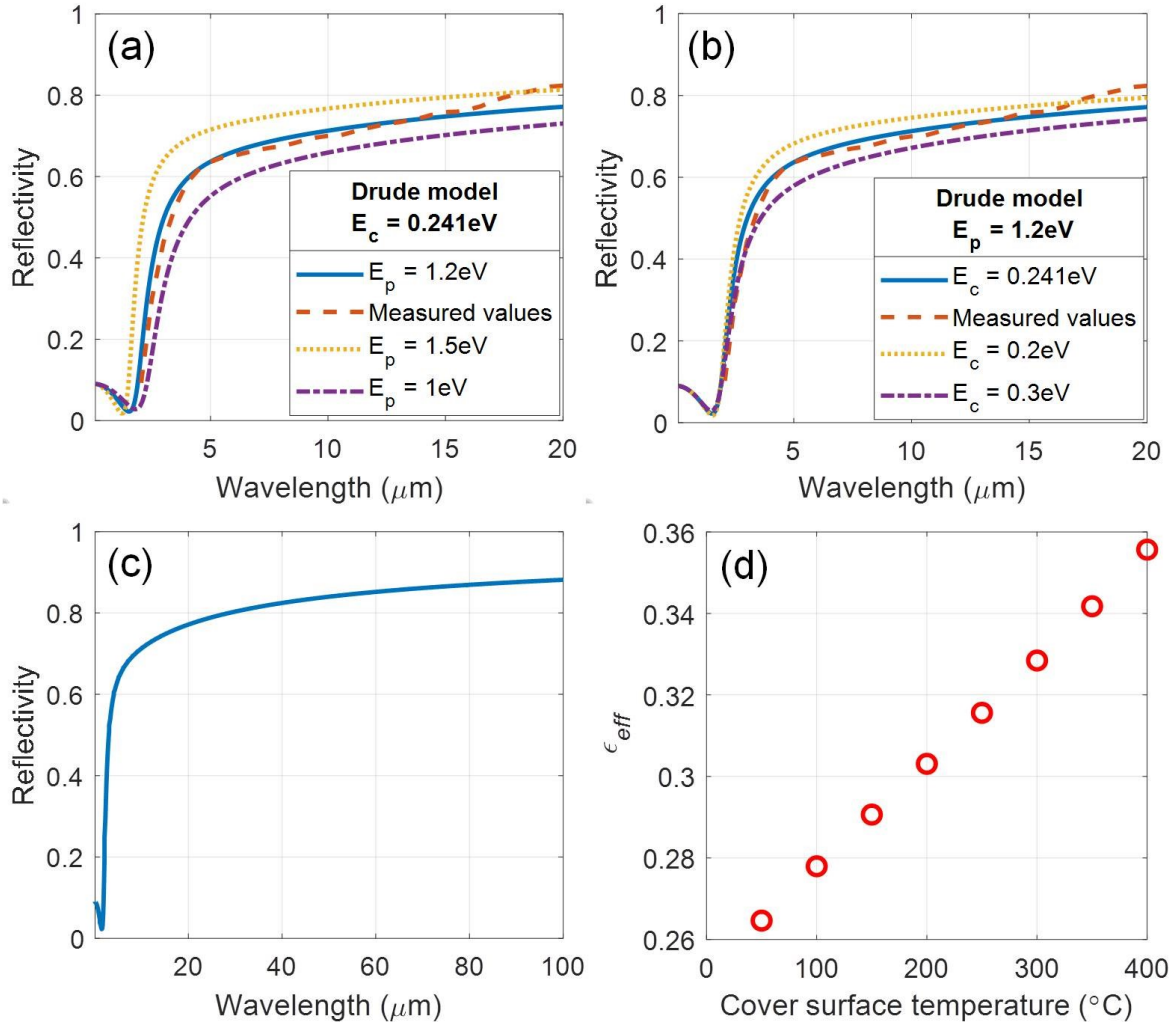

Fig. 5.7 (a) Comparison of the experimental measured spectral reflectance values with the theoretically calculated values for different value of (a) Plasmon energies (at fixed value of relaxation energy), (b) relaxation energies (at fixed value of plasmon energy), (c) theoretically calculated spectral reflectance in the 0.2 μm-100 μm wavelength band, and (d) weighted average effective emittance as a function of cover temperature.

$$\varepsilon_{eff} = \frac{\int_{0.1\mu m}^{100\mu m}(1-\rho_{\mathrm{eff},\lambda})e_{b,T,\lambda}d\lambda}{\int_{0.1\mu m}^{100\mu m} e_{b,T,\lambda}d\lambda} \tag{5.21}$$

Where, $\rho_{\mathrm{eff},\lambda}$ is the spectral effective spectral reflectivity, $e_{b,T,\lambda}$ is the spectral blackbody emissive power at a given temperature.

5.5 Experimental results

Figure 5.8(a) shows the receiver surface temperature as a function of inlet fluid temperature for various receiver configurations. Inlet fluid temperature has been varied from 100˚C to 175˚C using the heater (the maximum temperature limited by the working temperature limitation of the gear pump). Clearly, all the configurations (with or without cover) have nearly same receiver surface temperatures for relative low values of inlet fluid temperatures. The receiver surface (optically transparent window) is invariably made of low iron glass and has high absorptivity in the IR region. At low inlet fluid temperature, radiative losses from the working fluid have low values and are moreover absorbed by the receiver surface (glass surface); therefore, the type of cover employed does not alter the surface temperature appreciably, However, with the further increase in inlet fluid temperature, receiver surface temperature tends to decrease, owing to higher convective and radiative losses [See Fig. 5.8(a)]. Thus, we see more pronounced differences among the various configurations at higher temperatures.

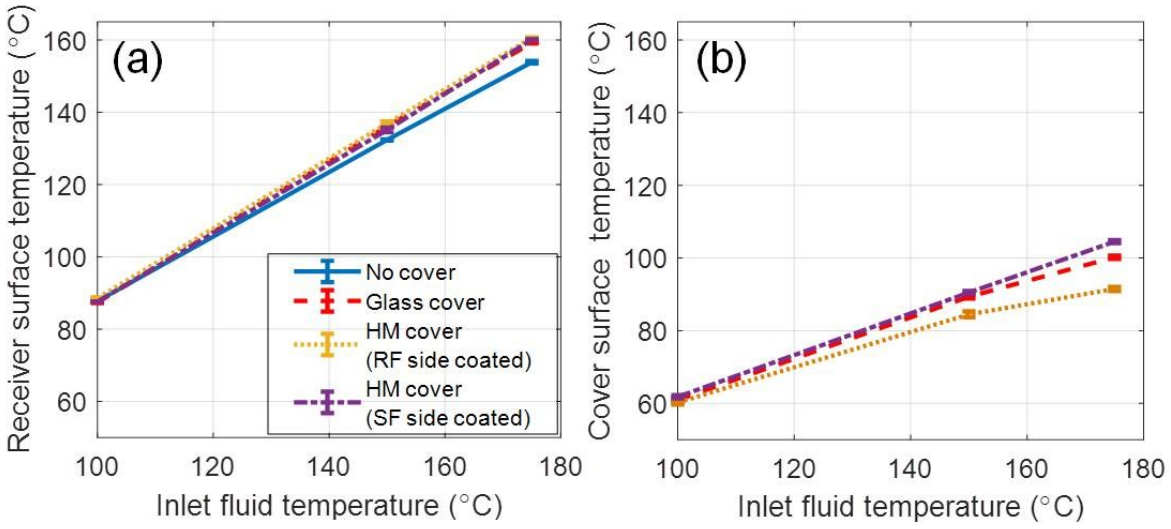

Fig. 5.8 (a) Receiver surface temperature and (b) cover surface temperature as a function of inlet fluid temperature for various receiver configurations.

However, as the inlet fluid temperature increases further, the receiver surface temperature (in case of configuration without cover) tends to have relative less surface temperature as compared to the configurations with cover. This may be ascribed to the larger thermal losses in the case of configuration without cover.

In order to better understand and compare the configurations with cover; cover surface temperature as a function of inlet fluid temperature has been plotted in Fig. 5.8 (b). In addition

to the cover temperature, the effective emissivity values dictate the magnitude of the thermal loss mechanism.

5.6 Comparing experimental and theoretical modeling results

The theoretical modeling results for various receiver design configurations have been compared with the corresponding experimentally measured values (see Fig. 5.9).

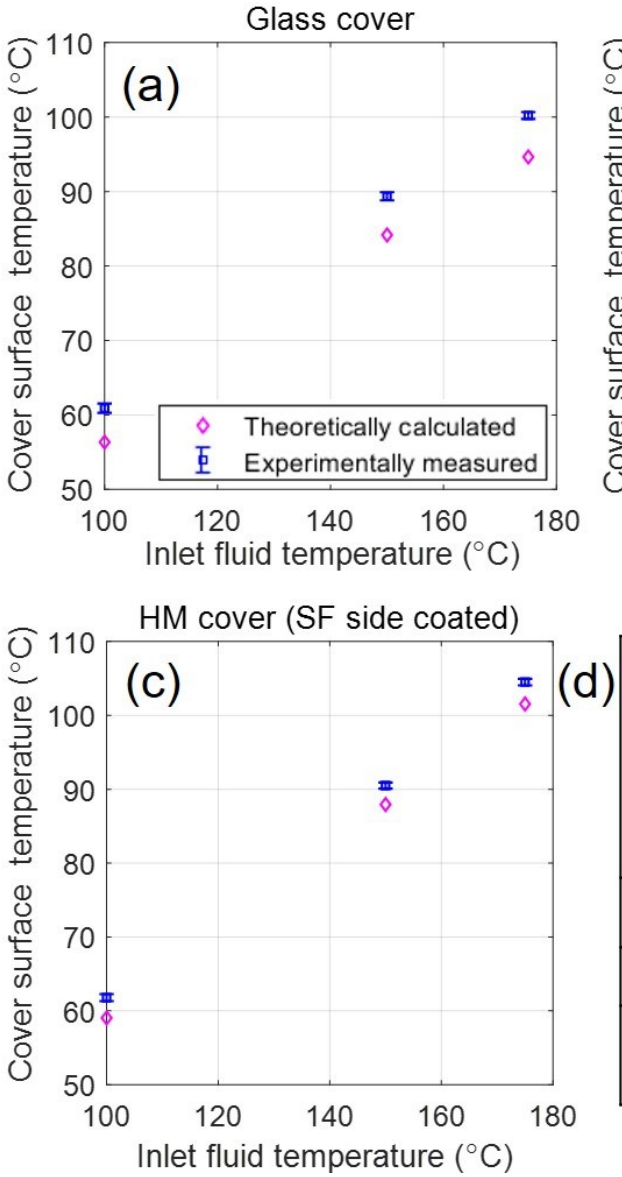

Configu-ations	Error (%) between theoretically calculated and experimentally measured values		
	100˚C	150˚C	175˚C
(a)	7.485	5.799	5.548
(b)	4.724	4.146	4.993
(c)	4.438	2.826	2.831

Fig. 5.9 Comparison of the experimental and theoretical modeling results for receiver configurations involving cover as (a) glass, (b) heat miror (RF side coated), (c) heat mirror (SF side coated), and (d) table represents the percentage error between experimental and theoretical modeling results. Error bar represents the standard deviation.

In the given temperature range (100˚C - 175˚C), the two sets closely match - hence validating the developed theoretical modeling framework. The differences in theoretically calculated and experimentally measured values have been presented in Fig. 5.9(d). The possible reasons may be the following assumptions taken in the model:

(1) Firstly, we have assumed the surface to be perfectly diffuse and grey (which may not be the case in practice.)

(2) Secondly, we have neglected the effect of coating on the thermal conductivity of the cover substrate material.

5.6.1 Assessing the efficacy of various cover configurations in reducing thermal losses in high temperature regime

As noted in Section 5.5, experimentation of various receiver configurations has been done only up to 175°C due to the working temperature limitation of the gear pump. However, to assess the performance at higher temperatures, the developed model has been invoked. In particular, effective emittance (ε_{eff}) (calculated from the Drude model) along with other design and operational parameters forms the input to the developed theoretical modeling framework.

In terms of cover surface temperatures, it is clearly apparent from Fig. 5.10(a) that highest values are observed in case of HM (SF side coated) configuration. This may be understood from the fact that SF side coating of ZnO ensures low emissivity in the IR region, but at the same time, the substrate being 'low iron glass' is highly absorbing in the IR region.

Therefore, the emitted IR radiations from the receiver surface are absorbed by the substrate of the cover (HM (SF side coated)), but owing to the ZnO coating at the SF side, there is low reemission to the surrounding - hence resulting in rise of temperature of the cover. On the other hand, lowest values of cover temperatures are observed in case of HM (RF side coated) configuration. Herein, the ZnO coating at the RF side coated predominantly reflects back the emitted IR radiation from the receiver surface - hence resulting in low cover surface temperatures. Finally, in case of 'glass' as the cover, the IR radiations emitted by the receiver surface are absorbed by the cover and at the same time in the absence of any type of ZnO coating, reemission from the top surface of the cover is high.

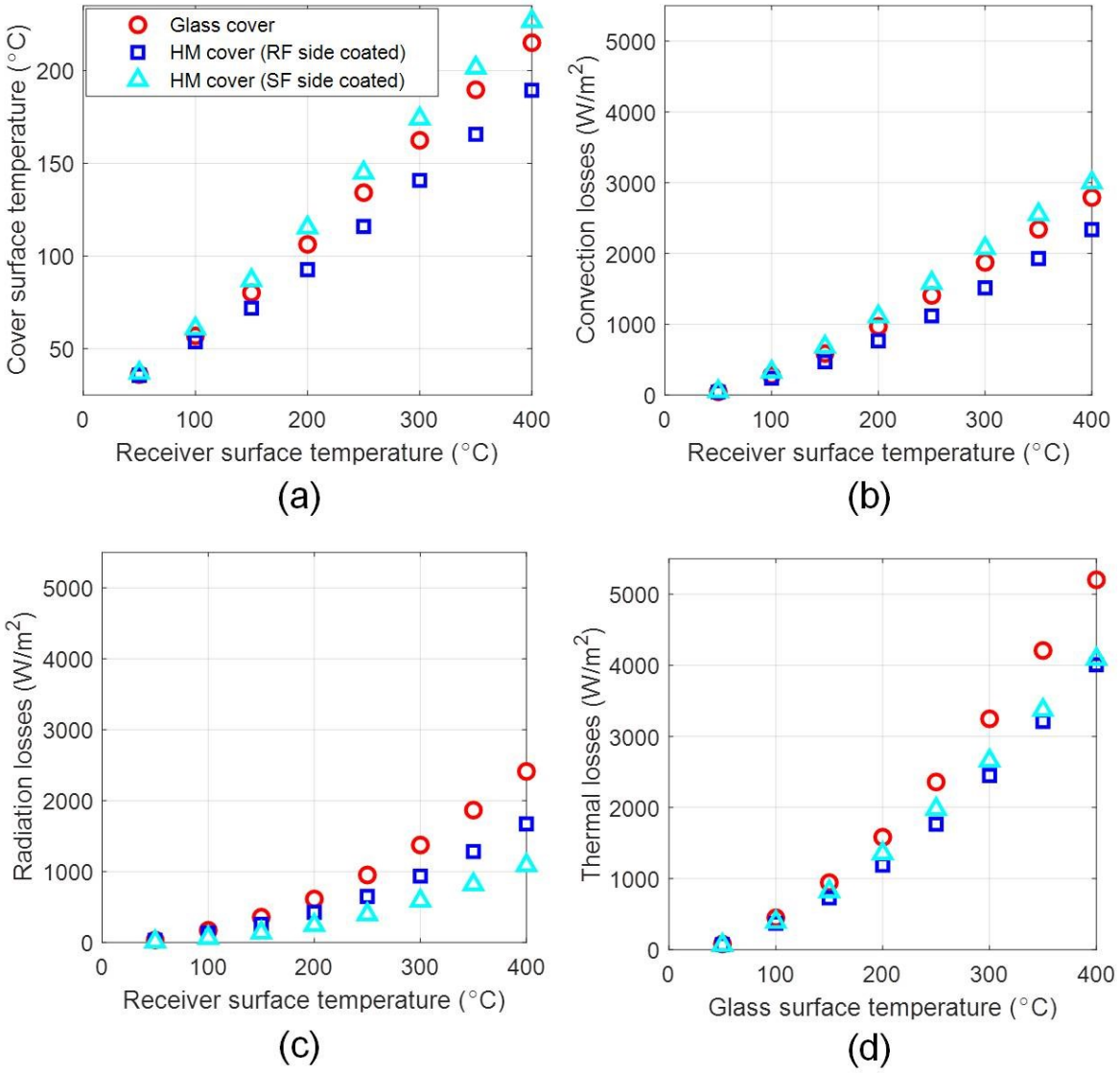

Fig. 5.10 (a) Cover surface temperature, (b) convective losses, (c) radiative losses and, (d) thermal losses as a function of receiver surface temperature for various receiver configurations.

Convective losses being directly proportional to the cover surface temperature follow similar trends to that for cover temperatures. However, in relation to radiative losses, quite different trends are observed. Radiative losses have been found to be highest in case of 'glass' as the cover and lowest in case of HM (SF side coated). Radiative losses being directly proportional to the cover surface emissivity and to the fourth power of cover surface temperatures; 'glass' cover has the highest magnitude of radiative losses. However, in case of HM (SF side coated), although temperatures are relatively high but owing to low emissivity values the overall radiative losses are the least among all the studied receiver configurations.

In order to quantify the benefits of employing ZnO based heat mirrors (relative to uncoated glass cover) as 'covers', percentage loss reduction with respect to glass cover has been computed. Figure 5.11 details the percentage reduction in thermal losses in HM covers relative to the 'glass' cover. In case of HM cover (RF side coated), the % reduction in thermal losses increases with increase in receiver surface temperature and attains a maxima (25.12% reduction) at 250˚C (glass surface temperature). Thereafter, a further increase in receiver surface temperature results in lower gains in terms of % thermal loss reduction (with respect to 'glass' cover) owing to increase in effective emissivity of the ZnO coating with increase in temperature.

In case of HM cover (SF side coated) the % thermal loss reduction first decreases (reaches minima @100˚C receiver surface temperature) and the starts increasing with further increase in receiver surface temperature. Herein, the cover temperatures being always higher than the corresponding 'glass' cover temperature - renders higher convective losses in the former case. Therefore, it is exclusively due to lower radiative losses (owing to lower values of effective emissivity) in case of HM (SF side coated) covers that results in overall thermal loss reduction with respect to 'glass' cover.

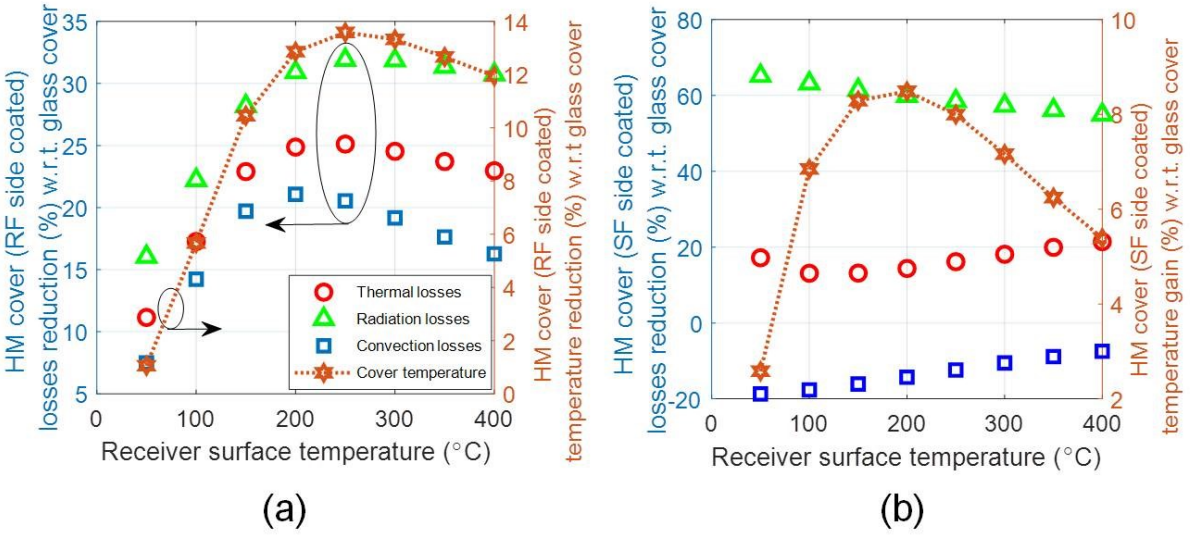

Fig. 5.11 Percentage reduction in thermal losses in (a) HM (RF side coated), and (b) HM (SF side coated) covers relative to the 'glass' cover.

5.7 Fundamental performance limits of transparent heat mirrors as cover materials

The foregoing discussion pertains to a particular type of transparent heat mirror coating (i.e. ZnO in the present case); however, to assess the performance bounds of transparent heat mirror coatings in general, ideal heat mirror coatings with sharp and distinct cut-off wavelengths have been investigated. Here, 'cut-off wavelength' refers to the wavelength which marks the boundary between two distinct regions - '100% transmittance' and '100% reflectance' before and after the cut-off wavelength respectively (see Fig. 5.12(a)).

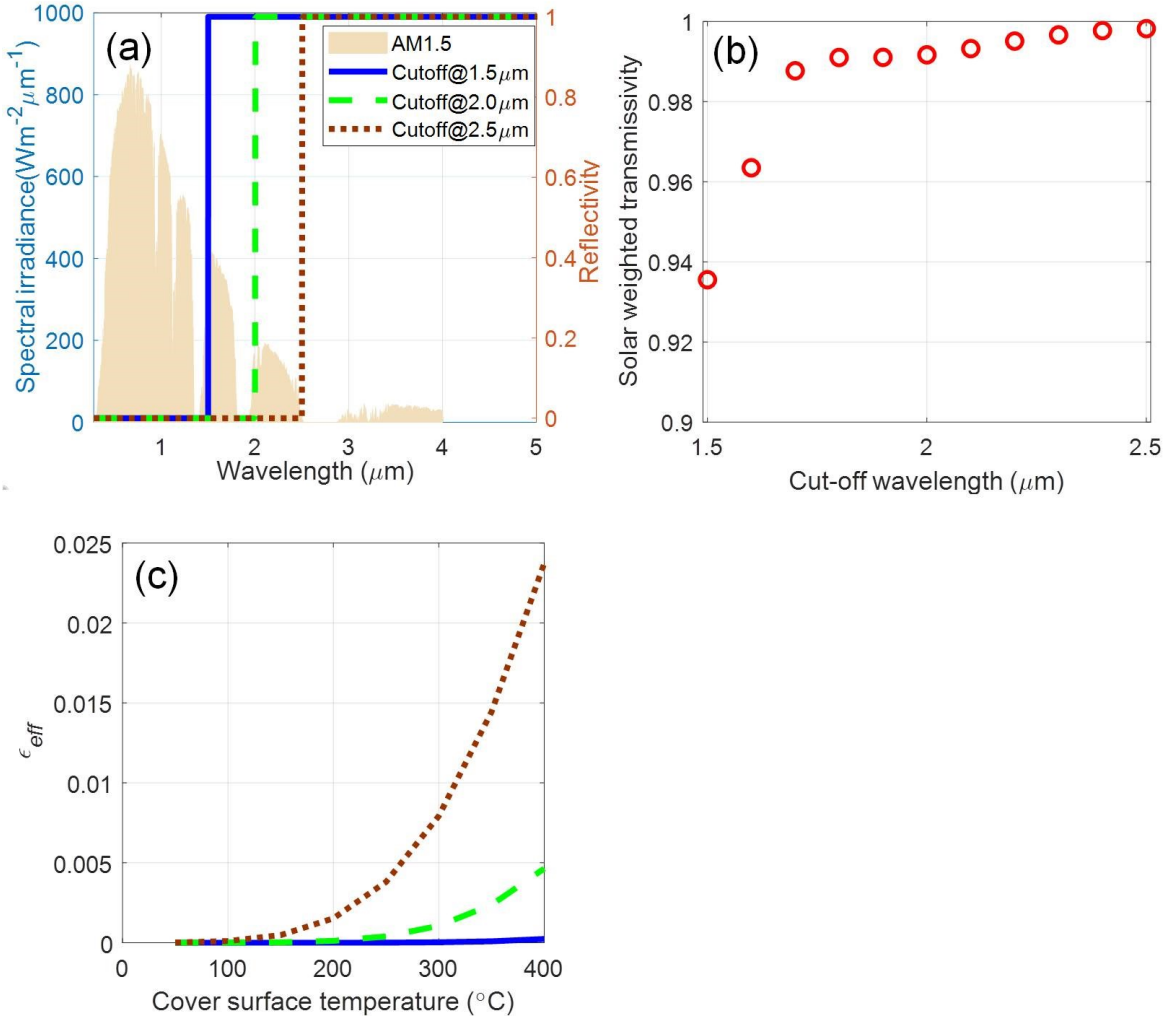

Fig. 5.12 (a) Spectral transmissivity (and reflectivity), (b) solar weighted transmissivity, and (c) effective emissivity of ideal heat mirror for various cut-off wavelength values

Ideal heat mirror has high transmittance in the solar irradiation wavelength band (quantified by solar weighted transmissivity, see Fig. 5.12(b)) and high reflectivity (i.e. low average effective emissivity, ε_{eff}, see Fig. 5.12(c)) in the infrared region. However, both the characteristics cannot

be independently engineered; therefore, a tradeoff is required to be made to tailor the heat mirror characteristics for a particular application.

Furthermore, investigation has been carried out into thermal characteristics of the ideal heat mirrors for both SF and as well RF side coating configurations. Clearly, for a given configuration, the thermal loss reduction characteristics (relative to the uncoated glass cover) are nearly independent of the cutoff wavelength (see Fig. 5.13). However, the side of the coating (whether SF side coated or RF side coated) has marked effect on the thermal losses (both convective and radiative).

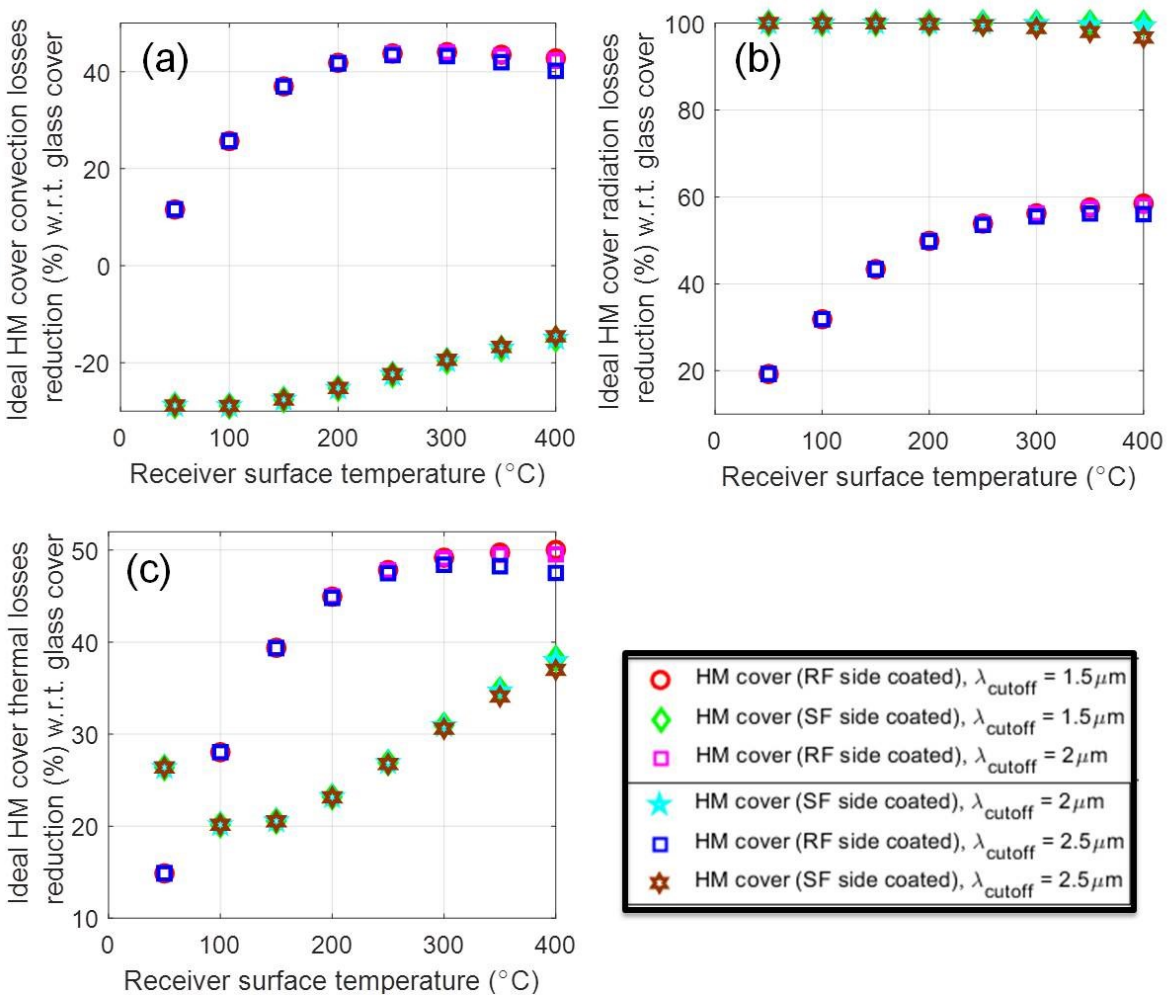

Fig. 5.13 (a) Convective losses reduction (%), (b) radiative losses reduction (%), and (c) thermal losses reduction (%)as a function of receiver surface temperature for various ideal HM covers (both RF side and SF side coated with cut-off wavelengths 1.5µm, 2.0µm, and 2.5µm) relative to glass cover.

Convective losses reduction percentage in case of HM cover (SF side coated) are higher owing to higher cover surface temperatures. On the other hand, radiative losses reduction percentage is higher in case of HM cover (RF side coated). Magnitude of convective losses being higher than the corresponding radiative losses renders HM (RF side coated) cover to have lower thermal losses.

Chapter 6

Conclusions and future work

6.1 Conclusions

Nanofluid stability and heat transfer analysis of volumetric absorption solar collector shows their potential in solar thermal systems. In this section, the conclusions of the present work are summarised.

6.1.1 Nanofluid synthesis and stability quantification

- We report a low-cost and scalable method to synthesize solar selective nanofluids from 'used engine oil.'
- The as-prepared nanofluids exhibit excellent long-term stability and photo-thermal conversion efficiency.
- Nanofluid retain their stability and functional characteristics even after extended periods of high temperature (300°C) heating, ultraviolet light exposure, and thermal cyclic loading.

6.1.2 Experimental investigation of volumetric absorption solar collector

- A nanofluid-based volumetrically absorbing solar receiver having reflecting inner surfaces has been tested under outdoor conditions.
- Steady-state thermal efficiency peaks at an optimum nanoparticles volume fraction (η_{th} = 59 ± 5.5% at f_v = 1%).
- As-prepared nanofluid does not affect the optical and surface properties of the receiver constitute materials.
- The as-prepared nanofluid shows excellent stability i.e., it retains its optical characteristics and particle size distribution even after undergoing pumping and thermal cycles and moving in flow loops (circulation through pipes/valves) during on-sun testing.

6.1.3 Experimental and theoretical estimation of thermal loss from volumetric absorption solar collector

- Various volumetric absorption based receiver configurations (glass-glass, glass-HM RF side coated and glass-HM SF side coated) have been investigated for their usefulness in thermal loss mitigation.
- Experimental results show that the use of ZnO coated cover is beneficial (relative to uncoated glass cover) in the entire temperature range studied (receiver surface temperatures: 50˚C to 400˚C).
- In low temperature range (< 100˚C), HM (SF side coated cover is better; on the other hand, in intermediate to high temperature regime (> 100˚C and up to 400˚C), HM (RF side coated) configuration proves to be more beneficial in thermal loss mitigation.
- In terms of radiation loss mitigation, HM (SF side coated) and HM (RF side coated) covers have 54.91% and 30.73% (@ 400˚C receiver surface temperature) lower values relative to uncoated glass cover.
- Coating on the RF side enables cover to have low tempertures and hence low convective losses (16.27% lower 400˚C receiver surface temperature) relative to the the uncoated glass cover.

6.2 Recommendation

Nanofluid synthesis and their stability up to 300°C shows potential for actual operating solar thermal systems. Furthermore, experimental investigation of nanofluid in a volumetric system promises a uniform temperature distribution along with the depth of the fluid. In particular, in low temperature range (< 100˚C), HM (SF side coated cover is better; on the other hand in intermediate to high temperature regime (> 100˚C and up to 400˚C), HM (RF side coated) configuration proves to be more beneficial in thermal loss mitigation. The present work provides the fundamental performance limits of transparent heat mirrors as 'covers' in volumetrically absorption based solar thermal systems. Summarised results indicate the use of volumetric absorbers for practical applications in solar thermal technologies, and more research should be done to furthers improvise the efficiency.

6.3 Suggestions for future work

- Standardization of used engine oil for more reproducible nanofluid precursor.
- Nanofluid synthesis by using different dispersants (PIBSI, PIBSA)

- More designs of the volumetric receiver to be tested on test-circuit.
- Synthesize/engineer high temperature nanofluids (300°C-700°C).
- Engineer methods to reduce the heat losses from receiver (aerogel, heat mirror etc.).

6.4 Challenges

- High-temperature testing under the leak-proof condition
- Economics of the total system as compared to a conventional system.

References

[1] Minardi, J. E., and Chuang, H. N., 1975, "Performance of a 'Black' Liquid Flat-Plate Solar Collector," Sol. Energy, **17**(3), pp. 179–183.

[2] Buongiorno, J., "A Benchmark Study on the Thermal Conductivity of Nanofluids A Benchmark Study on the Thermal Conductivity of Nanofluids," Appl. Phys. Lett., **084317**(2009).

[3] Mesgari, S., Taylor, R. A., Hjerrild, N. E., Crisostomo, F., Li, Q., and Scott, J., 2016, "An Investigation of Thermal Stability of Carbon Nanofluids for Solar Thermal Applications," Sol. Energy Mater. Sol. Cells, **157**, pp. 652–659.

[4] Otanicar, T. P., and Golden, J. S., 2009, "Comparative Environmental and Economic Analysis of Conventional and Nanofluid Solar Hot Water Technologies," Environ. Sci. Technol., **43**(15), pp. 6082–6087.

[5] Lewis, N. S., 2007, "Toward Cost-Effective Solar Energy Use," Science (80-.)., **315**(5813), pp. 798–801.

[6] Ghadimi, A., Saidur, R., and Metselaar, H. S. C., 2011, "A Review of Nanofluid Stability Properties and Characterization in Stationary Conditions," Int. J. Heat Mass Transf., **54**(17–18), pp. 4051–4068.

[7] Mesgari, S., Coulombe, S., Hordy, N., and Taylor, R. A., 2015, "Thermal Stability of Carbon Nanotube-Based Nanofluids for Solar Thermal Collectors," Mater. Res. Innov., **19**(5), pp. 650–653.

[8] Prasher, R. S., and Phelan, P. E., 2005, "Modeling of Radiative and Optical Behavior of Nanofluids Based on Multiple and Dependent Scattering Theories," Heat Transf. Part B, **2005**, pp. 739–743.

[9] Wei, X., and Wang, L., 2010, "Synthesis and Thermal Conductivity of Microfluidic Copper Nanofluids," Particuology, **8**(3), pp. 262–271.

[10] Kim, H. J., Bang, I. C., and Onoe, J., 2009, "Characteristic Stability of Bare Au-Water Nanofluids Fabricated by Pulsed Laser Ablation in Liquids," Opt. Lasers Eng., **47**(5), pp. 532–538.

[11] Hwang, Y., Lee, J. K., Lee, C. H., Jung, Y. M., Cheong, S. I., Lee, C. G., Ku, B. C., and Jang, S. P., 2007, "Stability and Thermal Conductivity Characteristics of Nanofluids," Thermochim. Acta, **455**(1–2), pp. 70–74.

[12] Sani, E., Mercatelli, L., Barison, S., Pagura, C., Agresti, F., Colla, L., and Sansoni, P., 2011, "Potential of Carbon Nanohorn-Based Suspensions for Solar Thermal Collectors," Sol. Energy Mater. Sol. Cells, **95**(11), pp. 2994–3000.

[13] Otanicar, T., Hoyt, J., Fahar, M., Jiang, X., and Taylor, R. A., 2013, "Experimental and Numerical Study on the Optical Properties and Agglomeration of Nanoparticle Suspensions," J. Nanoparticle Res., **15**(11).

[14] He, Q., Wang, S., Zeng, S., and Zheng, Z., 2013, "Experimental Investigation on Photothermal Properties of Nanofluids for Direct Absorption Solar Thermal Energy Systems," Energy Convers. Manag., **73**, pp. 150–157.

[15] Colangelo, G., Favale, E., De Risi, A., and Laforgia, D., 2013, "A New Solution for Reduced Sedimentation Flat Panel Solar Thermal Collector Using Nanofluids," Appl. Energy, **111**, pp. 80–93.

[16] Karami, M., Akhavan Bahabadi, M. A., Delfani, S., and Ghozatloo, A., 2014, "A New Application of Carbon Nanotubes Nanofluid as Working Fluid of Low-Temperature Direct Absorption Solar Collector," Sol. Energy Mater. Sol. Cells, **121**, pp. 114–118.

[17] Hordy, N., Rabilloud, D., Meunier, J. L., and Coulombe, S., 2014, "High Temperature and Long-Term Stability of Carbon Nanotube Nanofluids for Direct Absorption Solar Thermal Collectors," Sol. Energy, **105**, pp. 82–90.

[18] Khullar, V., Tyagi, H., Hordy, N., Otanicar, T. P., Hewakuruppu, Y., Modi, P., and Taylor, R. A., 2014, "Harvesting Solar Thermal Energy through Nanofluid-Based Volumetric Absorption Systems," Int. J. Heat Mass Transf., **77**, pp. 377–384.

[19] Bandarra Filho, E. P., Mendoza, O. S. H., Beicker, C. L. L., Menezes, A., and Wen, D., 2014, "Experimental Investigation of a Silver Nanoparticle-Based Direct Absorption Solar Thermal System," Energy Convers. Manag., **84**, pp. 261–267.

[20] Zhang, L., Liu, J., He, G. D., Ye, Z. C., Fang, X. M., and Zhang, Z. G., 2014, "Radiative Properties of Ionic Liquid-Based Nanofluids for Medium-to-High-Temperature Direct Absorption Solar Collectors," Sol. Energy Mater. Sol. Cells, **130**, pp. 521–528.

[21] Sajid, M. H., Said, Z., Saidur, R., Adikan, F. R. M., Sabri, M. F. M., and Rahim, N. A., 2014, "A Time Variant Investigation on Optical Properties of Water Based Al2O3nanofluid," Int. Commun. Heat Mass Transf., **50**, pp. 108–116.

[22] Mehrali, M., Sadeghinezhad, E., Latibari, S. T., Kazi, S. N., Mehrali, M., Nashrul, M., Mohd, B., Simon, H., and Metselaar, C., 2014, "Investigation of Thermal Conductivity and Rheological Properties of Nanofluids Containing Graphene Nanoplatelets," pp. 1–12.

[23] Chen, M., He, Y., Zhu, J., Shuai, Y., Jiang, B., and Huang, Y., 2015, "An Experimental Investigation on Sunlight Absorption Characteristics of Silver Nanofluids," Sol. Energy, **115**, pp. 85–94.

[24] Subramaniyan, A. L., Priya, S. L., and Ilangovan, R., 2015, "Energy Harvesting Through Optical Properties of TiO 2 and C- TiO 2 Nanofluid for Direct Absorption Solar Collectors," **5**(2).

[25] Hordy, N., Rabilloud, D., Meunier, J.-L., and Coulombe, S., 2015, "A Stable Carbon Nanotube Nanofluid for Latent Heat-Driven Volumetric Absorption Solar Heating Applications," J. Nanomater., **16**(1), p. 248.

[26] Gorji, T. B., Ranjbar, A. A., and Mirzababaei, S. N., 2015, "Optical Properties of Carboxyl Functionalized Carbon Nanotube Aqueous Nanofluids as Direct Solar Thermal Energy Absorbers," Sol. Energy, **119**, pp. 332–342.

[27] Jin, H., Lin, G., Bai, L., Amjad, M., Bandarra Filho, E. P., and Wen, D., 2016, "Photothermal Conversion Efficiency of Nanofluids: An Experimental and Numerical Study," Sol. Energy, **139**, pp. 278–289.

[28] Mesgari, S., Taylor, R. A., Hjerrild, N. E., Crisostomo, F., Li, Q., and Scott, J., 2016, "An Investigation of Thermal Stability of Carbon Nanofluids for Solar Thermal

Applications," Sol. Energy Mater. Sol. Cells, **157**, pp. 27–35.

[29] Li, X., Zou, C., Zhou, L., and Qi, A., 2016, "Experimental Study on the Thermo-Physical Properties of Diathermic Oil Based SiC Nanofluids for High Temperature Applications," Int. J. Heat Mass Transf., **97**, pp. 631–637.

[30] Menbari, A., and Alemrajabi, A. A., 2016, "Analytical Modeling and Experimental Investigation on Optical Properties of New Class of Nanofluids (Al2O3-CuO Binary Nanofluids) for Direct Absorption Solar Thermal Energy," Opt. Mater. (Amst)., **52**, pp. 116–125.

[31] Zhang, L., Chen, L., Liu, J., Fang, X., and Zhang, Z., 2016, "Effect of Morphology of Carbon Nanomaterials on Thermo-Physical Characteristics , Optical Properties and Photo-Thermal Conversion Performance of Nano Fl Uids," Renew. Energy, **99**, pp. 888–897.

[32] Shende, R. C., and Ramaprabhu, S., 2016, "Thermo-Optical Properties of Partially Unzipped Multiwalled Carbon Nanotubes Dispersed Nanofluids for Direct Absorption Solar Thermal Energy Systems," Sol. Energy Mater. Sol. Cells, **157**, pp. 117–125.

[33] Colangelo, G., Favale, E., Miglietta, P., Milanese, M., and Risi, A. De, 2016, "Thermal Conductivity , Viscosity and Stability of Al 2 O 3 -Diathermic Oil Nano Fl Uids for Solar Energy Systems," Energy, **95**, pp. 124–136.

[34] Sarsam, W. S., Amiri, A., Kazi, S. N., and Badarudin, A., 2016, "Stability and Thermophysical Properties of Non-Covalently Functionalized Graphene Nanoplatelets Nanofluids," Energy Convers. Manag., **116**, pp. 101–111.

[35] Farzaneh, H., Behzadmehr, A., Yaghoubi, M., Samimi, A., and Sarvari, S. M. H., 2016, "Stability of Nanofluids : Molecular Dynamic Approach and Experimental Study," ENERGY Convers. Manag., **111**, pp. 1–14.

[36] Chen, Y., Quan, X., Wang, Z., Lee, C., Wang, Z., Tao, P., Song, C., Wu, J., Shang, W., and Deng, T., 2016, "Stably Dispersed High-Temperature Fe 3 O 4 /Silicone-Oil Nanofluids for Direct Solar Thermal Energy Harvesting," J. Mater. Chem. A, **4**(44), pp. 17503–17511.

[37] Vakili, M., Hosseinalipour, S. M., Delfani, S., and Khosrojerdi, S., 2016, "Photothermal Properties of Graphene Nanoplatelets Nanofluid for Low-Temperature Direct Absorption Solar Collectors," Sol. Energy Mater. Sol. Cells, **152**, pp. 187–191.

[38] Li, X., Zou, C., Chen, W., and Lei, X., 2016, "Experimental Investigation of β-Cyclodextrin Modified Carbon Nanotubes Nanofluids for Solar Energy Systems: Stability, Optical Properties and Thermal Conductivity," Sol. Energy Mater. Sol. Cells, **157**, pp. 572–579.

[39] Zeng, J., Xuan, Y., and Duan, H., 2016, "Tin-Silica-Silver Composite Nanoparticles for Medium-to-High Temperature Volumetric Absorption Solar Collectors," Sol. Energy Mater. Sol. Cells, **157**, pp. 930–936.

[40] Yan, S., Wang, F., Shi, Z. G., and Tian, R., 2017, "Heat Transfer Property of SiO2/Water Nanofluid Flow inside Solar Collector Vacuum Tubes," Appl. Therm. Eng., **118**, pp. 385–391.

[41] Liu, J., Chen, L., Fang, X., and Zhang, Z., 2017, "Preparation of Graphite Nanoparticles-Modified Phase Change Microcapsules and Their Dispersed Slurry for

Direct Absorption Solar Collectors," Sol. Energy Mater. Sol. Cells, **159**, pp. 159–166.

[42] Akilu, S., Baheta, A. T., Mior, M. A., Minea, A. A., and Sharma, K. V., 2018, "Properties of Glycerol and Ethylene Glycol Mixture Based SiO2-CuO/C Hybrid Nanofluid for Enhanced Solar Energy Transport," Sol. Energy Mater. Sol. Cells, **179**(October), pp. 118–128.

[43] Mondragón, R., Torres-mendieta, R., Mínguez-vega, G., Juliá, J. E., Mondragón, R., Torres-mendieta, R., Meucci, M., Mínguez-vega, G., and Juliá, J. E., 2016, "Synthesis and Characterization of Gold / Water Nanofluids Suitable for Thermal Applications Produced by Femtosecond Laser Radiation," **6**(3).

[44] Chen, L., Xu, C., Liu, J., Fang, X., and Zhang, Z., 2017, "Optical Absorption Property and Photo-Thermal Conversion Performance of Graphene Oxide / Water Nanofluids with Excellent Dispersion Stability," Sol. Energy, **148**, pp. 17–24.

[45] Leong, K. Y., Najwa, Z. A., Ku Ahmad, K. Z., and Ong, H. C., 2017, "Investigation on Stability and Optical Properties of Titanium Dioxide and Aluminu[1] Leong KY, Najwa ZA, Ku Ahmad KZ, Ong HC. Investigation on Stability and Optical Properties of Titanium Dioxide and Aluminum Oxide Water-Based Nanofluids. Int J Thermophys," Int. J. Thermophys., **38**(5), pp. 1–15.

[46] Shende, R. C., and Ramaprabhu, S., 2017, "Application of Few-Layered Reduced Graphene Oxide Nanofluid as a Working Fluid for Direct Absorption Solar Collectors," J. Nanosci. Nanotechnol., **17**(2), pp. 1233–1239.

[47] Gimeno-Furio, A., Navarrete, N., Mondragon, R., Hernandez, L., Martinez-Cuenca, R., Cabedo, L., and Julia, J. E., 2017, "Stabilization and Characterization of a Nanofluid Based on a Eutectic Mixture of Diphenyl and Diphenyl Oxide and Carbon Nanoparticles under High Temperature Conditions," Int. J. Heat Mass Transf.

[48] Qu, J., Tian, M., Han, X., Zhang, R., and Wang, Q., 2017, "Photo-Thermal Conversion Characteristics of MWCNT-H 2 O Nanofluids for Direct Solar Thermal Energy Absorption Applications," Appl. Therm. Eng., **124**, pp. 486–493.

[49] Torres-Mendieta, R., Mondragón, R., Puerto-Belda, V., Mendoza-Yero, O., Lancis, J., Juliá, J. E., and Mínguez-Vega, G., 2017, "Characterization of Tin/Ethylene Glycol Solar Nanofluids Synthesized by Femtosecond Laser Radiation," ChemPhysChem, **18**(9), pp. 1055–1060.

[50] Gómez-Villarejo, R., Navas, J., Mart\'\in, E. I., Sánchez-Coronilla, A., Aguilar, T., Gallardo, J. J., los Santos, D., Alcántara, R., Fernández-Lorenzo, C., and Mart\'\in-Calleja, J., 2017, "Preparation of Au Nanoparticles in a Non-Polar Medium: Obtaining High-Efficiency Nanofluids for Concentrating Solar Power. An Experimental and Theoretical Perspective," J. Mater. Chem. A, **5**(24), pp. 12483–12497.

[51] khosrojerdi, S., Lavasani, A. M., and Vakili, M., 2017, "Experimental Study of Photothermal Specifications and Stability of Graphene Oxide Nanoplatelets Nanofluid as Working Fluid for Low-Temperature Direct Absorption Solar Collectors (DASCs)," Sol. Energy Mater. Sol. Cells, **164**(February), pp. 32–39.

[52] Liu, J., Xu, C., Chen, L. L., Fang, X., and Zhang, Z., 2017, "Preparation and Photo-Thermal Conversion Performance of Modified Graphene/Ionic Liquid Nanofluids with Excellent Dispersion Stability," Sol. Energy Mater. Sol. Cells, **170**(May), pp. 219–232.

[53] Chen, W., Zou, C., and Li, X., 2017, "Solar Energy Materials & Solar Cells An Investigation into the Thermophysical and Optical Properties of SiC / Ionic Liquid Nano Fl Uid for Direct Absorption Solar Collector," Sol. Energy Mater. Sol. Cells, **163**(December 2016), pp. 157–163.

[54] Bhalla, V., and Tyagi, H., 2017, "Solar Energy Harvesting by Cobalt Oxide Nanoparticles, a Nanofluid Absorption Based System," Sustain. Energy Technol. Assessments, **24**, pp. 45–54.

[55] Chen, L., Liu, J., Fang, X., and Zhang, Z., 2017, "Solar Energy Materials & Solar Cells Reduced Graphene Oxide Dispersed Nano Fl Uids with Improved Photo-Thermal Conversion Performance for Direct Absorption Solar Collectors," Sol. Energy Mater. Sol. Cells, **163**(December 2016), pp. 125–133.

[56] Wang, R. T., and Wang, J. C., 2017, "Intelligent Dimensional and Thermal Performance Analysis of Al2O3nanofluid," Energy Convers. Manag., **138**, pp. 686–697.

[57] Wang, H., Yang, W., Cheng, L., Guan, C., and Yan, H., 2018, "Solar Energy Materials and Solar Cells Chinese Ink : High Performance Nano Fl Uids for Solar Energy," **176**(November 2017), pp. 374–380.

[58] Zeng, J., and Xuan, Y., 2018, "Enhanced Solar Thermal Conversion and Thermal Conduction of MWCNT- SiO 2 / Ag Binary Nano Fl Uids," **212**(November 2017), pp. 809–819.

[59] Yasinskiy, A., Navas, J., Aguilar, T., Alcántara, R., Gallardo, J. J., Sánchez-Coronilla, A., Martín, E. I., De Los Santos, D., and Fernández-Lorenzo, C., 2018, "Dramatically Enhanced Thermal Properties for TiO2-Based Nanofluids for Being Used as Heat Transfer Fluids in Concentrating Solar Power Plants," Renew. Energy, **119**, pp. 809–819.

[60] Gulzar, O., Qayoum, A., and Gupta, R., 2018, "Photo - Thermal Characteristics of Hybrid Nanofluids Based on Therminol - 55 Oil for Concentrating Solar Collectors," Appl. Nanosci., (0123456789).

[61] Wang, X., He, Y., Chen, M., and Hu, Y., 2018, "ZnO-Au Composite Hierarchical Particles Dispersed Oil-Based Nanofluids for Direct Absorption Solar Collectors," Sol. Energy Mater. Sol. Cells, **179**(November 2017), pp. 185–193.

[62] Khullar, V., Bhalla, V., and Tyagi, H., 2017, "Potential Heat Transfer Fluids (Nanofluids) for Direct Volumetric Absorption-Based Solar Thermal Systems," J. Therm. Sci. Eng. Appl., **10**(1), p. 011009.

[63] Zhang, R., and Qu, J., 2018, "Efficiency Improvement of a Solar Direct Volumetric Receiver Utilizing Aqueous Suspensions of CuO," (September 2017), pp. 1–9.

[64] Mehrali, M., Ghatkesar, M. K., and Pecnik, R., 2018, "Full-Spectrum Volumetric Solar Thermal Conversion via Graphene/Silver Hybrid Plasmonic Nanofluids," Appl. Energy, **224**(February), pp. 103–115.

[65] Sánchez-Coronilla, A., Martín, E. I., Navas, J., Aguilar, T., Gómez-Villarejo, R., Alcántara, R., Piñero, J. C., and Fernández-Lorenzo, C., 2018, "Experimental and Theoretical Analysis of NiO Nanofluids in Presence of Surfactants," J. Mol. Liq., **252**, pp. 211–217.

[66] Navas, J., Martínez-Merino, P., Sánchez-Coronilla, A., Gallardo, J. J., Alcántara, R., Martín, E. I., Piñero, J. C., León, J. R., Aguilar, T., Toledo, J. H., and Fernández-Lorenzo, C., 2018, "MoS2 Nanosheets vs. Nanowires: Preparation and a Theoretical Study of Highly Stable and Efficient Nanofluids for Concentrating Solar Power," J. Mater. Chem. A, **6**(30), pp. 14919–14929.

[67] Lingling, W., Guihua, Z., Wei, Y., Jia, Z., Xiaoxiao, Y., Qiang, L., and Huaqing, X., 2018, "Integrating Nitrogen-Doped Graphitic Carbon with Au Nanoparticles for Excellent Solar Energy Absorption Properties," Sol. Energy Mater. Sol. Cells, **184**(October 2017), pp. 1–8.

[68] Tao, P., Shu, L., Zhang, J., Lee, C., Ye, Q., Guo, H., and Deng, T., 2018, "Progress in Natural Science : Materials International Silicone Oil-Based Solar-Thermal Fluids Dispersed with PDMS-Modified," Prog. Nat. Sci. Mater. Int., (May), pp. 1–9.

[69] Taylor, R. A., Hjerrild, N., Duhaini, N., Pickford, M., and Mesgari, S., 2018, "Stability Testing of Silver Nanodisc Suspensions for Solar Applications," Appl. Surf. Sci., **455**, pp. 465–475.

[70] Aguilar, T., Carrillo-berdugo, I., Roberto, G., Jes, J., Fern, C., and Navas, J., 2018, "A Solvothermal Synthesis of TiO 2 Nanoparticles in a Non-Polar Medium to Prepare Highly Stable Nanofluids with Improved Thermal Properties."

[71] Huaxu, L., Fuqiang, W., Dong, L., Jie, Z., and Jianyu, T., 2019, "Optical Properties and Transmittances of ZnO-Containing Nanofluids in Spectral Splitting Photovoltaic/Thermal Systems," Int. J. Heat Mass Transf., **128**, pp. 668–678.

[72] Qu, J., Zhang, R., Wang, Z., and Wang, Q., 2019, "Photo-Thermal Conversion Properties of Hybrid CuO-MWCNT/H2O Nanofluids for Direct Solar Thermal Energy Harvest," Appl. Therm. Eng., **147**, pp. 390–398.

[73] Xu, X., Xu, C., Liu, J., Fang, X., and Zhang, Z., 2019, "A Direct Absorption Solar Collector Based on a Water-Ethylene Glycol Based Nanofluid with Anti-Freeze Property and Excellent Dispersion Stability," Renew. Energy, **133**, pp. 760–769.

[74] Sadeghi, G., Safarzadeh, H., and Ameri, M., 2019, "Experimental and Numerical Investigations on Performance of Evacuated Tube Solar Collectors with Parabolic Concentrator, Applying Synthesized Cu2O/Distilled Water Nanofluid," Energy Sustain. Dev., **48**, pp. 88–106.

[75] Shu, L., Zhang, J., Fu, B., Xu, J., Tao, P., Song, C., Shang, W., Wu, J., and Deng, T., 2019, "Ethylene Glycol-Based Solar-Thermal Fluids Dispersed with Reduced Graphene Oxide," RSC Adv., **9**(18), pp. 10282–10288.

[76] Gimeno-Furio, A., Hernandez, L., Navarrete, N., and Mondragon, R., 2019, "Characterisation Study of a Thermal Oil-Based Carbon Black Solar Nanofluid," Renew. Energy, **140**, pp. 493–500.

[77] Gimeno-Furio, A., Hernandez, L., Barison, S., Agresti, F., Cabaleiro, D., and Mancin, S., 2019, "Optical Characterisation of Oxidised Carbon Nanohorn Nanofluids for Direct Solar Energy Absorption Applications," Sol. Energy, **191**(September), pp. 323–331.

[78] Sharaf, O. Z., Rizk, N., Joshi, C. P., Abi Jaoudé, M., Al-Khateeb, A. N., Kyritsis, D. C., Abu-Nada, E., and Martin, M. N., 2019, "Ultrastable Plasmonic Nanofluids in

Optimized Direct Absorption Solar Collectors," Energy Convers. Manag., **199**(September), p. 112010.

[79] Sreekumar, S., Joseph, A., Sujith Kumar, C. S., and Thomas, S., 2020, "Investigation on Influence of Antimony Tin Oxide/Silver Nanofluid on Direct Absorption Parabolic Solar Collector," J. Clean. Prod., **249**, p. 119378.

[80] Valizade, M., Heyhat, M. M., and Maerefat, M., 2019, "Experimental Comparison of Optical Properties of Nanofluid and Metal Foam for Using in Direct Absorption Solar Collectors," Sol. Energy Mater. Sol. Cells, **195**(September 2018), pp. 71–80.

[81] Chen, W., Zou, C., and Li, X., 2019, "Application of Large-Scale Prepared MWCNTs Nanofluids in Solar Energy System as Volumetric Solar Absorber," Sol. Energy Mater. Sol. Cells, **200**(8), p. 109931.

[82] Li, X., Zeng, G., and Lei, X., 2020, "The Stability, Optical Properties and Solar-Thermal Conversion Performance of SiC-MWCNTs Hybrid Nanofluids for the Direct Absorption Solar Collector (DASC) Application," Sol. Energy Mater. Sol. Cells, **206**(1), p. 110323.

[83] Alberghini, M., Morciano, M., Bergamasco, L., Fasano, M., Lavagna, L., Humbert, G., Sani, E., Pavese, M., Chiavazzo, E., and Asinari, P., 2019, "Coffee-Based Colloids for Direct Solar Absorption," Sci. Rep., **9**(1), pp. 1–11.

[84] Almanassra, I. W., Manasrah, A. D., Al-Mubaiyedh, U. A., Al-Ansari, T., Malaibari, Z. O., and Atieh, M. A., 2020, "An Experimental Study on Stability and Thermal Conductivity of Water/CNTs Nanofluids Using Different Surfactants: A Comparison Study," J. Mol. Liq., **304**, p. 111025.

[85] Okonkwo, E. C., Essien, E. A., Kavaz, D., Abid, M., and Ratlamwala, T. A. H., 2019, "Olive Leaf-Synthesized Nanofluids for Solar Parabolic Trough Collector—Thermal Performance Evaluation," J. Therm. Sci. Eng. Appl., **11**(4), pp. 1–13.

[86] Hazra, S. K., Ghosh, S., and Nandi, T. K., 2019, "Photo-Thermal Conversion Characteristics of Carbon Black-Ethylene Glycol Nanofluids for Applications in Direct Absorption Solar Collectors," Appl. Therm. Eng., **163**(September), p. 114402.

[87] Lin, J., Ju, X., Xu, C., Yang, Y., and Du, X., 2020, "High Temperature Stability and Optical Properties Investigation of a Novel ITO-Therminol 66 Nanofluid for Spectral Splitting PV/T Systems," Opt. Mater. (Amst)., **109**(August), p. 110373.

[88] Qu, J., Zhang, R., Shang, L., and Wang, Z., 2020, "Graphene Oxide/Multi-Walled Carbon Nanotube—Therminol®66 Hybrid Nanofluids for Low-to-Medium Temperature Volumetric Solar Collectors," Int. J. Energy Res., **44**(9), pp. 7216–7228.

[89] Lee, R., Kim, J. B., Qin, C., Lee, H., Lee, B. J., and Jung, G. Y., 2020, "Synthesis of Therminol-Based Plasmonic Nanofluids with Core/Shell Nanoparticles and Characterization of Their Absorption/Scattering Coefficients," Sol. Energy Mater. Sol. Cells, **209**(February), p. 110442.

[90] Martínez-Merino, P., Sani, E., Mercatelli, L., Alcántara, R., and Navas, J., 2020, "WSe2 Nanosheets Synthesized by a Solvothermal Process as Advanced Nanofluids for Thermal Solar Energy," ACS Sustain. Chem. Eng., **8**(3), pp. 1627–1636.

[91] Li, X., Chen, W., and Zou, C., 2020, "An Experimental Study on β-Cyclodextrin Modified Carbon Nanotubes Nanofluids for the Direct Absorption Solar Collector

(DASC): Specific Heat Capacity and Photo-Thermal Conversion Performance," Sol. Energy Mater. Sol. Cells, **204**(1), p. 110240.

[92] Sani, E., Vallejo, J. P., Mercatelli, L., Martina, M. R., di Rosa, D., Dell'Oro, A., and Lugo, L., 2020, "A Comprehensive Physical Profile for Aqueous Dispersions of Carbon Derivatives as Solar Working Fluids," Appl. Sci., **10**(2).

[93] Torres, E., Carrillo-Berdugo, I., Zorrilla, D., Sánchez-Márquez, J., and Navas, J., 2021, "CuO-Containing Oil-Based Nanofluids for Concentrating Solar Power: An Experimental and Computational Integrated Insight," J. Mol. Liq., **325**, p. 114643.

[94] Sharaf, O. Z., Rizk, N., Munro, C. J., Joshi, C. P., Anjum, D. H., Abu-Nada, E., Martin, M. N., and Alazzam, A., 2021, "Radiation Stability and Photothermal Performance of Surface-Functionalized Plasmonic Nanofluids for Direct-Absorption Solar Applications," Sol. Energy Mater. Sol. Cells, **227**(March).

[95] Seifikar, F., and Azizian, S., 2021, "Super-Stable Carbon Quantum Dots Nanofluid for Efficient Solar-Thermal Conversion," Energy Convers. Manag., **228**(September 2020).

[96] Zanetti, E., Dugaria, S., Biscaglia, F., Agresti, F., Fedele, L., Meneghetti, M., and Del Col, D., 2021, "Investigation of Nanofluids Circulating in a Volumetric Solar Receiver," J. Therm. Sci. Eng. Appl., **13**(4), pp. 1–12.

[97] Tyagi, H., Phelan, P., and Prasher, R., 2009, "Predicted Efficiency of a Low-Temperature Nanofluid-Based Direct Absorption Solar Collector," J. Sol. Energy Eng., **131**(4), p. 041004.

[98] Mu, L., Zhu, Q., and Si, L., 2009, "Radiative Properties of Nanofluids and Performance of a Direct Solar Absorber Using Nanofluids," ASME 2009 Second Int. Conf. Micro/Nanoscale Heat Mass Transf. Vol. 1, pp. 549–553.

[99] Otanicar, T. P., Phelan, P. E., Prasher, R. S., Rosengarten, G., and Taylor, R. A., 2010, "Nanofluid-Based Direct Absorption Solar Collector," J. Renew. Sustain. Energy, **2**(3).

[100] Lee, B. J., Park, K., Walsh, T., and Xu, L., 2012, "Radiative Heat Transfer Analysis in Plasmonic Nanofluids for Direct Solar Thermal Absorption," J. Sol. Energy Eng., **134**(2), p. 021009.

[101] Parvin, S., Nasrin, R., and Alim, M. A., 2014, "Heat Transfer and Entropy Generation through Nanofluid Filled Direct Absorption Solar Collector," Int. J. Heat Mass Transf., **71**, pp. 386–395.

[102] Cregan, V., and Myers, T. G., 2015, "Modelling the Efficiency of a Nanofluid Direct Absorption Solar Collector," Int. J. Heat Mass Transf., **90**(July 2017), pp. 505–514.

[103] Gorji, T. B., and Ranjbar, A. A., 2015, "Geometry Optimization of a Nanofluid-Based Direct Absorption Solar Collector Using Response Surface Methodology," Sol. Energy, **122**, pp. 314–325.

[104] Lee, S.-H., and Jang, S. P., 2015, "Efficiency of a Volumetric Receiver Using Aqueous Suspensions of Multi-Walled Carbon Nanotubes for Absorbing Solar Thermal Energy," Int. J. Heat Mass Transf., **80**, pp. 58–71.

[105] Gupta, H. K., Agrawal, G. Das, and Mathur, J., 2015, "Investigations for Effect of Al2O3–H2O Nanofluid Flow Rate on the Efficiency of Direct Absorption Solar

Collector," Case Stud. Therm. Eng., **5**, pp. 70–78.

[106] Karami, M., Akhavan-Bahabadi, M. A., Delfani, S., and Raisee, M., 2015, "Experimental Investigation of CuO Nanofluid-Based Direct Absorption Solar Collector for Residential Applications," Renew. Sustain. Energy Rev., **52**, pp. 793–801.

[107] Delfani, S., Karami, M., and Akhavan-Behabadi, M. A., 2016, "Performance Characteristics of a Residential-Type Direct Absorption Solar Collector Using MWCNT Nanofluid," Renew. Energy, **87**, pp. 754–764.

[108] Vakili, M., Hosseinalipour, S. M., Delfani, S., Khosrojerdi, S., and Karami, M., 2016, "Experimental Investigation of Graphene Nanoplatelets Nanofluid-Based Volumetric Solar Collector for Domestic Hot Water Systems," Sol. Energy, **131**, pp. 119–130.

[109] Jeon, J., Park, S., and Lee, B. J., 2016, "Analysis on the Performance of a Flat-Plate Volumetric Solar Collector Using Blended Plasmonic Nanofluid," Sol. Energy, **132**, pp. 247–256.

[110] Turkyilmazoglu, M., 2016, "Performance of Direct Absorption Solar Collector with Nanofluid Mixture," Energy Convers. Manag., **114**, pp. 1–10.

[111] Gorji, T. B., and Ranjbar, A. A., 2016, "A Numerical and Experimental Investigation on the Performance of a Low-Flux Direct Absorption Solar Collector (DASC) Using Graphite, Magnetite and Silver Nanofluids," Sol. Energy, **135**, pp. 493–505.

[112] Menbari, A., Alemrajabi, A. A., and Rezaei, A., 2016, "Heat Transfer Analysis and the Effect of CuO/Water Nanofluid on Direct Absorption Concentrating Solar Collector," Appl. Therm. Eng., **104**, pp. 176–183.

[113] Chen, M., He, Y., Zhu, J., and Wen, D., 2016, "Investigating the Collector Efficiency of Silver Nanofluids Based Direct Absorption Solar Collectors," Appl. Energy, **181**, pp. 65–74.

[114] Chen, M., He, Y., Zhu, J., and Kim, D. R., 2016, "Enhancement of Photo-Thermal Conversion Using Gold Nanofluids with Different Particle Sizes," Energy Convers. Manag., **112**, pp. 21–30.

[115] Chen, L., Xu, C., Liu, J., Fang, X., and Zhang, Z., 2017, "Optical Absorption Property and Photo-Thermal Conversion Performance of Graphene Oxide/Water Nanofluids with Excellent Dispersion Stability," Sol. Energy, **148**, pp. 17–24.

[116] Dugaria, S., Bortolato, M., and Del Col, D., 2017, "Modelling of a Direct Absorption Solar Receiver Using Carbon Based Nanofluids under Concentrated Solar Radiation," Renew. Energy.

[117] Khullar, V., Bhalla, V., and Tyagi, H., 2018, "Potential Heat Transfer Fluids (Nanofluids) for Direct Volumetric Absorption-Based Solar Thermal Systems," J. Therm. Sci. Eng. Appl., **10**(1), p. 11009.

[118] Bhalla, V., Khullar, V., and Tyagi, H., 2018, "Experimental Investigation of Photo-Thermal Analysis of Blended Nanoparticles (Al2O3/Co3O4) for Direct Absorption Solar Thermal Collector," Renew. Energy, **123**, pp. 616–626.

[119] Zeiny, A., Jin, H., Bai, L., Lin, G., and Wen, D., 2018, "A Comparative Study of Direct Absorption Nano Fl Uids for Solar Thermal Applications," Sol. Energy,

161(February 2017), pp. 74–82.

[120] Beicker, C. L. L., Amjad, M., Bandarra Filho, E. P., and Wen, D., 2018, "Experimental Study of Photothermal Conversion Using Gold/Water and MWCNT/Water Nanofluids," Sol. Energy Mater. Sol. Cells, **188**(May), pp. 51–65.

[121] He, Y., Chen, M., Wang, X., and Hu, Y., 2018, "Plasmonic Multi-Thorny Gold Nanostructures for Enhanced Solar Thermal Conversion," Sol. Energy, **171**(June), pp. 73–82.

[122] Campos, C., Vasco, D., Angulo, C., Burdiles, P. A., Cardemil, J., and Palza, H., 2019, "About the Relevance of Particle Shape and Graphene Oxide on the Behavior of Direct Absorption Solar Collectors Using Metal Based Nanofluids under Different Radiation Intensities," Energy Convers. Manag., **181**(December 2018), pp. 247–257.

[123] Taylor, R. A., Phelan, P. E., Otanicar, T. P., Walker, C. A., Nguyen, M., Trimble, S., and Prasher, R., 2011, "Applicability of Nanofluids in High Flux Solar Collectors," J. Renew. Sustain. Energy, **3**(2).

[124] Lenert, A., and Wang, E. N., 2012, "Optimization of Nanofluid Volumetric Receivers for Solar Thermal Energy Conversion," Sol. Energy, **86**(1), pp. 253–265.

[125] Veeraragavan, A., Lenert, A., Yilbas, B., Al-Dini, S., and Wang, E. N., 2012, "Analytical Model for the Design of Volumetric Solar Flow Receivers," Int. J. Heat Mass Transf., **55**(4), pp. 556–564.

[126] Khullar, V., Tyagi, H., Phelan, P. E., Otanicar, T. P., Singh, H., and Taylor, R. A., 2013, "Solar Energy Harvesting Using Nanofluids-Based Concentrating Solar Collector," J. Nanotechnol. Eng. Med., **3**(3), p. 031003.

[127] Luo, Z., Wang, C., Wei, W., Xiao, G., and Ni, M., 2014, "Performance Improvement of a Nanofluid Solar Collector Based on Direct Absorption Collection (DAC) Concepts," Int. J. Heat Mass Transf., **75**, pp. 262–271.

[128] Hewakuruppu, Y. L., Taylor, R. A., Tyagi, H., Khullar, V., Otanicar, T., Coulombe, S., and Hordy, N., 2015, "Limits of Selectivity of Direct Volumetric Solar Absorption," Sol. Energy, **114**, pp. 206–216.

[129] Liu, J., Ye, Z., Zhang, L., Fang, X., and Zhang, Z., 2015, "A Combined Numerical and Experimental Study on Graphene/Ionic Liquid Nanofluid Based Direct Absorption Solar Collector," Sol. Energy Mater. Sol. Cells, **136**, pp. 177–186.

[130] Moradi, A., Sani, E., Simonetti, M., Francini, F., Chiavazzo, E., and Asinari, P., 2015, "Carbon-Nanohorn Based Nanofluids for a Direct Absorption Solar Collector for Civil Application," J. Nanosci. Nanotechnol., **15**(5), pp. 3488–3495.

[131] Xu, G., Chen, W., Deng, S., Zhang, X., and Zhao, S., 2015, "Performance Evaluation of a Nanofluid-Based Direct Absorption Solar Collector with Parabolic Trough Concentrator," Nanomaterials, **5**(4), pp. 2131–2147.

[132] Kasaeian, A., Daneshazarian, R., Rezaei, R., Pourfayaz, F., and Kasaeian, G., 2017, "Experimental Investigation on the Thermal Behavior of Nanofluid Direct Absorption in a Trough Collector," J. Clean. Prod., **158**, pp. 276–284.

[133] Menbari, A., Alemrajabi, A. A., and Rezaei, A., 2017, "Experimental Investigation of Thermal Performance for Direct Absorption Solar Parabolic Trough Collector

(DASPTC) Based on Binary Nanofluids," Exp. Therm. Fluid Sci., **80**, pp. 218–227.

[134] Potenza, M., Milanese, M., Colangelo, G., and de Risi, A., 2017, "Experimental Investigation of Transparent Parabolic Trough Collector Based on Gas-Phase Nanofluid," Appl. Energy, **203**, pp. 560–570.

[135] Bortolato, M., Dugaria, S., Agresti, F., Barison, S., Fedele, L., Sani, E., and Del Col, D., 2017, "Investigation of a Single Wall Carbon Nanohorn-Based Nanofluid in a Full-Scale Direct Absorption Parabolic Trough Solar Collector," Energy Convers. Manag., **150**(May), pp. 693–703.

[136] Cregan, V., and Myers, T. G., 2015, "Modelling the Efficiency of a Nanofluid Direct Absorption Solar Collector," Int. J. Heat Mass Transf., **90**, pp. 505–514.

[137] Heyhat, M. M., Valizade, M., Abdolahzade, S., and Maerefat, M., 2020, "Thermal Efficiency Enhancement of Direct Absorption Parabolic Trough Solar Collector (DAPTSC) by Using Nanofluid and Metal Foam," Energy, **192**.

[138] Joseph, A., Sreekumar, S., and Thomas, S., 2020, "Energy and Exergy Analysis of SiO2/Ag-CuO Plasmonic Nanofluid on Direct Absorption Parabolic Solar Collector," Renew. Energy, **162**, pp. 1655–1664.

[139] Vijayaraghavan, S., Ganapathisubbu, S., and Santosh Kumar, C., 2013, "Performance Analysis of a Spectrally Selective Concentrating Direct Absorption Collector," Sol. Energy, **97**, pp. 418–425.

[140] Kaluri, R., Vijayaraghavan, S., and Ganapathisubbu, S., 2015, "Model Development and Performance Studies of a Concentrating Direct Absorption Solar Collector," J. Sol. Energy Eng., **137**(84), pp. 021005-1–12.

[141] Muraleedharan, M., Singh, H., Suresh, S., and Udayakumar, M., 2016, "Directly Absorbing Therminol-Al2O3 Nano Heat Transfer Fluid for Linear Solar Concentrating Collectors," Sol. Energy, **137**, pp. 134–142.

[142] Li, Q., Zheng, C., Mesgari, S., Hewkuruppu, Y. L., Hjerrild, N., Crisostomo, F., Rosengarten, G., Scott, J. A., and Taylor, R. A., 2016, "Experimental and Numerical Investigation of Volumetric versus Surface Solar Absorbers for a Concentrated Solar Thermal Collector," Sol. Energy, **136**, pp. 349–364.

[143] Kalidoss, P., Venkatachalapathy, S., and Suresh, S., 2020, "Optical and Thermal Properties of Therminol 55-TiO2 Nanofluids for Solar Energy Storage," Int. J. Photoenergy, **2020**.

[144] Jin, H., Lin, G., Guo, Y., Bai, L., and Wen, D., 2020, "Nanoparticles Enabled Pump-Free Direct Absorption Solar Collectors," Renew. Energy, **145**, pp. 2337–2344.

[145] Shen, C., Lv, G., Wei, S., Zhang, C., and Ruan, C., 2020, "Investigating the Performance of a Novel Solar Lighting/Heating System Using Spectrum-Sensitive Nanofluids," Appl. Energy, **270**(May), p. 115208.

[146] Otanicar, T. P., Phelan, P. E., Prasher, R. S., Rosengarten, G., and Taylor, R. A., 2010, "Nanofluid-Based Direct Absorption Solar Collector," J. Renew. Sustain. Energy, **2**(3), p. 33102.

[147] Milanese, M., Colangelo, G., Cretì, A., Lomascolo, M., Iacobazzi, F., and De Risi, A., 2016, "Optical Absorption Measurements of Oxide Nanoparticles for Application as

Nanofluid in Direct Absorption Solar Power Systems - Part I: Water-Based Nanofluids Behavior," Sol. Energy Mater. Sol. Cells, **147**, pp. 315–320.

[148] Mondragón, R., Torres-Mendieta, R., Meucci, M., Mínguez-Vega, G., Enrique Juliá, J., and Sani, E., 2016, "Synthesis and Characterization of Gold/Water Nanofluids Suitable for Thermal Applications Produced by Femtosecond Laser Radiation," J. Photonics Energy, **6**(3), p. 034001.

[149] Qu, J., Tian, M., Han, X., Zhang, R., and Wang, Q., 2017, "Photo-Thermal Conversion Characteristics of MWCNT-H2O Nanofluids for Direct Solar Thermal Energy Absorption Applications," Appl. Therm. Eng., **124**, pp. 486–493.

[150] Wang, H., Yang, W., Cheng, L., Guan, C., and Yan, H., 2018, "Chinese Ink: High Performance Nanofluids for Solar Energy," Sol. Energy Mater. Sol. Cells, **176**, pp. 374–380.

[151] Zhang, K., Cao, Q., Jin, L., Li, P., and Zhang, X., 2017, "A Novel Route to Utilize Waste Engine Oil by Blending It with Water and Coal," J. Hazard. Mater., **332**, pp. 51–58.

[152] Rizvi, S. Q. A., 2003, *9 - Additives and Additive Chemistry*, Fuels and Lubricants Handbook.

[153] Won, Y., Meeker, S. P., Trappe, V., Weitz, D. A., Diggs, N. Z., and Emert, J. I., 2005, "Effect of Temperature on Carbon-Black Agglomeration in Hydrocarbon Liquid with Adsorbed Dispersant," (3), pp. 924–932.

[154] Esangbedo, C., Boehman, A. L., and Perez, J. M., 2012, "Characteristics of Diesel Engine Soot That Lead to Excessive Oil Thickening," Tribol. Int., **47**, pp. 194–203.

[155] La Rocca, A., Di Liberto, G., Shayler, P. J., Parmenter, C. D. J., and Fay, M. W., 2013, "The Nanostructure of Soot-in-Oil Particles and Agglomerates from an Automotive Diesel Engine," Tribol. Int., **61**, pp. 80–87.

[156] Bagi, S., Sharma, V., and Aswath, P. B., 2018, "Role of Dispersant on Soot-Induced Wear in Cummins ISB Engine Test," Carbon N. Y., **136**, pp. 395–408.

[157] dos Reis, M. A., and Jerónimo, M. S., 1988, "Waste Lubricating Oil Rerefining by Extraction-Flocculation. 1. A Scientific Basis to Design Efficient Solvents," Ind. Eng. Chem. Res., **27**(7), pp. 1222–1228.

[158] dos Reis, M. A., and Jeronimo, M. S., 1990, "Waste Lubricating Oil Rerefining by Extraction-Flocculation. 2. A Method to Formulate Efficient Composite Solvents," Ind. Eng. Chem. Res., **29**(3), pp. 432–436.

[159] Martins, J. P., 1997, "The Extraction - Flocculation Re-Refining Lubricating Oil Process Using Ternary Organic Solvents," Ind. Eng. Chem. Res., **36**(9), pp. 3854–3858.

[160] Morgan, L. J., 1985, *Polymeric Stabilization of Colloidal Dispersions*, Academic Press.

[161] Hordy, N., Coulombe, S., and Meunier, J. L., 2013, "Plasma Functionalization of Carbon Nanotubes for the Synthesis of Stable Aqueous Nanofluids and Poly(Vinyl Alcohol) Nanocomposites," Plasma Process. Polym., **10**(2), pp. 110–118.

[162] Lerche, D., 2002, “Dispersion Stability and Particle Characterization by Sedimentation Kinetics in a Centrifugal Field,” J. Dispers. Sci. Technol., **23**(5), pp. 699–709.

[163] Krause, B., Petzold, G., Pegel, S., and Pötschke, P., 2009, “Correlation of Carbon Nanotube Dispersability in Aqueous Surfactant Solutions and Polymers,” Carbon N. Y., **47**(3), pp. 602–612.

[164] Lamas, B., Abreu, B., Fonseca, A., Martins, N., and Oliveira, M., 2012, “Assessing Colloidal Stability of Long Term MWCNT Based Nanofluids,” J. Colloid Interface Sci., **381**(1), pp. 17–23.

[165] Harel, Y., Azoubel, S., Magdassi, S., and Lellouche, J.-P., 2013, “A Dispersability Study on Poly (Thiophen-3-Yl-Acetic Acid) and PEDOT Multi-Walled Carbon Nanotube Composites Using an Analytical Centrifuge,” J. Colloid Interface Sci., **390**(1), pp. 62–69.

[166] Yang, P., Zhao, X., Liu, Y., and Lai, X., 2016, “Preparation and Tribological Properties of Dual-Coated CuO Nanoparticles as Water Based Lubricant Additives,” J. Nanosci. Nanotechnol., **16**(9), pp. 9683–9689.

[167] Fang, Y. K., Osama, M., Rashmi, W., Shahbaz, K., Khalid, M., Mjalli, F. S., and Farid, M. M., 2016, “Synthesis and Thermo-Physical Properties of Deep Eutectic Solvent-Based Graphene Nanofluids,” Nanotechnology, **27**(7), p. 75702.

[168] Ahmad, I., Ullah, J., Ishaq, M., Khan, H., Gul, K., Siddiqui, S., and Ahmad, W., 2015, “Monitoring of Oxidation Behavior in Mineral Base Oil Additized with Biomass Derived Antioxidants Using FT-IR Spectroscopy,” RSC Adv., **5**(122), pp. 101089–101100.

[169] Iacobazzi, F., Milanese, M., Colangelo, G., Lomascolo, M., and de Risi, A., 2016, “An Explanation of the Al2O3 Nanofluid Thermal Conductivity Based on the Phonon Theory of Liquid,” Energy, **116**, pp. 786–794.

[170] Milanese, M., Iacobazzi, F., Colangelo, G., and de Risi, A., 2016, “An Investigation of Layering Phenomenon at the Liquid–Solid Interface in Cu and CuO Based Nanofluids,” Int. J. Heat Mass Transf., **103**, pp. 564–571.

[171] Hernaiz, M., Alonso, V., Estellé, P., Wu, Z., Sundén, B., Doretti, L., Mancin, S., Çobanoğlu, N., Karadeniz, Z. H., Garmendia, N., Lasheras-Zubiate, M., Hernández López, L., Mondragón, R., Martínez-Cuenca, R., Barison, S., Kujawska, A., Turgut, A., Amigo, A., Huminic, G., Huminic, A., Kalus, M. R., Schroth, K. G., and Buschmann, M. H., 2019, “The Contact Angle of Nanofluids as Thermophysical Property,” J. Colloid Interface Sci., **547**, pp. 393–406.

[172] Ham, J., Kim, H., Shin, Y., and Cho, H., 2017, “Experimental Investigation of Pool Boiling Characteristics in Al2O3 Nanofluid According to Surface Roughness and Concentration,” Int. J. Therm. Sci., **114**, pp. 86–97.

[173] Sadeghinezhad, E., Mehrali, M., Tahan Latibari, S., Mehrali, M., Kazi, S. N., Oon, C. S., and Metselaar, H. S. C., 2014, “Experimental Investigation of Convective Heat Transfer Using Graphene Nanoplatelet Based Nanofluids under Turbulent Flow Conditions,” Ind. Eng. Chem. Res.

[174] Xing, M., Yu, J., and Wang, R., 2016, “International Journal of Heat and Mass Transfer Effects of Surface Modification on the Pool Boiling Heat Transfer of

MWNTs / Water Nanofluids," Int. J. Heat Mass Transf., **103**, pp. 914–919.

[175] Chaudhury, K., Ghosh, U., and Chakraborty, S., 2013, "International Journal of Heat and Mass Transfer Substrate Wettability Induced Alterations in Convective Heat Transfer Characteristics in Microchannel Flows : An Order Parameter Approach," HEAT MASS Transf., **67**, pp. 1083–1095.

[176] Vafaei, S., Wen, D., and Borca-Tasciuc, T., 2011, "Nanofluid Surface Wettability through Asymptotic Contact Angle," Langmuir, **27**(6), pp. 2211–2218.

[177] Harikrishnan, A. R., Dhar, P., Agnihotri, P. K., Gedupudi, S., and Das, S. K., 2017, "Wettability of Complex Fluids and Surfactant Capped Nanoparticle-Induced Quasi-Universal Wetting Behavior," J. Phys. Chem. B, **121**(24), pp. 6081–6095.

[178] Lee, S. H., Choi, T. J., and Jang, S. P., 2016, "Thermal Efficiency Comparison: Surface-Based Solar Receivers with Conventional Fluids and Volumetric Solar Receivers with Nanofluids," Energy, **115**, pp. 404–417.

[179] 1985, *Method of Testing to Determine the Thermal Performance of Solar Collectors. (ASHRAE Standard). United States: N. p., 1985. Web*.

[180] Kasaeian, A., Daviran, S., Azarian, R. D., and Rashidi, A., 2015, "Performance Evaluation and Nanofluid Using Capability Study of a Solar Parabolic Trough Collector," Energy Convers. Manag., **89**, pp. 368–375.

[181] Yousefi, T., Shojaeizadeh, E., Veysi, F., and Zinadini, S., 2012, "An Experimental Investigation on the Effect of PH Variation of MWCNT-H 2O Nanofluid on the Efficiency of a Flat-Plate Solar Collector," Sol. Energy, **86**(2), pp. 771–779.

[182] Otanicar, T., Dale, J., Orosz, M., Brekke, N., DeJarnette, D., Tunkara, E., Roberts, K., and Harikumar, P., 2018, "Experimental Evaluation of a Prototype Hybrid CPV/T System Utilizing a Nanoparticle Fluid Absorber at Elevated Temperatures," Appl. Energy, **228**(May), pp. 1531–1539.

[183] Celata, G. P., D'Annibale, F., Mariani, A., Sau, S., Serra, E., Bubbico, R., Menale, C., and Poth, H., 2014, "Experimental Results of Nanofluids Flow Effects on Metal Surfaces," Chem. Eng. Res. Des., **92**(9), pp. 1616–1628.

[184] Bubbico, R., Celata, G. P., D'Annibale, F., Mazzarotta, B., and Menale, C., 2015, "Experimental Analysis of Corrosion and Erosion Phenomena on Metal Surfaces by Nanofluids," Chem. Eng. Res. Des., **104**, pp. 605–614.

[185] Rashmi, W., Ismail, A. F., Khalid, M., Anuar, A., and Yusaf, T., 2014, "Investigating Corrosion Effects and Heat Transfer Enhancement in Smaller Size Radiators Using CNT-Nanofluids," J. Mater. Sci., **49**(13), pp. 4544–4551.

[186] Jiang, H., Wang, W., Chu, D., Lu, W., Cheng, D., Huang, Y., and Wu, Y., 2017, "Corrosion-Erosion Tests of Fusion Reactor Materials in Flowing Nanofluids," J. Nucl. Mater., **494**, pp. 361–367.

[187] Fotowat, S., Askar, S., Ismail, M., and Fartaj, A., 2017, "A Study on Corrosion Effects of a Water Based Nanofluid for Enhanced Thermal Energy Applications," Sustain. Energy Technol. Assessments, **24**, pp. 39–44.

[188] Fernández, A. G., Muñoz-Sánchez, B., Nieto-Maestre, J., and García-Romero, A., 2019, "High Temperature Corrosion Behavior on Molten Nitrate Salt-Based

Nanofluids for CSP Plants," Renew. Energy, **130**, pp. 902–909.

[189] Singh, N., and Khullar, V., 2019, "Efficient Volumetric Absorption Solar Thermal Platforms Employing Thermally Stable - Solar Selective Nanofluids Engineered from Used Engine Oil.," Sci. Rep., (November 2018), pp. 1–15.

[190] Singh, N., and Khullar, V., 2020, "On-Sun Testing of Volumetric Absorption Based Concentrating Solar Collector Employing Carbon Soot Nanoparticles Laden Fluid," Sustain. Energy Technol. Assessments, **42**(July), p. 100868.

[191] Fan, J. C. C., Bachner, F. J., Foley, G. H., and Zavracky, P. M., 1974, "Transparent Heat-Mirror Films of TiO2/Ag/TiO2 for Solar Energy Collection and Radiation Insulation," Appl. Phys. Lett., **25**(12), pp. 693–695.

[192] Fan, J. C. C., and Bachner, F. J., 1976, "Transparent Heat Mirrors for Solar-Energy Applications," Appl. Opt., **15**(4), p. 1012.

[193] Betts, K. H., Parsons, R. R., and Brett, M. J., 1985, "Heat Mirrors for Greenhouses," Appl. Opt., **24**(16), p. 2651.

[194] Khullar, V., Tyagi, H., Otanicar, T. P., Hewakuruppu, Y. L., and Taylor, R. A., 2018, "Solar Selective Volumetric Receivers for Harnessing Solar Thermal Energy," J. Heat Transfer, **140**(6), pp. 1–15.

[195] Khullar, V., Mahendra, P., and Mittal, M., 2018, "Applicability of Heat Mirrors in Reducing Thermal Losses in Concentrating Solar Collectors," J. Therm. Sci. Eng. Appl., **10**(6).

[196] Motamedi, M., Rafeie, M., Ebrahimnia Bajestan, E., and Taylor, R. A., 2021, "Mitigating the Losses in Nanofluid-Based Direct Solar Absorption Receivers," Renew. Energy, **178**, pp. 1174–1186.

[197] Duffie, J. A., and Beckman, W. A., 2013, *Solar Engineering of Thermal Processes: Fourth Edition*, Wiley, New York.

[198] Cengel, Yunus A., A. J. G., 2014, *Heat and Mass Transfer: Fundamentals and Applications.*, McGraw-Hill Professional.

[199] M.J.Brett;R.R.Parsons, 1985, "Properties of Transparent, Conducting ZnO Films Deposited by Reactive Bias Sputtering," Solid State Commun., **54**(7), pp. 603–606.

[200] Yoshida, S., 1980, "Efficiency of Drude Mirror Type Selective Transparent Filters for Solar Thermal Conversion.," Bull. Electrotech. Lab. Tokyo, **44**(1–2), pp. 80–87.

List of Publications

Published in peer reviewed (SCI) journals

1. **N.Singh,** V. Khullar "Efficient Volumetric Absorption Solar Thermal Platforms Employing Thermally Stable- Solar Selective Nanofluids Engineered from Used Engine Oil" *Scientific Reports*,9, 10541(2019) https://doi.org/10.1038/s41598-019-47126-3 I.F.- 4.996

2. **N.Singh,** V. Khullar "On-Sun testing of Volumetric Absorption Based Concentrating Solar Collector Employing Carbon Soot Nanoparticles Laden Fluid" *Sustainable Energy Technologies and Assessments, volume* 42, *December*2020,100868 https://doi.org/10.1016/j.seta.2020.100868 I.F.-7.632

Under review

3. **N.Singh,** V.Khullar "Experimental and Theoretical Investigation into Effectiveness of Transparent Heat Mirror Covers in Mitigating Thermal Losses in Volumetric Absorption Based Solar Thermal Systems"

NOVEL CONTRIBUTIONS MADE TO THE SCIENTIFIC RESEARCH

In the backdrop of the ever-increasing demand for intermediate temperature applications (viz. industrial and domestic heating/cooling); efforts to improve the existing solar thermal technologies have gained a lot of momentum. In recent times, particularly the "volumetrically absorbing solar thermal platforms" have seen renewed interests owing to their higher performance characteristics.

Stability of nanoparticle dispersions under practical operating conditions and optimizing receiver design to achieve higher thermal efficiencies are the two fundamental challenges faced in the development of volumetrically absorbing solar thermal platforms. In relation to stability of nanoparticle dispersions, the incumbent synthesis routes are not robust enough to be scaled up to cater real world solar thermal platforms (such as solar energy driven electricity generation systems).

In relation to optimum receiver design, high thermal losses (particularly radiative losses at high temperatures) are still a major road block in the development of efficient volumetric absorption based solar thermal platforms. To circumvent this issue, researchers have employed transparent heat mirrors as covers; however, the design aspects explored in the reported studies are still in nascent stage and more detailed understanding of the thermal loss mechanisms is warranted to come up with optimum receiver- cover configurations.

Present work is essentially a significant step in addressing the aforementioned challenges. 'used engine oil' has been employed to engineer nanofluids that retain their stability and functional characteristics even after being subjected to extreme conditions. Furthermore, the as-prepared nanofluid shows excellent stability i.e. it retains its optical characteristics and particle size distribution even after undergoing pumping and thermal cycles and moving in flow loops (circulation through pipes/valves) during on-sun testing. Moreover, the as-prepared nanofluid has negligible impact on the surface and optical properties of solar receiver constituent materials. Additionally, this has been done without the aid of sophisticated and energy intensive nanoparticle functionalization techniques.

Furthermore, we have designed and developed comprehensive experimental and theoretical modeling frameworks to understand and estimate the thermal losses for a host of receiver design configurations. For the first time the effect of heat mirror coating side (i.e. whether 'receiver facing' (RF) or 'sky facing' (SF) side has been coated) has been experimentally as well as theoretically investigated. In particular, the performance characteristics of ZnO based

transparent heat mirrors have been investigated. Further, we have been able to clearly delineate the fundamental performance limits of ideal heat mirrors both in RF and SF configurations.

Capitalizing on these, we have been able device an efficient volumetric absorption solar thermal platform that could attain higher efficiency compared to its surface absorption counterpart.